Risk Assessment of Anomalous Induced Seismicity

by

Jieyu Zhang

A thesis submitted in partial fulfillment of the requirements for the degree of

Master of Science

in

Geophysics

Department of Physics
University of Alberta

Abstract

Anomalous induced seismicity (AIS) is defined as the induced seismic events larger than moment magnitude (M_w) 0. Moderate-sized seismicity (that is, around M_w 4) has the potential to be felt by humans and damage infrastructure. Industrial operations such as hydraulic fracturing, have the potential of creating AIS. A risk assessment before such an operation is important. It helps us better understand, control and mitigate the risk of AIS. In this thesis, several practices applied to the risk assessment of AIS are examined. This thesis consists of three parts. First, refinements are made on the fault slip potential (FSP) analysis to utilize more information and provide a more comprehensive preliminary assessment of the risk. FSP analysis quantifies the likelihood of fault reactivation under the current knowledge. Second, guidance is given on choosing locations for additional samples because reducing the uncertainty in key parameters with more samples improves the accuracy of the risk assessment. Here the key parameter is the in situ stress. Simulations show that the optimal locations for adding samples are in the least-sampled areas. Third, practical tactics are applied to simplify the risk assessment process and make effective decisions to mitigate the risk. Because giving quantitative measurements of the risk of AIS is complex, the three-level risk evaluation system is implemented to assess the risk qualitatively. This approach is applied to an operation in Fox Creek, Alberta. The anticipated risk of AIS is transferred into an expected loss in the decision tree analysis. Using the decision tree, how the anticipated risk affects the decision-making process is demonstrated. The risk assessment of AIS becomes more complete by adopting these suggestions.

Preface

This dissertation is submitted for the degree of Master of Science in Geophysics at the University of Alberta. The research described herein is original, and neither this nor any substantially similar dissertation was or is being submitted for any other degree or other qualification at any other university.

Acknowledgements

I want to express my sincere appreciation to my supervisor, Dr. Mirko van der Baan for the guidance, patience and knowledge he gave me. He taught me how to think critically and made me realize my true passion for science.

I would like to extend my deepest gratitude to Dr. David Eaton from the University of Calgary for his generous support of my work. I would also like to thank my committee members, Dr. Mauricio Sacchi, Dr. Bruce Sutherland and Dr. Clayton Deutsch for their valuable advice and comments.

Special thanks are given to Benjamin Harding from the University of Alberta, Tim Tyrrell from XTO Energy, Sobhi Alhashwa from Ovintiv, Nadine Igonin, German Rodriguez, and Hongliang Zhang from the University of Calgary for sharing their work with me.

This thesis would not be possible without the financial support of the sponsors from the Microseismic Industry Consortium. I also gratefully acknowledge the assistance of my colleagues in the Microseismic Industry Consortium. Their assistance of this thesis is much appreciated.

Finally, I must express my very profound gratitude to my parents, Mingzhu Zhang and Quanhui Yi, and to my boyfriend, Keda Cao, for their unfailing and continuous encouragement throughout my years of study and through the process of researching and writing this thesis. I wouldn't have made it this far if it hadn't been for them.

Contents

List of Tables

List of Figures

List of Symbols

$A,\ B,\ C,\ D$	functions of μ and θ
$\mathbf{C}$	matrix of Cov
Cov	covariance
D_x	diffusivity
D_{z_0}	a set of values of z that satisfy $P(\mathbf{z} \leq z_0)$
E	Young's modulus
EV	expected value
EMV	expected monetary value
G	shear modulus
$\mathbf{G}$	vector containing covariates in the trend function of $Z_t(\mathbf{u})$
G_d	shear modulus of the dry frame
H	a function of P_d, ξ and T
$J,\ K$	functions of S_1, S_3, p_p, and θ
K_d, K_f, K_g	bulk moduli of the dry frame, fluid and the grain material
K_x	permeability
L	the set of samples with the distance of h_l
$\mathbf{M}$	matrix of all Cov between $\mathbf{u}_0$ and sampled locations
$M_{z_0},\ N_{z_0}$	sets of $\mathbf{m}$ and $\mathbf{n}$ that the union of them is D_{z_0}
N	total number of samples
$\mathbf{N}$	a matrix of coefficients, a function of $\mathbf{n}$
N_l	number of all combinations between elements in L
N_r	total number of risk factors that are evaluated
N_i^o	the optimal number of pairs in ith lag interval
N_i^s	the actual number of pairs in ith lag interval
$\mathbf{N}^o$	the vector of all N_i^o
$\mathbf{N}^s$	the vector of all N_i^s
P	possibility of AIS

P_d	a function of K_d and G_d
R	similarity coefficient of two probabilistic distributions
S_{Hm}	measured maximum horizontal stress
S_{hm}	measured minimum horizontal stress
SS	Sum of Squares
S_v	total vertical stress
S_0	cohesion
S_1	maximum principal stress
S_3	minimum principal stress
T	a function of ϕ, K_f, K_g, and ξ
U	number of total grids (locations)
$\mathbf{U}$	matrix of all $\mathbf{u}$
V_i	the value of ith outcome in a decision tree
V_p	primary wave velocity
V_s	shear wave velocity
$\mathbf{W}$	matrix of all Cov between samples
X	set of all values for $\mathbf{x}$
Y	set of all values for $\mathbf{y}$
$\mathbf{Y}$	vector of the differences between Z and m at all locations $\mathbf{U}$
Z	spatial variable that is a function of $\mathbf{u}$
Z_r	standardized residual of Z
Z_t	spatial variable with a trend
$\hat{Z}$	estimated value of Z
$a,\ b,\ c$	constants
$\mathbf{a}$	combinations of all possible choices of second-phase sampling locations
a_b	the best alternative in $\mathbf{a}$
d	safety distance
g	gravitational acceleration
h	lag

h_l	constant
k	number of samples after declustering
$\mathbf{m}, \mathbf{n}$	independent random variables
m	mean of Z
$m_{1i},\ m_{2i}$	parameters from the original Warrick-Myers sampling criterion
n	number of samples in one grid
$\mathbf{n}$	outward unit normal vector of a plane
n_a	number of available locations for measurements
n_c	number of locations that can be chosen for measurements
n_i	the component of $\mathbf{n}$ along the i-axis
o	number of possible outcomes in a decision tree
p	pore pressure change due to diffusion, a function of t and x
$\mathbf{p}$	traction on a plane
p_i	the probability of ith outcome in a decision tree
p_p	pore pressure
s_i	the score assigned to the ith risk factor
$s_1,\ s_2,\ s_3$	coefficients in the original Warrick-Myers sampling criterion
t	diffusion time
u	number of unsampled locations after declustering
$\mathbf{u}$	location
u_i	component of $\mathbf{u}$ along the i-axis
$u_x,\ u_y$	coordinates of $\mathbf{u}$
$\mathbf{u}_0$	random unsampled location
$\mathbf{v}$	slip vector
$v_x,\ v_y,\ v_z$	elements of $\mathbf{v}$ along the $x-,\ y-$ and $z-$axes
x	diffusion distance
$\mathbf{x}$	random variable
$\mathbf{y}$	random variable, a function of $\mathbf{x}$
$\mathbf{z}$	random variable, a function of $\mathbf{m}$ and $\mathbf{n}$

z_0	a constant
$\bar{z}$	averaged sample value in one grid
α	poroelastic modulus
$\boldsymbol{\alpha}$	vector with the mean and variance of $Z_t(\mathbf{u})$
$\boldsymbol{\beta}$	regression vector describing the trend of $Z_t(\mathbf{u})$
γ	variogram model, a function of h
$\hat{\gamma}$	experimental variogram
δ_m	misfit between the true and estimated values of Z
ε_H	strain along the maximum horizontal stress direction
ε_h	strain along the minimum horizontal stress direction
ζ	pore-fluid dynamic viscosity
η	range
θ	angle between $\mathbf{n}$ and the x-axis
$\boldsymbol{\theta}$	vector of $\sigma^2,\ \eta,\ \tau^2$
$\hat{\boldsymbol{\theta}}$	estimated $\boldsymbol{\theta}$
$\boldsymbol{\lambda}$	vector of all λ
λ_i	weight of the sample at $\mathbf{u}_i$
μ	coefficient of friction
ν	Poisson's ratio
ρ	density of the rock
$\boldsymbol{\Sigma}$	stress tensor
σ^2	sill; the variance of Z
$\sigma_{\bar{H}}$	horizontal uniaxial stress
σ_H	maximum effective horizontal stress
σ_h	minimum effective horizontal stress
σ_i	normal component of $\boldsymbol{\Sigma}$ along the i-axis
σ_n	value of the normal stress on a plane
σ_v	vertical stress in rocks
σ_E^2	error variance

σ^2_{E1}	error variance calculated using the first-phase samples
σ^2_{E2}	error variance calculated using the first- and second-phase samples
τ	value of the shear stress on a plane
τ_{ij}	shear component of $\mathbf{\Sigma}$ along the i-axis towards the j-axis
τ^2	nugget
ϕ	porosity
ξ	a function of K_d and K_g

List of Abbreviations

AIS	Anomalous Induced Seismicity
CFC	Coulomb Failure Criterion
cdf	cumulative distribution function
EV	Error Variance
EMV	Expected Monetary Value
FSP	Fault Slip Potential
pdf	probability density function
PSHA	Probability Seismic Hazard Analysis
TOC	Total Organic Carbon
WM	Warrick-Myers

Chapter 1

Introduction

1.1 Background

1.1.1 Anomalous induced seismicity

Anomalous induced sesimicity (AIS) is defined as induced seismic events that are above moment magnitude (M_w) 0 (Eaton, 2018). Injecting fluids into formations can cause AIS by reactivating adjacent faults (Atkinson et al., 2016; Bao and Eaton, 2016; Ellsworth, 2013). The mechanisms of induced seismicity from injection are summarized as the increase in the pore pressure and/or change in the stress field (Healy et al., 1968; Raleigh et al., 1976; Atkinson et al., 2016). Wastewater disposal, hydraulic fracturing and enhanced geothermal systems have led to AIS (e.g. Atkinson et al., 2016; Eaton et al., 2018; Ellsworth, 2013; Snee and Zoback, 2016; Van der Baan and Calixto, 2017). AIS has raised concerns and posed a risk of reducing the revenue, damaging the infrastructures and disturbing people's life. The series of earthquakes happened in Pohang, South Korea in November, 2017 is associated with an enhanced geothermal system close to the epicenter of the earthquakes (Ellsworth, 2013). These earthquakes caused human injuries and millions of infrastructure damages (Lee et al., 2019). The reactivation of the fault between the two injection wells is considered as the cause of this disastrous earthquake (Woo et al., 2019).

To mitigate the risk of AIS, different protocols, such as the traffic light

system, have been published (Kao, 2017; Shipman et al., 2018). While most regulations focus on the mitigation of AIS, understanding the risk is as important.

1.1.2 Risk assessment of anomalous induced seismicity

Risk assessment of AIS aims to understand the forthcoming risk associated with the operation and prepare for response in advance. Generally, risk is divided into possibility and impact (Aven, 2015). For AIS, the risk is controlled by both the possibility of initiating a slip on the fault and the impact of that slip.

The Coulomb failure criterion (CFC) is a common criterion used in assessing the failure of a fault (Bott, 1959; McKenzie, 1969; Jaeger et al., 2009; Raleigh et al., 1976; Sibson, 1985, 1990). It states that a failure happens on a fault when the normal and shear stresses on the fault exceed the frictional forces and cohesion (Mohr, 1914; Twiss and Moores, 1992; Zoback, 2010). Based on the CFC, Sibson (1985, 1990) grouped the faults into *favorably orientated, unfavorably orientated* and *misorientated* faults. Orientations of faults in different stress regimes are indicative of whether the faults are prone to be reactivated. Besides the fault orientation, the ratio between the normal and shear stress is another indicator of the tendency to slip of a fault (Worum et al., 2004).

On the other hand, there are notable and various sources of uncertainty lying within the CFC parameters. It is appropriate to include different sources of uncertainty in the analysis of fault failure. The uncertainty impedes having a determined answer about fault failure using CFC. The fault slip potential (FSP) analysis is proposed to calculate the likelihood of fault failure under the current knowledge of the CFC parameters with uncertainty (Walsh and Zoback, 2016). The FSP analysis predicts the probability of fault reactivation based on the CFC and the statistical relations amongst all parameters. The influence of the uncertainty on the probability of fault reactivation is quantified via Monte Carlo simulations. The advantage of this method is that it specifically addresses the parameter uncertainty. A better constraint of the parameter uncertainty improves the accuracy of the FSP analysis. The FSP analysis has been included

in the risk assessment of AIS (Hennings et al., 2019; Zhang and van der Baan, 2019a,b).

Injecting fluids into formations perturbs the probability of fault reactivation. One major source of perturbation is the pore pressure change from the injection point. The pore pressure diffusion theory quantifies this change (Papoulis and Pillai, 2002; Hsieh and Bredehoeft, 1981; Shapiro et al., 2002, 2003; Silin et al., 2003; Song et al., 2004; Shapiro and Dinske, 2009; Eaton, 2011; McGarr, 2014; Barthwal et al., 2017). The increase in the pore pressure makes the faults more prone to failure according to the CFC. Various seismicity catalogues show that both the intensity and magnitudes of the observed seismic events are related to the injection volume and rate during operations (e.g. Atkinson et al., 2016; Shapiro and Dinske, 2009; Shapiro et al., 2010; Langenbruch and Shapiro, 2010; Keranen et al., 2013; Weingarten et al., 2015). Based on the pore pressure diffusion theory, Shapiro (2018) proposes the Seismogenic index model to quantify the influence of injection volume to the seismic susceptibility of an area. One limitation of pore pressure diffusion theory is that the accuracy of the calculation depends on the hydrologic characterization of the porous medium. In other words, the analysis should be site-specific. Langenbruch et al. (2018) improve the Seismogenic index model by including regional hydrologic models. By combining the CFC and the pore pressure diffusion theory, the likelihood of the fault reactivation near injection sites is estimated.

After computing the probability, the next step is to understand the possible impact of the failure. There are two ways to quantify the potential impact, namely the magnitude of the earthquake and the ground motion caused by the earthquake.

The magnitude is correlated with the fault size and the stress drop (Stein and Wysession, 2009; Zoback and Gorelick, 2012; Walters et al., 2015). In general, the magnitude of an earthquake is loosely correlated with the size of the fault. However, the magnitude still varies because of the stress drop, which is difficult to quantify (Stein and Wysession, 2009). Therefore, the fault size can only qualitatively give insights on the possible magnitudes. Magnitudes of seismic events in one area are also constrained by the total amount of seismic events in that area during a certain amount of time, which is described as the

Gutenberg and Richter law (Gutenberg and Richter, 1956). This law gives the maximum magnitude that can occur in the area. The possible maximum magnitude acts as an upper bound in the risk assessment as it is the worst case (Baker, 2013).

The magnitude and ground motion are loosely related as well. The impact is directly related to the ground motion. Infrastructures are built to withstand ground motions below a certain threshold. If the ground motion exceeds the threshold, infrastructure damage could occur. Ground motion is predicted using equations with the magnitude and the distance from the epicenter as variables. Again, the prediction equations are not precise in calculating the ground motion due to various sources of uncertainty (Van Eck et al., 2006). Therefore, probabilistic seismic hazard analysis (PSHA) is proposed. By adopting the total probability theorem, PSHA gives the probability of the ground motion exceeding the threshold at a specific location (Baker, 2013). Other methods to assess the risk of AIS have been proposed. Bommer et al. (2006) propose an improved real-time risk management of AIS by using a traffic light system based on ground motion. Hybrid methods that combine the statistical prediction approaches based on PSHA and the physics-based prediction approaches based on rock models have also been applied to the risk assessment of AIS (Gischig and Wiemer, 2013; Gaucher et al., 2015).

1.1.3 Understanding the in situ stress

Understanding the in situ stress state correctly plays an important part in the risk assessment. The in situ stress state includes both the stress magnitude and orientation of the three principal stresses. The in situ stress state is influenced by multiple factors, such as the topography, tectonic stresses, rock properties, natural fracture networks, local geological and operational histories (Jaeger et al., 2009; Zoback, 1992; Hillis and Reynolds, 2000; Cui et al., 2013; Soltanzadeh et al., 2015). By knowing the in situ stress state, whether a fault is at a critical stress state is analyzed using the CFC. Operators can avoid areas with critically stressed faults when planning operations. In general, different measurements of the stress take different amounts of time and effort, and also

present different qualities of the data (Zoback, 1992). There are two major sources of uncertainty in the stress measurements: first, the uncertainty comes from the sparseness of the measurements. As the accuracy of the measurements increases, the cost of the measurements increases as well. Hence the accurate measurements are sparse. Second, all the measurements are limited by the geographical locations of the wells, which vary spatially.

Interpolating the stress measurements shows how the in situ stress changes within the area of interest (e.g. Soltanzadeh et al., 2015; Shen et al., 2018). In this thesis, interpolation means both interpolation and extrapolation. Generally, the robustness of interpolation increases with the number of stress measurements. Ideally, every location should be measured. But this is not achievable. First, there are measurement errors (Sullivan, 2015). The stress measurements might not represent the true values due to the limitation of the available measurement approaches (Bell and Grasby, 2012; Shen et al., 2018). Second, wells at the target depth are required for the measurements. This could be time-consuming and expensive if the wells are deep.

There are multiple approaches to interpolate geological samples like the stress measurements, such as trend surface, nearest-neighbor, splines, inverse weighted distance and kriging (Ripley, 1981). Kriging has been used to interpolate the in situ stress (Shen et al., 2018). Kriging considers the spatial correlation and the variability of the samples.

Besides choosing an effective interpolation method, optimizing the sampling design can improve the interpolation results as well. There are four common spatial sampling schemes, *random, stratified random, systematic* and *systematic random* (Ripley, 1981; Delmelle, 2012; Wang et al., 2012). Since the stress measurements are limited by the well locations, the four common sampling designs are not applicable in this case. Here, the second-phase sampling design is considered. The second-phase samples are additional stress measurements. There are different types of uncertainty in the interpolation process (Kennedy and O'Hagan, 2001). Sampling criteria are designed to either reduce the interpolation error variances or improve the spatial coverage of the samples (Armstrong, 1984; Wang et al., 2012). Wang et al. (2012) and Delmelle (2012) both give detailed reviews on various sampling designs.

If the stress measurements used in the risk assessment contain too much uncertainty, the effectiveness of the assessment is questionable. Additional stress measurements reduce the uncertainty and hence improve the risk assessment. However, as mentioned above, the locations of the stress measurements are limited by the well locations, and the accuracy of the measurements is positively related to the cost. In addition, the available wells might not necessarily be at the optimal locations for additional sampling. Under these limitations, the optimal locations for additional stress measurements might be difficult to choose. To recreate the real situation when choosing which wells for additional stress measurements, a premise is set. The premise here is that the available wells are pre-determined and only part of these wells can actually be measured. This premise is crucial in the guidance of determining the optimal locations for additional stress measurement. By choosing the optimal locations for stress measurements, the understanding of the in situ stress is improved.

1.1.4 Decision analysis and risk assessment

The impact of AIS is another part to consider when assessing the risk. The risk assessment of AIS proposed in recently years has started to assess the risk qualitatively rather than quantitatively as the impact can be difficult to characterize precisely with numbers. Walters et al. (2015) propose a project-based risk tolerance matrix to analyze factors affecting the risk based on a traffic light system. This workflow uses the traffic light system to mark the level of the risk. It requires the analysts to have a comprehensive understanding of the variables related to the exposure of the operation. Canadian Association of Petroleum Producers (CAPP) (2019) publish an industry shared practice about the risk assessment and management of AIS. Five factors, including historical seismicity, in situ stress, geological fault mapping, operational risk factors and consequences, should all be analyzed during the risk assessment of AIS.

Since the risk assessment is also a part of the decision making process of the operation, techniques used in the decision analysis are adopted to improve the risk assessment of AIS. Decision analysis has been implemented in the planning process of petroleum exploration and production (Bratvold and Begg, 2010;

Newendorp and Schuyler, 2000). It is a series of methodologies adopted from decision theory to guide the practical decision-making processes (Newendorp and Schuyler, 2000; Eidsvik et al., 2015; Bratvold et al., 2007).

1.2 Motivation and contribution

The motivation of this thesis is to provide practical solutions that optimize the risk assessment of AIS.

In this thesis, the FSP analysis is expanded by including the variations in principal stress and pore pressure gradients with depth. The modified FSP analysis will show at which depth the fault is more prone to slip.

As mentioned above, interpolating the in situ stress correctly improves the risk assessment. To achieve this goal, two sampling criteria for determining the additional locations of stress measurements are proposed and compared. By comparing the misfit reductions between the interpolated results and the true data set, the better criterion to determine the additional locations for stress measurements is known.

Implementing decision analysis to the risk assessment of AIS optimizes the assessment and the decision-making process of the whole operation. Two common techniques from the decision analysis are used, the three-level risk evaluation and the decision tree analysis.

Risk assessment cannot be accomplished perfectly since the future is unpredictable. Therefore, this thesis proposes multiple solutions to improve the risk assessment of AIS. Most of the methodologies in this thesis have been developed but not yet been well applied to the risk assessment of AIS specifically.

The contribution of this thesis unfolds into three parts:

1. Modifying the FSP analysis to improve the calculation of the fault reactivation likelihood;

2. Suggesting locations for additional stress measurements to reduce the uncertainty in stress interpolation; and

3. Adopting techniques in decision analysis to the risk assessment process to provide a simple and clear risk assessment workflow.

1.3 Thesis structure

This thesis begins with an overview of the Coulomb failure criterion and the Monte Carlo simulation in **Chapter 2**, which are the basic theories applied in the FSP analysis.

Chapter 3 shows a comprehensive FSP analysis of a series of strike-slip faults in Fox Creek, Alberta. principal stresses in the studied area are derived from well logs. The vertical variations of the principal stresses and the pore pressure are considered to conduct a 3D FSP analysis. The observed seismic events during the operation are also analyzed and the 3D FSP analysis is updated accordingly.

Chapter 4 explains the methodology of kriging in detail as it is the main interpolation method used to estimate the in situ stress. Considering the different sources of uncertainty in the kriging process, two sampling criteria targeting two different sources are introduced. They are the Warrick-Myers sampling criterion and the error-variance based criterion. Because the objective is to find the optimal locations for additional measurements, the Warrick-Myers sampling criterion is modified.

Chapter 5 compares the effectiveness of the two criteria in determining the optimal locations for additional sampling with simulations. The robustness of the two criteria are also tested through sensitivity tests.

Chapter 6 demonstrates the application of decision analysis to the risk assessment of AIS. The same operation studied in **Chapter 3** is analyzed using the three-level risk evaluation system and the decision tree analysis.

Chapter 7 presents the conclusion and possible future work.

Chapter 2

Fault slip potential analysis - theory

Summary

In this chapter, the calculation of stresses on a fault plane is shown, the mechanism of fault reactivation is explained, and the capability of using Monte Carlo simulations to replace analytical calculation is proved. The fault slip potential (FSP) analysis considers the uncertainty in related parameters as it plays an important role in understanding the probability of fault reactivation. The idea and workflow of FSP analysis are explained. Based on the CFC, FSP applies Monte Carlo simulations to capture the influence of the uncertainties of the parameters in the prediction of fault reactivation.

2.1 Introduction

The objective of this chapter is to explain the basic theories applied in the FSP analysis, which calculates the likelihood of fault reactivation under the current knowledge.

AIS, similar to natural earthquakes, is caused by the reactivation of existing faults. Fault reactivation is the slip movement along the fault plane resulting from the stresses applied to the fault (Twiss and Moores, 1992; Jaeger et al.,

2009). Fault reactivation is also referred as fault failure in this thesis. The chance is higher for a fault to fail again comparing to creating a new fault (Bott, 1959; Alaniz-Álvarez et al., 2000). When perturbing the stress state of a fault by injecting fluids, the change in the stress state on the fault plane could lead to the fault failure (Ellsworth, 2013; Zoback, 2010).

By understanding the mechanism of fault reactivation, one can predict whether a fault will slip again. To reactivate a fault, the critical shear stress must equal or exceed the frictional resistance on the fault (Jaeger et al., 1969). The most common and accepted criterion of fault reactivation is the Coulomb failure criterion (CFC) (Yin and Ranalli, 1992; Lisle and Srivastava, 2004). Using CFC, various analyses related to the fault reactivation are established (e.g. Sibson, 1974, 1990; Morris et al., 1996; Worum et al., 2004; Walsh and Zoback, 2016).

Multiple parameters are involved in the determination of fault reactivation, including the fault geometry, the stress state on the fault plane, and the frictional resistance of the fault. These parameters are either directly measured or estimated. These measurement errors and estimations bring uncertainty to the prediction of fault failure. The uncertainty in the prediction is a function of all kinds of errors and can be calculated analytically once the errors are known. But the complexity of a solution increases with the number of parameters. An alternative is to use the Monte Carlo simulations, which are based on random sampling. It provides numerical solutions for statistical problems, especially when the analytical solutions are too complex to calculate (Eidsvik et al., 2015). Based on the Law of Large Numbers, the similarity between the numerical results and the analytical results is proportional to sampling size.

Walsh and Zoback (2016) apply Monte Carlo simulations to predict the likelihood of fault reactivation considering the errors in all the CFC parameters. The percentage of fault failures given all realizations is called the FSP. FSP indicates the likelihood of fault reactivation given the current understanding of the parameters. Since fault reactivation is a key point in seismic assessment (Neves et al., 2009), FSP analysis helps the risk analysts anticipate the possibility of the AIS. If the fault has a high possibility of reactivation without any perturbation from the injection, the risk of AIS could be high.

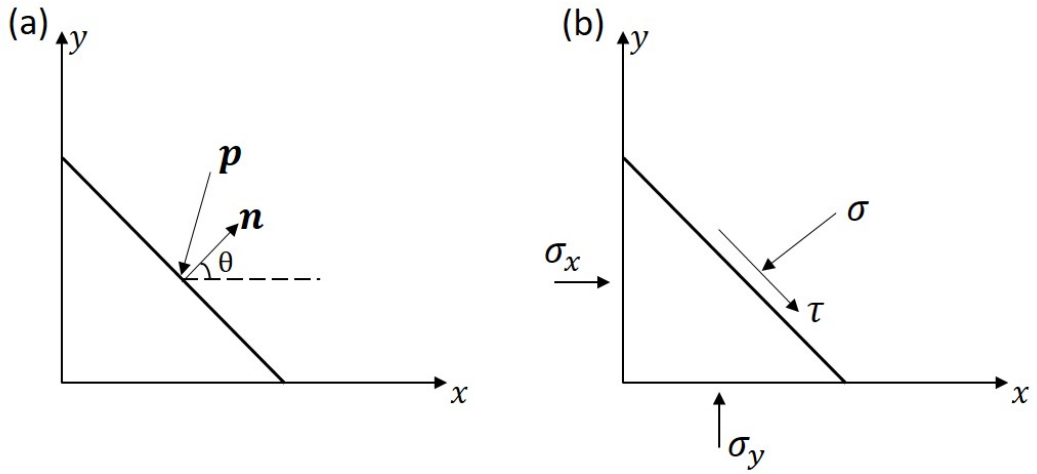

Figure 2.1: A plane in two dimensions. (a). Traction **p** and unit normal **n** of a plane. (b). Normal and shear stresses, σ and τ, on the same plane in (a). σ_x and σ_y are the principle stresses. They are in the same directions of the axes. The other principle stress is parallel to the plane.

In this chapter, the mechanism of fault slip, the method of Monte Carlo simulations, and the FSP analysis are explained in detail. The analytical results of fault reactivation with uncertainties of the parameters are compared with the results from Monte Carlo simulations.

2.2 Mechanism of fault reactivation

2.2.1 Traction and stress on a plane

In this section, the calculation of the normal and shear stresses on a plane is explained. The problem is first set in two dimensions and then expanded into three dimensions. The following explanation is adopted from Jaeger et al. (2009).

The traction **p** on a plane is defined as the force applying on the plane divided by its total area. A unit normal of a plane, **n**, points outward from the plane. Both **p** and **n** are illustrated in Figure 2.1(a). If the plane is a fault, **n** is the unit normal of the foot wall pointing outwards. Using the Pythagorean theory, $\mathbf{n} = (n_x, n_y)$, where $n_x^2 + n_y^2 = 1$. The angle between **n** and the x-axis is θ, as shown in Figure 2.1(a). Then $n_x = cos\theta$ and $n_y = sin\theta$. The traction

$\mathbf{p}$ is calculated using the stress tensor $\mathbf{\Sigma}$ and the unit normal $\mathbf{n}$ as

$$\mathbf{p} = \mathbf{\Sigma}\mathbf{n} = \begin{bmatrix} \sigma_x & \tau_{xy} \\ \tau_{yx} & \sigma_y \end{bmatrix} \begin{bmatrix} n_x \\ n_y \end{bmatrix}. \tag{2.1}$$

If the principle stresses are in the same directions of $x-$ and $y-$axis, then $\tau_{xy} = \tau_{yx} = 0$. And $\mathbf{\Sigma}$ contains only the principal stresses, as shown in Figure 2.1(b). $\mathbf{\Sigma}$ becomes

$$\mathbf{\Sigma} = \begin{bmatrix} \sigma_x & 0 \\ 0 & \sigma_y \end{bmatrix}. \tag{2.2}$$

The normal and shear stresses on the plane, σ_n and τ, then equal

$$\begin{aligned} \sigma_n = \mathbf{p}^T\mathbf{n} = \begin{bmatrix} \sigma_x n_x \\ \sigma_y n_y \end{bmatrix}^T \begin{bmatrix} n_x \\ n_y \end{bmatrix} = \sigma_x n_x^2 + \sigma_y n_y^2, \\ \tau = \sqrt{|\mathbf{p}|^2 - \sigma_n^2} = (\sigma_x - \sigma_y) n_x n_y. \end{aligned} \tag{2.3}$$

Equation 2.3 can be rewritten as

$$\begin{aligned} \sigma_n &= \frac{\sigma_x + \sigma_y}{2} + \frac{\sigma_x - \sigma_y}{2}\cos 2\theta, \\ \tau &= \frac{\sigma_x - \sigma_y}{2}\sin 2\theta. \end{aligned} \tag{2.4}$$

Based on Equation 2.4, we have

$$[\sigma_n - (\frac{\sigma_x + \sigma_y}{2})]^2 + \tau^2 = (\frac{\sigma_x - \sigma_y}{2})^2. \tag{2.5}$$

Equation 2.5 is a formula of a circle with the center at $(\frac{\sigma_x+\sigma_y}{2}, 0)$ and the radius of $\frac{\sigma_x-\sigma_y}{2}$. Therefore, the relation of σ_n and τ on the same plane is a circle. We can plot the circle with a Cartesian coordinate system where the x-axis is σ_n and the y-axis is τ. The circle is the Mohr diagram. In a compressive stress field, both normal and shear stresses are positive.

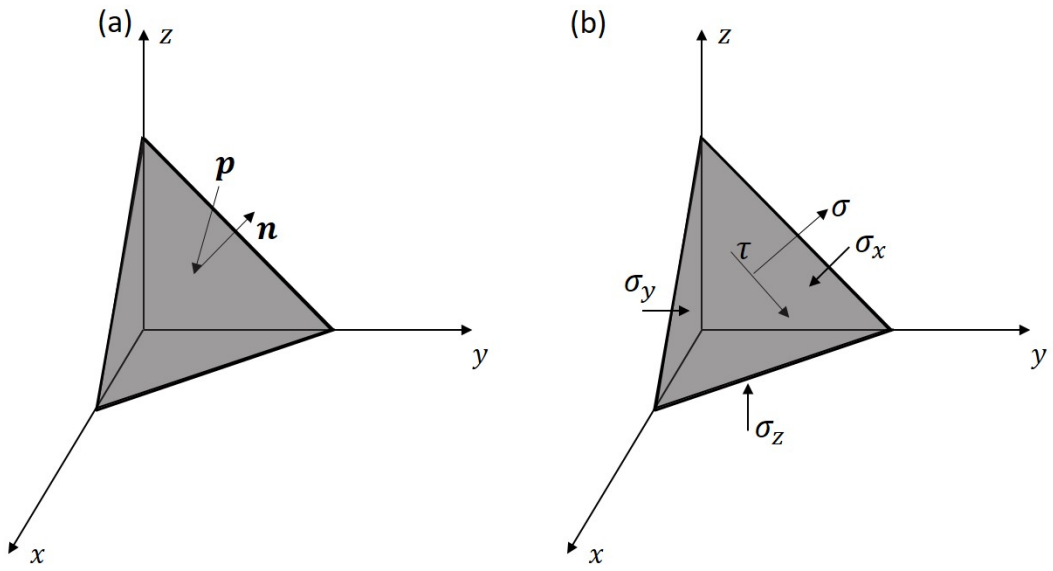

Figure 2.2: Traction and stress on a plane in three dimensions. (a). Traction $\mathbf{p}$ and unit normal $\mathbf{n}$ of a plane. (b). Normal and shear stresses, σ and τ, on the same plane in (a). σ_x, σ_y and σ_z are the principle stresses, which are in the same directions of the axes.

In three dimensions, $\mathbf{\Sigma}$ is

$$\mathbf{\Sigma} = \begin{bmatrix} \sigma_x & \tau_{xy} & \tau_{xz} \\ \tau_{yx} & \sigma_y & \tau_{yz} \\ \tau_{zx} & \tau_{zy} & \sigma_z \end{bmatrix}. \tag{2.6}$$

Again, in Figure 2.2(b), the principle stresses are in the same directions of the $x-$, $y-$ and $z-$axis, so the non-diagonal elements in $\mathbf{\Sigma}$ become zero. Hence $\mathbf{p}$ shown in Figure 2.2(a) equals

$$\mathbf{p} = \mathbf{\Sigma n} = \begin{bmatrix} \sigma_x & 0 & 0 \\ 0 & \sigma_y & 0 \\ 0 & 0 & \sigma_z \end{bmatrix} \begin{bmatrix} n_x \\ n_y \\ n_z \end{bmatrix}. \tag{2.7}$$

Similar to Equation 2.3, in Figure 2.2(b), σ_n is

$$\sigma_n = \mathbf{p}^T\mathbf{n} = \begin{bmatrix} \sigma_x n_x \\ \sigma_y n_y \\ \sigma_z n_z \end{bmatrix}^T \begin{bmatrix} n_x \\ n_y \\ n_z \end{bmatrix} = \sigma_x n_x^2 + \sigma_y n_y^2 + \sigma_z n_z^2, \tag{2.8}$$

and the shear stress τ

$$\tau = \sqrt{|\mathbf{p}|^2 - \sigma_n^2} = \sqrt{(\sigma_x - \sigma_y)^2 n_x^2 n_y^2 + (\sigma_x - \sigma_z)^2 n_x^2 n_z^2 + (\sigma_y - \sigma_z)^2 n_y^2 n_z^2}. \tag{2.9}$$

The two dimensional scenario is applicable to cases when one of the principal stresses is parallel to the fault plane. And the three dimensional scenario deals with cases when none of the principal stresses in parallel to the fault plane.

2.2.2 Coulomb failure criterion

With a low compressive normal stress, to create a shear fracture on the plane, σ_n and τ on a fault plane satisfy (Twiss and Moores, 1992)

$$\tau \geqslant \mu\sigma_n + S_0, \tag{2.10}$$

where μ is the frictional coefficient, and S_0 is the cohesion of the rock. The shear stress that equals $\mu\sigma_n + S_0$ is called the critical shear stress.

2.2.3 Description of fault reactivation

The Coulomb failure criterion (CFC) is widely used to determine whether the stress state is sufficient to cause a fault to slip as well (Twiss and Moores, 1992; Worum et al., 2004; Walsh and Zoback, 2016). If the normal and shear stresses on a fault plane satisfy the relation in Equation 2.10, the fault is considered to be reactivated. Graphically, the line representing the Coulomb failure criterion intersects with the Mohr diagram. As shown in Figure 2.3, failure is not limited to the stress state σ_n and τ_n, but all planes within the shaded area will fail.

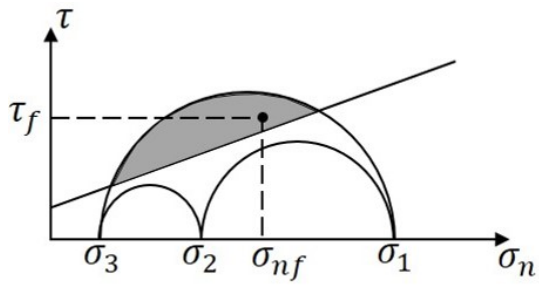

Figure 2.3: Mohr diagrams intersect with the CFC. The Mohr diagrams are the circles and the CFC is the straight line intersecting the outer circle. Faults in the shaded area are expected to fail. σ_{nf} and τ_f represent one possible combination of normal and shear stresses on a fault plane that is capable of initiating a fault failure.

2.2.4 Slip direction

Bott (1959) establishes a theory about oblique slip faulting. The theory demonstrates that the direction of the sliding plane does not need to be parallel to any principal stresses. To calculate the slip vector, which are indicative of the slip direction, the Wallace-Bott assumption is applied. The assumption states that the slip vector $\mathbf{v}$ is in the direction of the shear stress on the fault plane (Bott, 1959; Pollard et al., 1993; Michael, 1984). The slip vector $\mathbf{v}$ is calculated by (Vavryčuk, 2014; Jia et al., 2018; Zhang et al., 2019)

$$\mathbf{v} = \begin{bmatrix} v_x \\ v_y \\ v_z \end{bmatrix} = \mathbf{N} \begin{bmatrix} \sigma_x & \sigma_y & \sigma_z & \tau_{yz} & \tau_{xz} & \tau_{xy} \end{bmatrix}^T, \tag{2.11}$$

where

$$\mathbf{N} = \begin{bmatrix} n_x(1-n_x^2) & -n_y n_x^2 & -n_z n_x^2 \\ -n_x n_y^2 & n_y(1-n_y^2) & -n_z n_y^2 \\ -n_x n_z^2 & -n_y n_z^2 & n_z(1-n_z^2) \\ -2n_x n_y n_z & n_z(1-2n_y^2) & n_y(1-2n_z^2) \\ n_z(1-2n_x^2) & -2n_x n_y n_z & n_x(1-2n_z^2) \\ n_y(1-2n_x^2) & n_x(1-2n_y^2) & -2n_x n_y n_z \end{bmatrix}^T,$$

σ_i and τ_{ij} are the elements of $\mathbf{\Sigma}$ where the principle stresses are not in the same directions of the $x-$, $y-$, or the $z-$axis. n_i are the elements of the unit normal $\mathbf{n}$.

2.2.5 Safety distance

The safety distance d is defined as the distance between the stress state of the fault in the Mohr circle and the CFC line. The safety distance is illustrated as the dashed line in Figure 2.4. d is calculated by

$$d = \frac{|\mu\sigma_n - \tau + S_0|}{\sqrt{1+\mu^2}}, \tag{2.12}$$

The calculation of the distance between a point and a line is adopted from Ballantine and Jerbert (1952). If d is positive, the fault is stable. Otherwise,

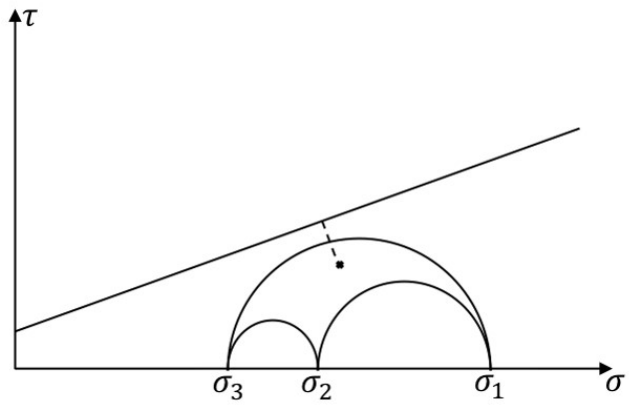

Figure 2.4: Illustration of the safety distance d (the dashed line). The cross in the Mohr Circles indicates the values of the normal and shear stresses on the fault plane. The three half-circles are 3D Mohr circles and the straight line is the CFC.

the fault slips. The FSP equals the percentage of cases where d is negative or zero in the Monte Carlo simulations.

Equation 2.12 shows that d is a function of all the CFC parameters, as

$$d = f(\sigma_n, \tau, \mu, S_0). \tag{2.13}$$

For each Monte Carlo simulation, the input values are generated based on the distributions of the parameters. Whether the fault fails in this simulation is determined based on Equation 2.10. The distribution of d is constrained by the distributions of the parameters through Equation 2.13 (Papoulis and Pillai, 2002). The analytic expressions of the distribution of d, based on variations in solely one or two parameters are explained in the following. By characterizing the probability density function (pdf) of d derived from FSP analysis, how the variances of all the parameters affect the FSP is represented.

2.3 Analytical and simulated solutions

2.3.1 Monte Carlo simulation

Monte Carlo simulation is an algorithm for calculating numerical results based on random sampling. According to the Law of Large Numbers, the simulated results from performing the same experiment a large number of times become comparable to the analytical results.

2.3.2 Analytical solutions

The following analysis is based on Papoulis and Pillai (2002).

Assume two random variables $\mathbf{x}$ and $\mathbf{y}$, and their relation is

$$\mathbf{y} = g_1(\mathbf{x}). \tag{2.14}$$

If the set of all values for $\mathbf{x}$ is X, the set of all values for $\mathbf{y}$ is calculated using the relation between $\mathbf{x}$ and $\mathbf{y}$ and denoted as a set of Y. For a specific value y, we have n real roots of Equation 2.14 as

$$y = g_1(x_1) = g_1(x_2) = ... = g_1(x_n). \tag{2.15}$$

If the pdf of $\mathbf{x}$ is $f_x(x)$, the pdf of the output variable $\mathbf{y}$, $f_y(y)$, can be calculated

from Equation 2.15 as

$$f_y(y) = \frac{f_x(x_1)}{\mid g_1'(x_1) \mid} + \frac{f_x(x_2)}{\mid g_1'(x_2) \mid} + ... + \frac{f_x(x_n)}{\mid g_1'(x_n) \mid}. \tag{2.16}$$

The detailed proof can be found in Papoulis and Pillai (2002).

If there are two random variables $\mathbf{m}$ and $\mathbf{n}$, and another variable $\mathbf{z}$ is described as

$$\mathbf{z} = g_2(\mathbf{m}, \mathbf{n}). \tag{2.17}$$

To calculate the pdf of $\mathbf{z}$ for known pdf's of $\mathbf{m}$ and $\mathbf{n}$, the cumulative distribution function ($F_z(z_0)$) (cdf) of $\mathbf{z}$ is computed first. $F_z(z_0)$ means the probability of variable $\mathbf{z}$ being equal or smaller than a constant z_0, $F_z(z_0) = P(\mathbf{z} \leqslant z_0)$. Since $\mathbf{z}$, $\mathbf{m}$, and $\mathbf{n}$ satisfy the relation in Equation 2.17, $F_z(z_0)$ implies that $\mathbf{m}$ and $\mathbf{n}$ that are in the region D_{z_0} satisfy the inequality $g_2(m, n) \leqslant z_0$. Thus $F_z(z_0)$ can be calculated as

$$\begin{aligned} F_z(z_0) =& P(\mathbf{z} \leqslant z_0) = P(g_2(\mathbf{m}, \mathbf{n}) \leqslant z_0) \\ =& P((\mathbf{m}, \mathbf{n}) \in D_{z_0}) \\ =& \iint_{m,n \in D_{z_0}} f_{mn}(m, n) dm dn, \end{aligned} \tag{2.18}$$

where $f_{mn}(m, n)$ is the joint pdf of $\mathbf{m}$ and $\mathbf{n}$ in D_{z_0}. Assume $\mathbf{m}$ and $\mathbf{n}$ are independent, and $g_2(\mathbf{m}, \mathbf{n})$ is

$$\mathbf{z} = \mathbf{m} + \mathbf{n}, \tag{2.19}$$

then the pdf of $\mathbf{z}$ is the convolution of $f_m(m)$ and $f_n(n)$. Denote set M_{z_0} and set N_{z_0} are the sets of $\mathbf{m}$ and $\mathbf{n}$ that the union of M_{z_0} and N_{z_0} is D_{z_0}, we have

$$\begin{aligned} f_z(z_0) &= \int_{N_{z_0}} \int_{X_{z_0}} f_m(z_0 - n) f_n(n) dm dn \\ &= f_m(m) * f_n(n). \end{aligned} \tag{2.20}$$

where the symbol $*$ denotes convolution.

2.3.3 Comparison between simulated and analytical results

In this section, the analytical and simulated pdf's of d are compared. The analytic results can be used to test if the Monte Carlo simulations are correct, or the other way around. A 2D Mohr diagram is used here for simplicity. In a 2D Mohr diagram, the stress on a fault plane can be calculated graphically using Equation 2.4. d in Figure 2.4 is the distance between the stress point calculated using Equation 2.4 and the CFC. The effect of pore pressure is also included in the calculation. The three principal stresses are denoted as S_1, S_2 and S_3 where S_1 is the maximum stress and S_3 is the minimum. S_2 is parallel to the fault plane so it is not included in the calculation. Therefore, the effective principal stresses σ_x and σ_y in Equation 2.4 are

$$\sigma_x = S_1 - p_p, \sigma_y = S_3 - p_p, \tag{2.21}$$

where p_p is the pore pressure. Combining Equation 2.4 to Equation 2.21, d is

$$\begin{aligned} d = & \frac{\mu(S_1 + S_3 - 2p_p + (S_1 - S_3)\cos 2\theta)}{2\sqrt{1+\mu^2}} \\ & - \frac{(S_1 - S_3)\sin 2\theta + 2S_0}{2\sqrt{1+\mu^2}}. \end{aligned} \tag{2.22}$$

To further illustrate how the analytical results are derived, assume the variables are uniformly distributed and independent.

One variable

If there is only one variable in Equation 2.22, and this variable is uniformly distributed in $[a, b]$, Equation 2.16 can be derived as

$$f_y(y) = \frac{1}{\mid g'(x) \mid} \frac{1}{b-a}. \tag{2.23}$$

Furthermore, if $\mathbf{x}$ is linearly related to $\mathbf{y}$, $g'(x)$ is a constant value. Therefore $f_y(y)$ is also uniformly distributed. On the other hand, if $\mathbf{x}$ is not linear related

to $\mathbf{y}$, $f_y(y)$ is determined by the derivative of $g_1(x)$. To calculate the derivatives with different variables, first we can rewrite Equation 2.22 as

$$d = AS_1 + BS_3 + Cp_p + DS_0, \tag{2.24}$$

where

$$A = \frac{\mu + \mu\cos 2\theta - \sin 2\theta}{2\sqrt{1+\mu^2}}, B = \frac{\mu - \mu\cos 2\theta + \sin 2\theta}{2\sqrt{1+\mu^2}},$$
$$C = -\frac{\mu}{\sqrt{1+\mu^2}}, D = \frac{1}{\sqrt{1+\mu^2}}.$$

Equation 2.22 can also be rewritten as

$$d = \frac{1}{\sqrt{1+\mu^2}}[\mu(\frac{S_1 + S_3 - 2p_p}{2} + \frac{(S_1 - S_3)\cos 2\theta}{2}) + (S_0 - \frac{(S_1 - S_3)\sin 2\theta}{2})], \tag{2.25}$$

or

$$d = \frac{\mu(S_1 - S_3)}{2\sqrt{1+\mu^2}}\cos 2\theta - \frac{S_1 - S_3}{2\sqrt{1+\mu^2}}\sin 2\theta + \frac{\mu(S_1 + S_3 - 2p_p) + 2S_0}{2\sqrt{1+\mu^2}}. \tag{2.26}$$

Equation 2.24 shows that S_1, S_3, p_p and S_0 all have linear relations with d in a form as $y = ax + b$. Equation 2.25 and Equation 2.26 show that non-linear relations exist between μ, θ and d.

Therefore, the pdf of d under the circumstance where one of the linearly related parameters is the variable, is also uniformly distributed. In contrast, the pdf of d when μ or θ is the variable is not uniformly distributed. $g'(x)$ equals A, B, C or D in Equation 2.23 when the variable is S_1, S_3, p_p or S_0 respectively. When the variable is μ, $g'(\mu)$ is

$$g'(\mu) = \frac{J}{\sqrt{1+\mu^2}} - \frac{J\mu^2 + K\mu}{(1+\mu^2)^2}, \tag{2.27}$$

where

$$J = \frac{S_1 + S_3 - 2p_p}{2} + \frac{(S_1 - S_3)\cos 2\theta}{2}, K = S_0 - \frac{(S_1 - S_3)\sin 2\theta}{2}.$$

Similarly, $g'(\theta)$ is

$$g'(\theta) = -2\frac{\mu(S_1 - S_3)}{2\sqrt{1+\mu^2}}\sin 2\theta - 2\frac{S_1 - S_3}{2\sqrt{1+\mu^2}}\cos 2\theta. \tag{2.28}$$

To include the uncertainty in the parameters, each parameter in Equation 2.22 is assigned with the mean and the range listed in Table 2.1. The range is generated based on a uniform distribution with a standard deviation of 0.15. The pdf's of d are computed using Equation 2.22 and Equation 2.23, with results shown as the red lines in Figure 2.5. Here each parameter in Equation 2.22 is uniformly distributed if considered as a variable, otherwise the mean is used as the value. For Monte Carlo simulations, the results are shown in the blue bars in Figure 2.5. The results are calculated using MATLAB® scripts. The steps are:

1. Determine which parameter is the variable.
2. Create a *for* loop that repeats 5000 times. In each loop, the value of the variable is randomly generated from a uniform distribution with the the mean and the variance of the variable. The mean of each parameter when it is treated as the variable is shown in Table 2.1. The variance is 0.15^2.
3. In each for loop, calculate the safety distance d using Equation 2.24.
4. Store the value of d in another array.
5. After the 5000 rounds, calculate and store the pdf of d.
6. Repeat step 2-5 for another 9 times. The final pdf of d is the average of the 10 pdf's.

The pdf's of d using the Monte Carlo simulations are also shown in Figure 2.5. Great similarities lie between the analytical results and the simulated results.

Two variables

There are four independent parameters in Equation 2.24 that are linearly related to d. If two of them are selected as uniformly distributed variables, d and

Table 2.1: Means and ranges of all parameters in Equation 2.22. *: generated based on a uniform distribution with a standard deviation of 0.15.

Variable	Mean	Range*
S_1	$60MPa$	51-69MPa
S_3	$20MPa$	17-23MPa
p_p	$10MPa$	8.5-11.5MPa
θ	60°	42.5°-57.5°
μ	0.6	0.51-0.69
S_0	$5MPa$	4.25-5.75MPa

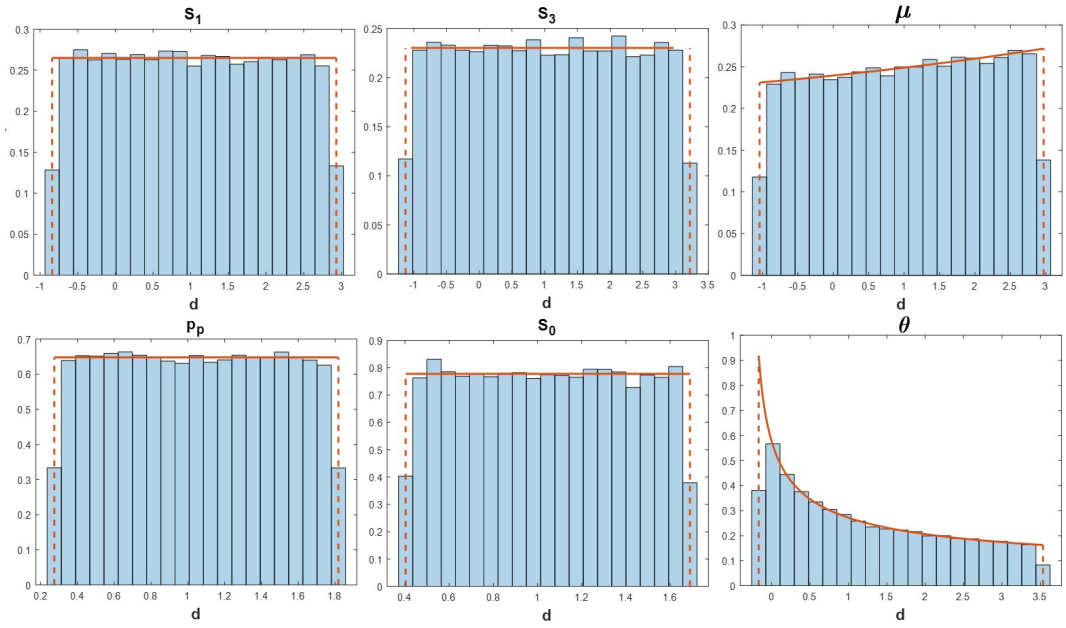

Figure 2.5: Analytical and simulated results. Blue bars are the averaged histograms from 10 rounds of 5000 Monte Carlo simulations. Red lines are the analytic results. Red dashed lines show the ranges of the variables. Horizontal axes are the values of d calculated from Equation 2.22 given the means and ranges in Table 2.1. Title of each subplot is the variable of choice.

the two variables satisfy a relation similar to Equation 2.19 as

$$d = ax + by + c, \tag{2.29}$$

where x and y are the two variables of choice, a and b are the corresponding coefficients in Equation 2.24, which are also constants. c is another constant because, except for the variables, other parameters are constant. Based on

Equation 2.20, the pdf of d is

$$f_d(d) = (af_x(x)) * (bf_y(y)). \tag{2.30}$$

For instance, assume S_1 and S_3 are the two uniformly distributed and independent variables, $f_d(d)$ is

$$\begin{aligned} f_d(d) = \int_{AS_{1min}}^{AS_{1max}} \int_{BS_3}^{d+C-D-AS_1} & \frac{1}{(S_{1max} - S_{1min})} \\ & \times \frac{1}{(S_{3max} - S_{3min})} dS_1 dS_3, \end{aligned} \tag{2.31}$$

where A, B, C and D denote the same as in Equation 2.24. There are six combinations of choosing two random variables that are linearly related to d in Equation 2.24. Figure 2.6 illustrate the analytical and simulated pdf's of d using the same means and ranges in Table 2.1. Again, there is a strong consistency between the analytical results and the simulated results. Comparing the analytical and the Monte Carlo simulation methods, we can see that the simulation method requires less calculation of the mathematical relation between the pdf of d and the variable. But it requires more computational time for the computer to generate reasonable results because the Monte Carlo simulations becomes more valid as the size of the simulations increases. As for analytical expressions, once the distributions of the variables are known, the pdf of d is easily calculated based on their relations. Unfortunately, the analytic expressions of such relations become quite involved in particular if multiple variables are considered that have non-linear relationships with d. In this case, Monte Carlo simulations are preferred.

Tornado diagram

Figure 2.7 shows how the variability in each parameter affects the variability of d in 2D scenario. Here we can see that with the same variance of 0.15, d is most sensitive to the minimum principal stress S_3. Such a tornado diagram illustrates the uncertainty of which parameter has a lager impact on the uncertainty in d.

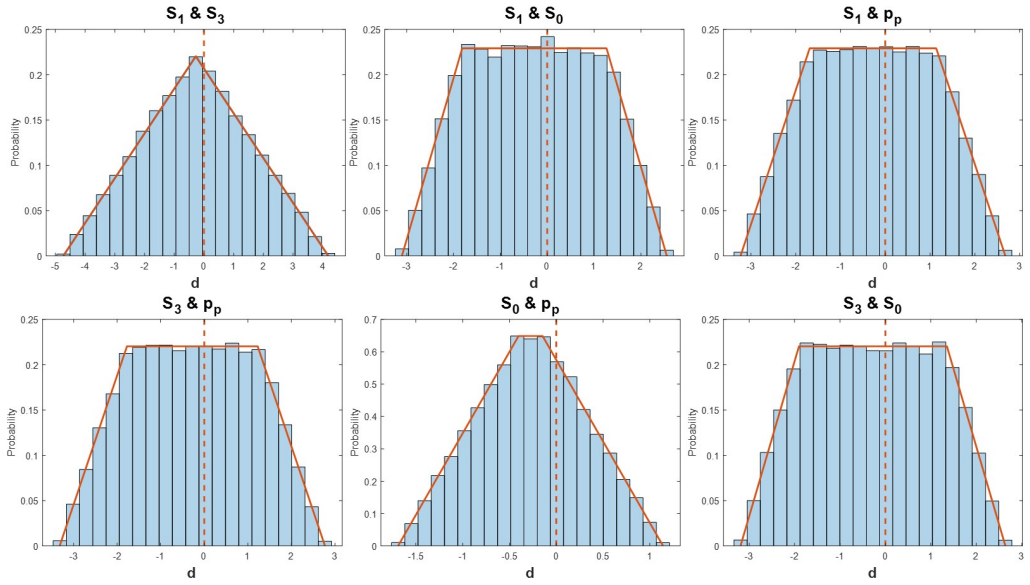

Figure 2.6: Analytic and simulated results. Blue bars are the histograms from Monte Carlo simulations and red lines are the analytic results. Title of each subplot is the two variables of choice. Horizontal axes are the values of d calculated from Equation 2.31 given the means and standard deviations in Table 2.1. Dashed red lines indicate $d = 0$. Failure occurs for $d < 0$.

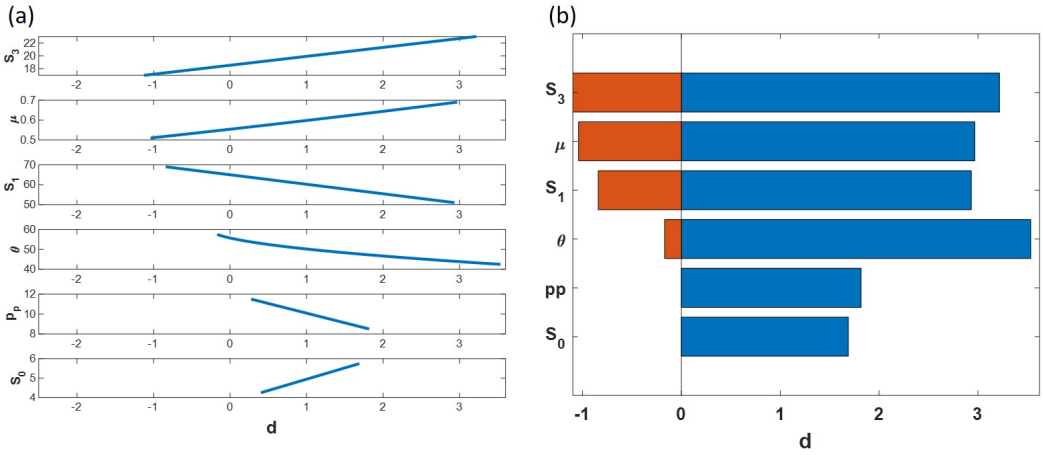

Figure 2.7: (a). Relation between each parameter and d with the parameter changing between the range given in Table 2.1. (b). The tornado diagram of d based on (a). d is calculated using Equation 2.22.

2.4 Fault slip potential analysis

CFC is easy to apply if all the parameters can be known with little to no uncertainties. However, if the quantification of the parameters is imperfect,

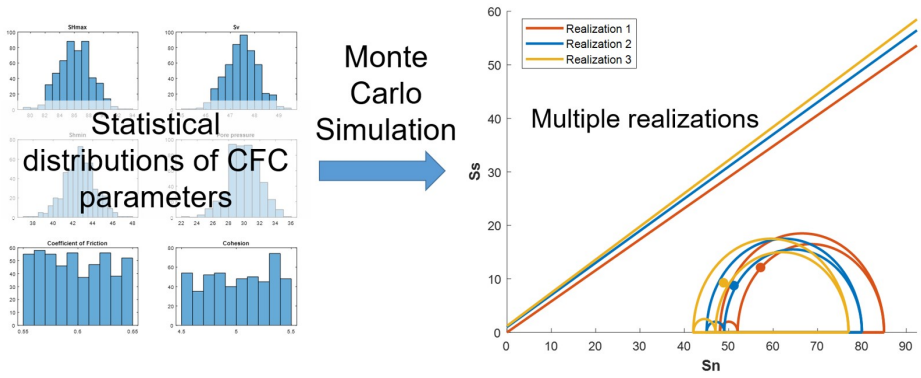

Figure 2.8: Workflow of FSP analysis. In one Monte Carlo simulation, values of the CFC parameters are generated based on the given statistical distributions as shown in the left part of the figure. Using the values, the stress state on the fault is calculated and analyzed using the CFC, as shown on the right part of the figure. Here three realizations are shown, circles are the 3D Mohr circles and the straight lines are the CFC. The dots on the circles represent the stress states. The FSP is the ratio between the number of realizations with fault reactivation and the total number of realizations.

uncertainties would lie within the results. FSP is proposed if the parameters have uncertainty (Walsh and Zoback, 2016). The idea behind this method is to quantify the risk of fault reaction by including the uncertainties of the CFC parameters via Monte Carlo simulations since analytical solutions become quite complex with multiple variables.

Figure 2.8 illustrates the workflow of FSP analysis. First step is to characterize the uncertainties in the input parameters. The uncertainties can be characterized using various methods, such as bootstrapping. Bootstrapping means resampling the variable based on the probabilistic distribution obtained from the existing samples (Tibshirani and Efron, 1993). The resampled population is then used for further analyses. Next, Monte Carlo simulations are conducted. In order to have a better result, a large number of realizations are recommended. For each Monte Carlo realization, CFC is applied to determine whether the fault will slip with the values generated based on the input parameters and their uncertainties. The FSP is the ratio of realizations with fault reactivation over the total number of realizations as

$$FSP = \frac{\text{Fault reactivation events}}{\text{Total realizations}}. \tag{2.32}$$

2.5 Conclusion

This chapter explained the theories related to the FSP analysis. Stresses acting on a fault plane can be vectorized into the normal and shear stresses. The normal and shear stresses are calculated using the relations between the traction on a plane and the plane normal. Then CFC determines if the fault plane fails under certain normal and shear stresses.

Considering the uncertainty in the quantification process of the relevant parameters, the FSP analysis is proposed to calculate the probability of fault reactivation. This analysis is based on the CFC. Instead of having a certain answer of if a fault will fail, the FSP analysis gives a likelihood of the fault failure given the current knowledge.

The FSP analysis utilizes the Monte Carlo simulations to determine the impact of the uncertainty on the probability of fault reactivation. The uncertainty in each variable contributes to the ultimate probability of fault failure. The impact can be known analytically. However, given the complexity of the numerical relations between the variables and the fault failure, analytical solutions in the FSP analysis are too difficult to solve. Hence Monte Carlo simulations are introduced to simulate the analytical solutions based on the Law of Large Numbers. Implementing Monte Carlo simulations makes the FSP analysis less complex. A detailed case study of the application of the FSP analysis is included in Chapter 3.

Chapter 3

Fault slip potential analysis - application

Summary

In this chapter, the original FSP analysis is modified by considering the depth variation in the stress gradients. Methods explained in Chapter 2 are applied and several faults identified in Fox Creek, Alberta are studied in detail. The case study demonstrates the practicability of the FSP analysis. It can be updated easily once more information is available. The slip direction and the safety distance are included in the 3D FSP analysis as well. The analysis explained in this chapter utilizes more information and is more comprehensive. The improved method helps better understand the likelihood of fault reactivation and how the uncertainty affects the likelihood.

3.1 Introduction

The original FSP method only considers constant stress gradients with depth. Since the stress gradients can vary with depth (Prats et al., 1981; Roche and van der Baan, 2017; Ma and Zoback, 2017; Zoback and Kohli, 2019), FSP analysis including the variations in principal stress gradients and pore pressure gradients with depth is proposed. The results from the FSP analysis show at

which depth the fault is more prone to slip. Also, the safety distance is included to study the variation of the FSP results. The slip direction of the fault is also calculated to validate the FSP analysis. To demonstrate the application of the FSP analysis, a case study in the Fox Creek region, Alberta, Canada is shown. The focus is on understanding and quantifying the probability of fault slip without addressing the potential impact associated with the slip.

In this chapter, the methodology of applying FSP analysis to assess the risk of AIS is first explained. Then a field example involving a hydraulic fracturing treatment and moderate-size seismicity with the maximum moment magnitude of M_w 3.2 is investigated. This chapter demonstrates how FSP can be useful in the risk assessment of AIS prior to treatment but also once more observations become available.

3.2 Method

FSP analysis, slip direction and safety distance are explained in detail in Chapter 2. Here, the approach applied for calculating the principal stresses is explained.

3.2.1 Principal stresses with depth

Principal stresses are required to determine the normal and shear stresses on a fault plane. Often, stress gradients are used to describe the horizontal principal stresses by dividing the stress measurements over depths (Shen et al., 2018). Nevertheless, determining the stresses at different depths using the gradients is not precise as measurements show that the minimum horizontal stress varies along depth and does not have a constant gradient (Ma and Zoback, 2017; Prats et al., 1981). Different explanations are proposed based on various assumptions, such as the stress relaxation and creep (Sone and Zoback, 2013; Prats et al., 1981), tectonic movements and rock properties (Roche and van der Baan, 2017; Economides and Nolte, 2000; Prats et al., 1981), or temperature (Prats et al., 1981). It is possible that a fault crossing multiple layers is under different stress states. Including the stress variations in vertical direction in FSP analysis not

only calculates the probabilities of reactivation of numerous faults, but also the probabilities of fault reactivation at various depths. At the same time, stress measurements at different depths in one region are limited, and most stress measurements are done within the depth range of the reservoir (Higgins-Borchardt et al., 2016). Different approaches are proposed for estimating the gradient variations of principal stresses (Jaeger et al., 2009; Savage et al., 1992; Economides and Nolte, 2000; Roche and van der Baan, 2017; Zoback and Kohli, 2019). Here the approach proposed by Roche and van der Baan (2017) is applied for demonstration.

The methodology of this model consists of two steps. Firstly, it assumes a state of uniaxial strain due to the overburden. The vertical effective stress σ_V and the horizontal uniaxial stress $\sigma_{\bar{H}}$ in the rock satisfy (Jaeger et al., 2009; Savage et al., 1992; Roche and van der Baan, 2017)

$$\frac{\sigma_{\bar{H}}}{\sigma_V} = \frac{\nu}{1-\nu}, \tag{3.1}$$

where ν is the Poisson's ratio of the rock. Secondly, the effects of tectonic stress and strain are included. A biaxial stress state is applied because only the horizontal tectonic stresses are considered (Economides and Nolte, 2000). The changes in the horizontal strains at the directions of maximum and minimum horizontal stresses, $\Delta\varepsilon_H$ and $\Delta\varepsilon_h$, are

$$\Delta\varepsilon_h = \frac{\Delta\sigma_H}{E} - \frac{\nu\Delta\sigma_h}{E} \tag{3.2}$$

$$\Delta\varepsilon_H = \frac{\Delta\sigma_h}{E} - \frac{\nu\Delta\sigma_H}{E}, \tag{3.3}$$

where $\Delta\sigma_H$ and $\Delta\sigma_h$ are the changes in the horizontal effective stresses, $\Delta\varepsilon_H$ and $\Delta\varepsilon_h$ are the changes in the horizontal strains, and E is the Young's modulus. A similar calculation of the effective horizontal stresses is proposed by Higgins-Borchardt et al. (2016), in which the poroelastic effect is also considered. For simplicity, Biot's coefficient, the indicator of how strong the poroelastic value is within the rocks, is assumed to be 1 in all directions.

$\Delta\sigma_H$ and $\Delta\sigma_h$ can be calculated by subtracting the uniaxial horizontal stress

from the effective horizontal stresses as the following,

$$\Delta\sigma_h = S_{hm} - p_p - \sigma_{\bar{H}}, \tag{3.4a}$$

$$\Delta\sigma_H = S_{Hm} - p_p - \sigma_{\bar{H}}, \tag{3.4b}$$

where p_p is the pore pressure, S_{Hm} and S_{hm} are the measured in situ maximum and minimum horizontal stresses. Because in the uniaxial strain model, the horizontal strains are zero, tectonic strains are the only strains considered in the horizontal directions. In addition, since both maximum and minimum horizontal strains are assumed constant in all layers, the variations in horizontal stresses depend on the variances in E and ν according to Equation 3.2 and Equation 3.3. Hence, horizontal stresses in other layers can be calculated using the reciprocal versions of Equation 3.2 and Equation 3.3 as

$$\Delta\sigma'_h = \frac{E'}{1-\nu'^2}\Delta\varepsilon_h + \frac{E'\nu'}{1-\nu'^2}\Delta\varepsilon_H, \tag{3.5a}$$

$$\Delta\sigma'_H = \frac{E'}{1-\nu'^2}\Delta\varepsilon_H + \frac{E'\nu'}{1-\nu'^2}\Delta\varepsilon_h. \tag{3.5b}$$

The apostrophe ($'$) denotes the stresses and strains in the layers with different E and ν. E and ν can be inverted using the relations between elastic moduli and seismic wave velocities (Yilmaz, 2001),

$$\nu = \frac{1}{2}\frac{(V_p/V_s)^2 - 2}{(V_p/V_s)^2 - 1}, G = \rho V_s^2, E = 2G(1+\nu), \tag{3.6}$$

where V_p and V_s are the velocities, G is the shear modulus. Velocities can be obtained from well logs. ν and E calculated from seismic velocities are dynamic properties, which should be compared with static moduli measured with core samples. Static elastic moduli are different from the dynamic moduli. Static moduli refer to the direct measurements of the moduli in laboratories, where dynamic moduli are derived from the compressional (P-wave) and shear (S-wave) wave velocities (Zoback, 2010). Because differences rise between static and dynamic elastic properties, it is important to distinguish between these two types. The static elastic properties describe the rock behaviours more ac-

curately (Eissa and Kazi, 1988). The relations between the dynamic and static moduli vary place by place and rock by rock. Often, laboratory tests are done to quantify this relation (e.g. Mullen et al., 2007). The static moduli should also be calibrated to match the condition of the confining pressure around the rock in the ideal depth. When applying different confining pressure, the static moduli of the same rock change (Najibi and Asef, 2013). The calibrated static moduli are used for further calculations.

3.2.2 Measuring principal in situ stresses and pore pressure

The strain model requires stress measurements at least in one formation for calibration. The vertical stress S_v at a certain depth is calculated by integrating the density with the depth (Zoback, 2010; Jaeger et al., 2009),

$$S_v = \int \rho g dz, \tag{3.7}$$

where ρ is the density from the well log, g is the gravitational acceleration, and S_v is the vertical stress.

S_{hm}, S_{Hm} and p_p can be measured using hydraulic fracturing (Zoback, 2010; Shen et al., 2018). With the measurements of S_{hm} and maximum horizontal S_{hm} at the same depth, and the calculated elastic properties with well logs using Equation 3.6, the horizontal stresses in depth can be calculated based on Equation 3.4 and 3.5.

3.3 Case study

To demonstrate how the FSP analysis is implemented in the risk assessment and management of AIS, an area located at the east of Fox Creek, Alberta, Canada is studied. This area is also studied for other purposes in Zhang et al. (2019); Eaton et al. (2018); Rodriguez-Pradilla (2018); Igonin et al. (2019) and Poulin et al. (2019).

3.3.1 Geological background

Lithological analysis

This region is known for the presence of unconventional resources in the Duvernay formation lying within the Western Canada Sedimentary basin. It is an active area of hydraulic fracturing operations. Here seismic data, well logs, microseismic data, stress measurements as well as core samples in this area are studied.

Velocity logs, density logs and gamma-ray logs from the wells located in the center of the study area are obtained to determine the depth and rock properties of each formation. Figure 3.1(a) shows the well logs, along with the interpretation of the formations. A detailed analysis of the same well logs is included in Rodriguez-Pradilla (2018).

The interpretation of the well logs indicates that the Duvernay formation is at about 3500m depth in the study area with a thickness around 70 meters (Rodriguez-Pradilla, 2018). Above lie the Banff, Wabamum, Winterbum, Upper and Lower Ireton formations. Formations below are interpreted from seismic data. They are Swan Hill, Gilwood and Precambrian respectively. The Duvernay formation is an organic and clay-rich formation, with average total organic carbon (TOC) of 4.5 wt% (Preston et al., 2016; Dunn et al., 2012). Above the Duvernay is the Ireton, containing mostly shale. The Ireton is divided into two layers with increasing clay and decreasing carbonate content from the Upper Ireton to the Lower Ireton (Switzer et al., 1994). The formations below Duvernay also transit from organic and clay-rich shale to mudstone. The Precambrian basin consists of crystalline rocks at around 4000m below the surface.

With the density logs and velocity logs, the dynamic E and ν are calculated using Equation 3.6. As mentioned above, the Duvernay formation has a higher organic and clay content where the formations above and below it have a lower clay content. The lithological analysis means that the elastic properties would change through these formations, as shown in Figure 3.1. E and ν decrease with the increase in TOC (Sone and Zoback, 2013). The measurements of three core samples retrieved from the Duvernay formations are listed in Table 3.1.

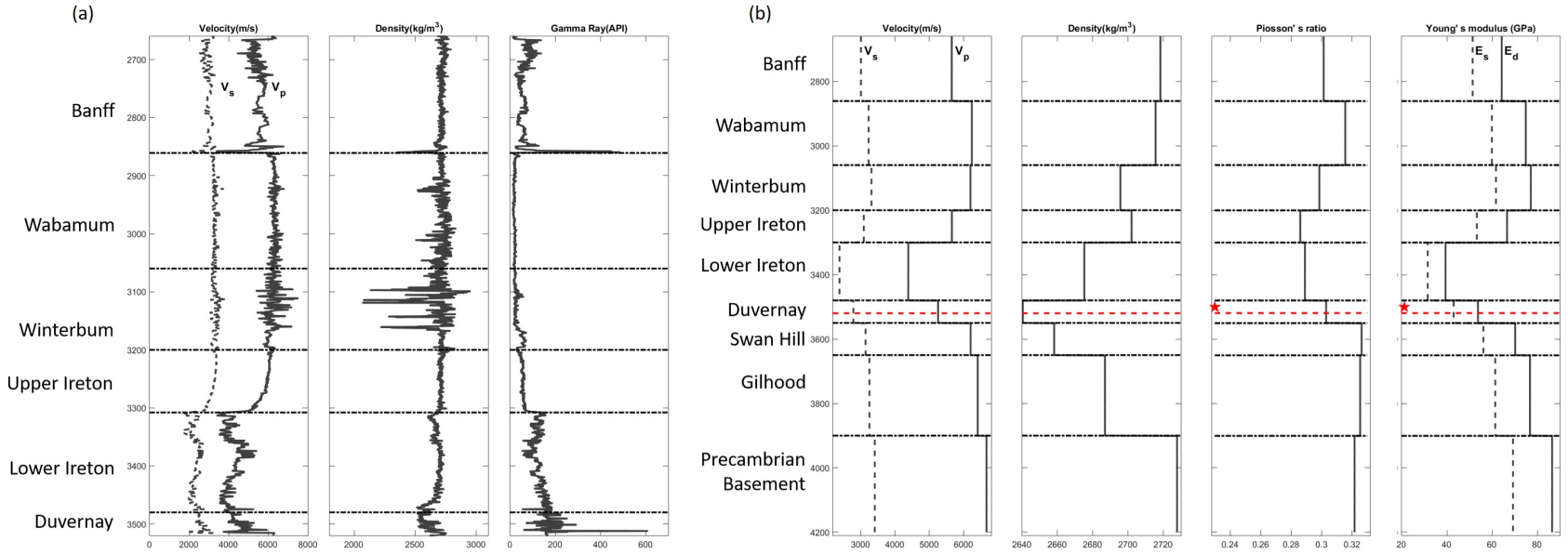

Figure 3.1: Well log and profiles of different rock properties. Horizontal black dashed lines indicate the formation boundaries. Formation names are listed at the left side. (a). Well logs obtained from one vertical well in the study area. Data can be found in Rodriguez-Pradilla (2018). (b). Profiles of rock properties in different formations used for further analysis. Red dashed lines indicate the end of the well logs in (a). Average values are shown in each formation above the red dashed lines. Values are given for the formations below the red lines with no well logs. Red stars are the lab measurements listed Table 3.1. V_p and V_s are the velocities of the primary and secondary waves. E_d and E_s are the dynamic and static Young's modulus. The ratio between E_s and E_d is 0.8. Detailed calculation is explained in the text.

Table 3.1: Triaxial compressing measurements of the core samples at the Duvernay retrieved from two wells in the study area. Data are available at the geoSCOUT® QFind module with subscription.

No.	Depth(m)	Confining Pressure(MPa)	Young's Modulus (GPa)	Poisson's Ratio
1	3615.28	5.6	21.17	0.23
2	3639.62	5.6	22.62	0.23
3	3632.94	5.6	21.95	0.23

In situ stresses

Because the well logs end at the Duvernay formation, values of velocities, densities and other properties are assigned for the formations below the Duvernay. In each identified formation, constant values are assigned. For formations with well logs, for simplification, the means are used. Profiles of rock properties are shown in Figure 3.1(b).

Since the confining pressures applied in the laboratory are lower than the overburden calculated from the density log, the static elastic properties in the in situ stress environment should be higher than the values listed in Table 3.1. This is because higher confining pressure results in higher Young's modulus and Poisson's ratio (Wu et al., 2019). A ratio of 0.8 between the static and dynamic properties is applied according to the study conducted by Mullen et al. (2007).

Based on the stress analysis of the Western Sedimentary Basin (e.g. Bell et al., 1990; Shen et al., 2018; Cui et al., 2013), the study area is located in a strike-slip stress region. The principal stresses of the Duvernay formation, as well as the rock properties (coefficient of friction μ and cohesion S_0) at the Duvernay formation in Alberta are obtained from Shen et al. (2018) and Heidbach et al. (2016). Stress and rock measurements and their variances at the Duvernay formation in the study area are shown in Table 3.2. Different distributions are assigned. For principal stresses (S_{hm}, S_{Hm} and S_v), pore pressure p_p and the azimuth of S_{Hm} β, a Gaussian distribution is used. For rock mechanical properties μ and S_0, a uniform distribution is used. Here the bootstrapping method is not applied as used in the original paper from Walsh and Zoback (2016). The reasons are the study area is relatively small compared to that in the original paper, and there are limited published stress

Table 3.2: Stress measurements and rock properties of the Duvernay within the study area. Data are from Shen et al. (2018) and Heidbach et al. (2016).

S_{Hm}	S_{hm}	P_p	Azimuth of S_{Hm}	μ	S_0
33±2 kPa/m	20.8-21.5kPa/m	15.2-17.9kPa/m	45±2(°)	0.45-0.65	0-1 MPa

measurements in this area.

Identification of faults

Figure 3.2 shows a seismic cross section of the study area. Most of the faults in this area are difficult to locate since there is no vertical displacement, indicating they are strike-slip faults. Figure 3.3 shows the faults in this area from the

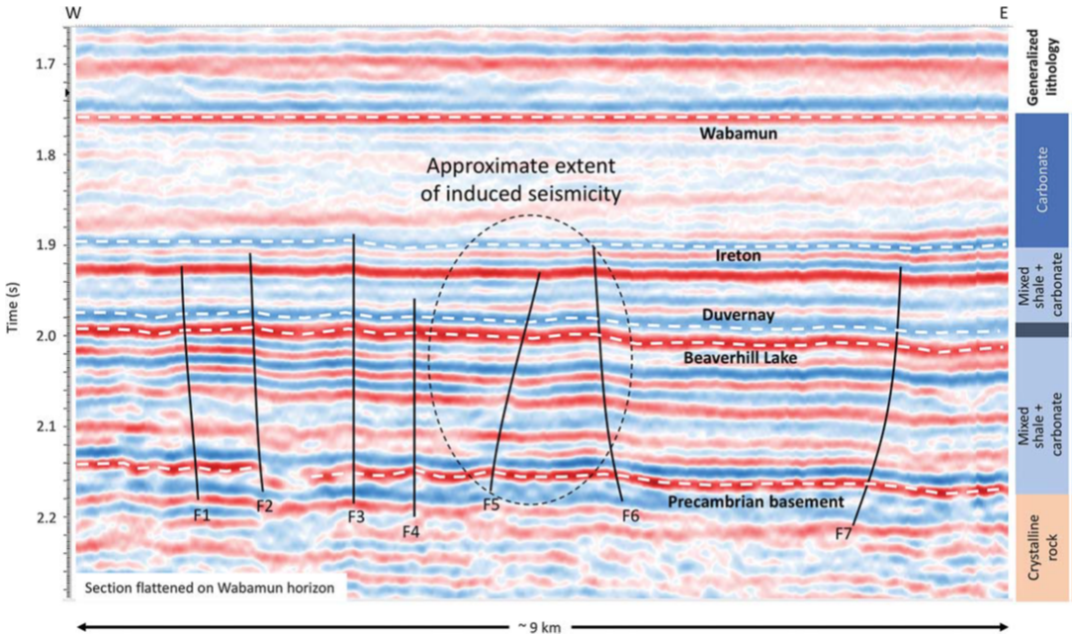

Figure 3.2: Seismic cross section trending east-west. The section is compressed in the lateral direction and flattened on the Wabamum horizon. Faults are marked with black solid lines. Red and blue colors represent the positive and negative seismic amplitude values. White dashed lines are formation boundaries. Figure from Eaton et al. (2018).

interpretation of the seismic data. A detailed analysis of the seismic data can be found in Weir et al. (2018). Because most of these faults are strike-slip faults, the chance of misinterpretation is relatively high compared to regions

with normal or thrust faults.

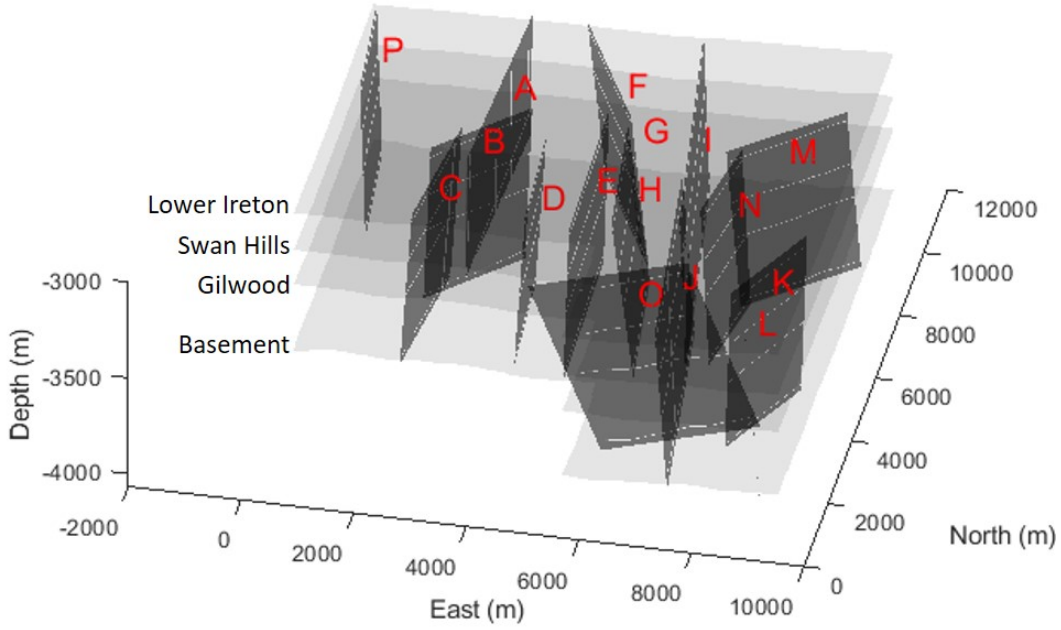

Figure 3.3: Map view of the faults interpreted from the seismic data used in Weir et al. (2018) and Eaton et al. (2018). Faults are represented by darker gray planes with names in red capital letters. Light gray horizontal planes are the formation boundaries with names on the left side. The Duvernay lies between the Lower Ireton and the Swan Hill. Data offered by Dr. David Eaton from the University of Calgary.

3.3.2 Results

Stress inversion

There are three states of pore pressure in rock, hydrostatic, overpressured and underpressured (Zoback, 2010). Hydrostatic state exists in most of the rock. An overpressured state is often observed in the unconventional reservoirs. In this study, the Duvernay is overpressured due to the presence of the reservoir. As for the pore pressure in the rest formations, two different cases are proposed, namely Case 1 and Case 2. In Case 1, only the formation with the reservoir, the Duvernay formation, is overpressured. In Case 2, the overpressured state exists in the formation containing the source rock and the formations adjacent

to it, namely the Duvernay, the Lower Ireton and Swan Hill formations.

To calculate the stress profiles using the method proposed by Roche and van der Baan (2017), which is mentioned above, measurements of the principal stresses in at least one formation should be known. Here the measurements of the horizontal stresses in the Duvernay formation in the study area are used. They are listed in Table 3.2. Figure 3.4(a) shows the stress gradients calculated based on the averaged well logs and static elastic moduli in Case 1, where only the Duvernay formation is overpressured. The pore pressure is measured at the Duvernay. The stress gradient shows a constant strike-slip stress regime regardless of the changes in the gradients. Figure 3.4(b) lists the Mohr diagrams at all formations. Figure 3.5 show the stress gradients calculated based on Case 2 and the corresponding Mohr diagram in each formation.

For formations with faults, the stress states on the faults are calculated and colored with red, yellow and green based on the safety distances. Red means close and green means far. The faults shown in red and yellow dots can be considered as being at risk of reactivation. From Figure 3.4(b) and Figure 3.5(b), we can see that more faults are at risk at the Lower Ireton and Swan Hill in Case 2 than in Case 1, a result from the increased pore pressure in these two formations. In addition, due to the overpressured stress state, several faults are at a high risk (red dots) at the Duvernay in both cases. The overpressured state decreases the safety distance between the fault and the failure line, making the fault closer to reactivation. Because no uncertainty is given in the Mohr diagrams, Figure 3.4(b) and Figure 3.5(b) are preliminary analyses.

The pore pressure change can be calculated using the pore pressure diffusion theory (Shapiro et al., 2002; Eaton, 2011). The closest fault to the planned injection wells is fault E, which is within $100 - 150m$ of two injection wells. The locations of the wells and the faults is shown in Figure 3.7(b). With the assumption that the permeability of a typical shale gas reservoir is $50mD$, the pore pressure perturbation at the fault E is less than $0.2MPa$. The detailed explanation and analysis can be found in Appendix A. The increase in the pore pressure is too small to reactivate the fault. It is even smaller than the uncertainty assigned to the pore pressure. Therefore, the perturbation in the

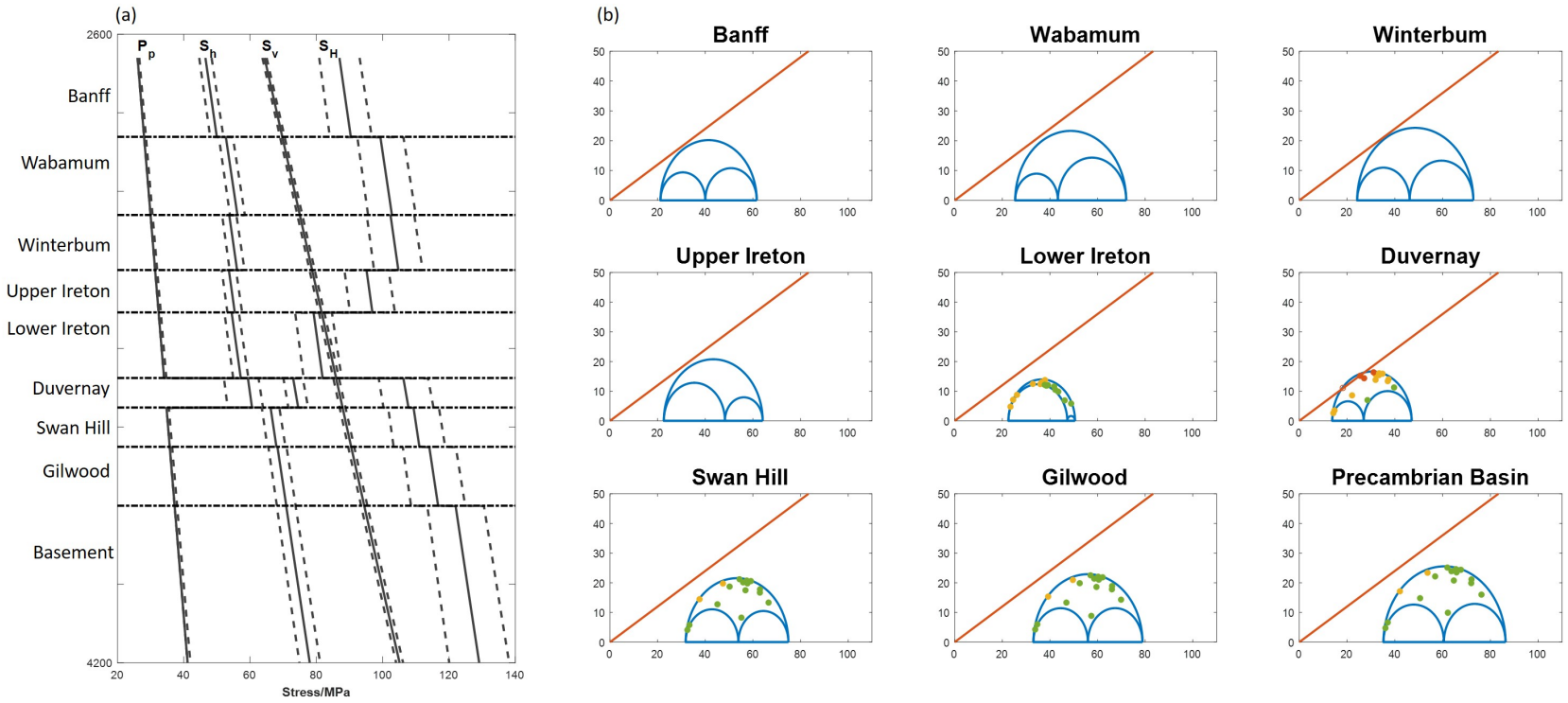

Figure 3.4: Stress gradients and Mohr diagrams of Case 1 where the overpressure exists in the Duvernay. (a). Gradients of principal stresses and pore pressure. p_p, S_h, S_v, and S_H represent the pore pressure, minimum horizontal stress, vertical stress and maximum horizontal stress respectively. Solid lines are the stresses directly calculated based on the rock properties in Figure 3.1(b) and stress measurements at the Duvernay in Table 3.2 using the stress interpretation model by Roche and van der Baan (2017). The dashed lines close to the solid lines indicate the uncertainty ranges given to each stress during the FSP analysis. Horizontal dashed lines are the formation boundaries. (b). Mohr diagrams of the formations using the stresses indicated by the solid lines in (a). Names of the formations are shown above the diagrams. The CFC is the red solid line. At formations with faults crossing, the stress state at each fault plane is calculated and shown as dots in the Mohr diagram. The color of the dot is based on the distance between the dot and the line of CFC.

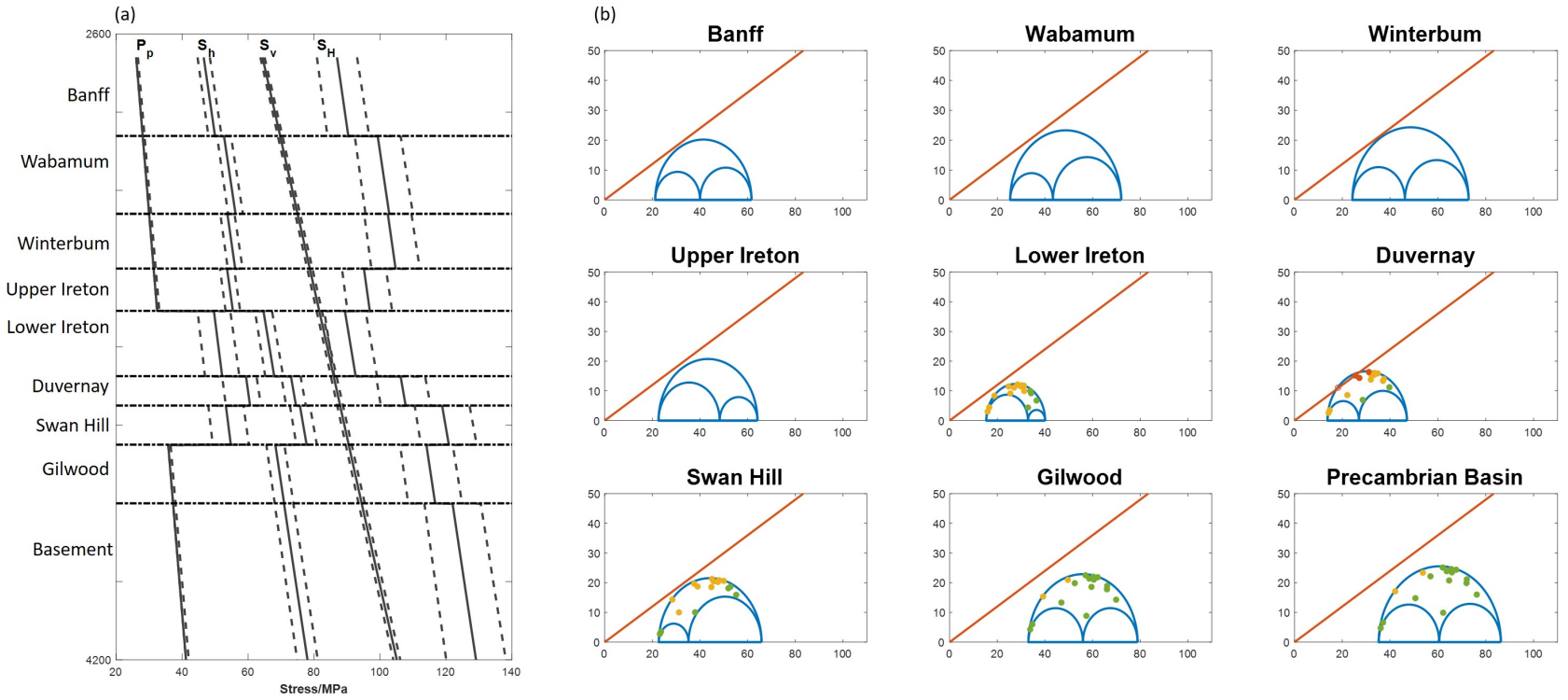

Figure 3.5: Stress gradients and Mohr diagrams of Case 2 where the overpressure exists in the Lower Ireton, the Duvernay and the Swan Hill. (a). Gradients of principal stresses and pore pressure. p_p, S_h, S_v, and S_H represent the pore pressure, minimum horizontal stress, vertical stress and maximum horizontal stress respectively. Solid lines are the stresses directly calculated based on the rock properties in Figure 3.1(b) and stress measurements at the Duvernay in Table 3.2 using the stress interpretation model by Roche and van der Baan (2017). The dashed lines close to the solid lines indicate the uncertainty ranges given to each stress during the FSP analysis. Horizontal dashed lines are the formation boundaries. (b). Mohr diagrams of the formations using the stresses indicated by the solid lines in (a). Names of the formations are shown above the diagrams. The CFC is the red solid line. At formations with faults crossing, the stress state at each fault plane is calculated and shown as dots in the Mohr diagram. The color of the dot is based on the distance between the dot and the line of CFC.

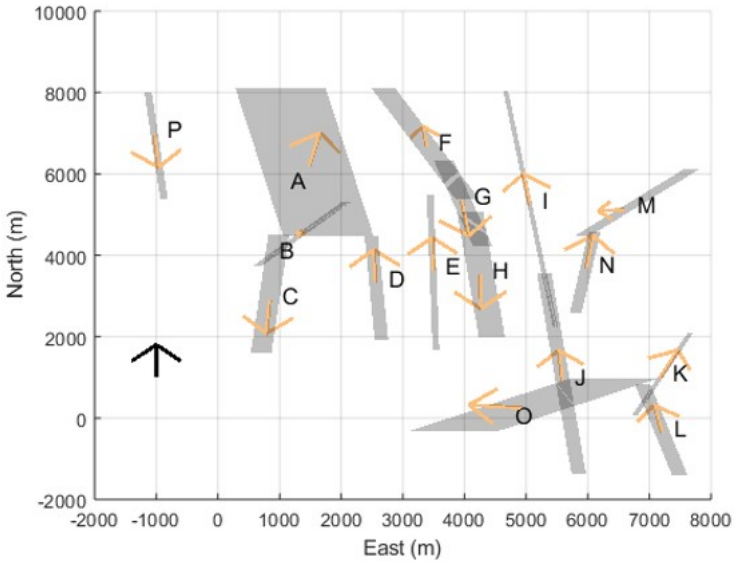

Figure 3.6: Projection of the slip directions on the surface. Faults are represented by light gray planes. Slip directions are shown in arrows. The length of the arrow on the left corner is one unit, indicating a horizontal slip movement.

pore pressure due to injection is not included in the FSP analysis.

Slip direction

If the poroelastic effect is ignored, the ratios of the effective principal stresses do not change, hence the slip directions remain the same before and after the treatment. Based on Equation 2.11, the slip directions of all faults are calculated using the stresses without uncertainty in the Duvernay, as illustrated in Figure 3.6. Slips are predominantly strike-slips, which is expected since the stress field is a strike-slip stress field (Cui et al., 2013; Bell and Grasby, 2012).

FSP analysis prior to the injection

For the FSP analysis, in each Monte Carlo simulation, the values of all the parameters are generated based on the stresses and their variances at different formations shown in Figure 3.4(a) and Figure 3.5(a) and the geomechanical properties listed in Table 3.2. The stress state of each fault at each formation are calculated based on Equation 2.3 and Equation 2.9. Then the CFC is

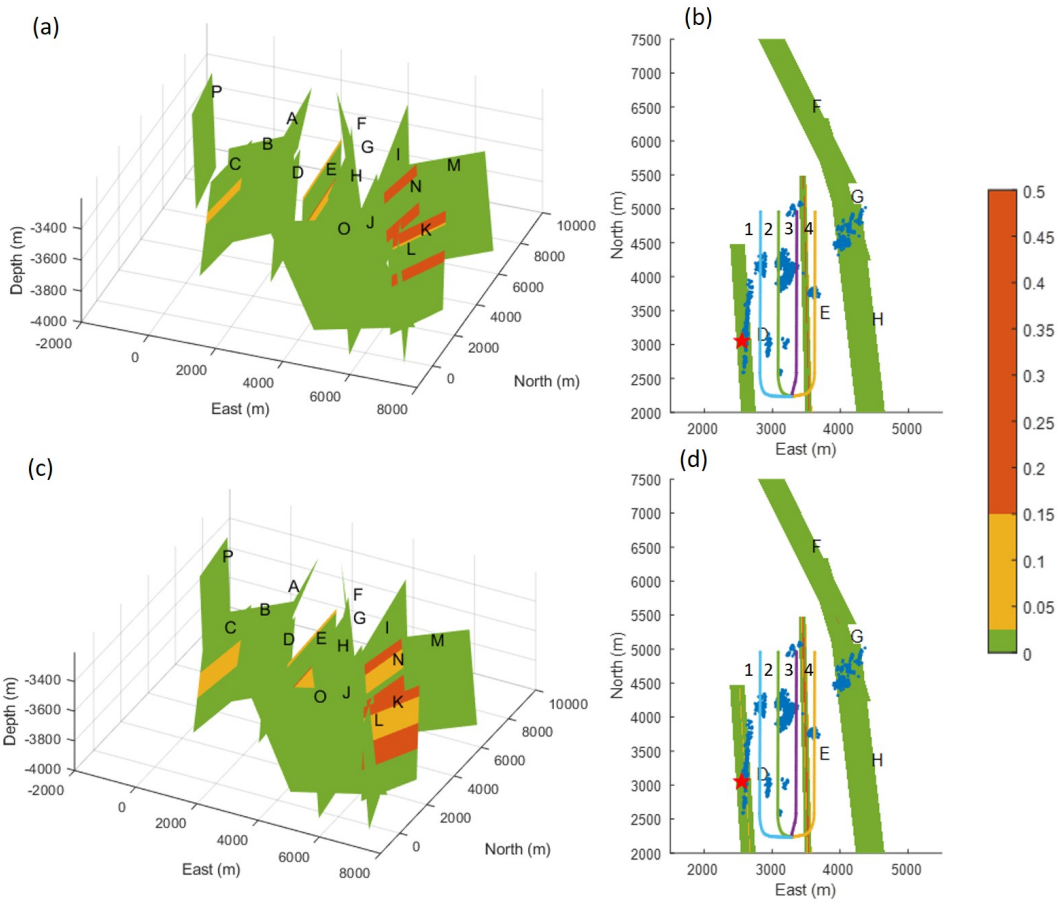

Figure 3.7: FSP analysis and comparison with the observed AIS. (a). FSP of all faults in Case 1. (b). Comparison between the FSP results in Case 1 and the AIS during the treatment. The figure is in a map view. (c). FSP of all faults in Case 2. (d). Comparison between the FSP results in Case 2 and the AIS during the treatment. In (a) and (c), fault planes are colored based on the FSP in each formation. The color bar on the right shows how the FSP is colored. In (b) and (d), four horizontal wells are named 1-4. Blue dots are the observed AIS. Red star is the location of the maximum AIS with M_w 3.2.

applied to determine whether the fault is considered being reactivation in this simulation. Figure 3.7(a) and (c) show the FSP results of all faults in Case 1 and Case 2. Most of the faults have FSP's smaller than 5%, indicated by the color green. This means that the faults are stable and have low possibilities of being reactivated under the current stress field without the injection. Similar to the analysis of the Mohr circle plots in Figure 3.4(b) and Figure 3.5(b), most of the faults are far from the failure line, indicated by green dots. Faults with

yellow and red segments are more likely to be reactivated at those depths under the current stress field and given uncertainty, such as faults C, E, K, and N in Figure 3.7(a) and (c).

Distribution of the safety distance

The pdf of safety distance d is a combination of the contributions of all the variances in the input parameters. The pdf give insights into the uncertainty in the input parameters as well as the likely outcomes. A wider distribution indicates a larger spread in possible outcomes.

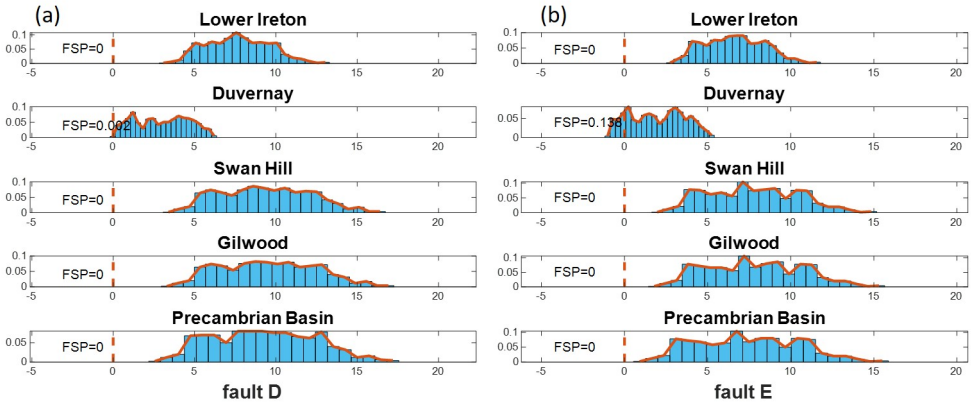

Figure 3.8: Pdf of d of faults D and E in Case 1. FSP in each formation is shown at the left of each plot. Red dashed lines are $d = 0$. The title of each plot is the formation where the d is calculated during the FSP analysis.

Figure 3.8 shows the pdf's of d of fault D and fault E in Case 1. The wide distributions of d in all formations indicate poorly constrained input parameters, which means a refinement is needed for a more precise prediction.

Figure 3.7(a) and (c) show the fault D as a green plane, indicating low probabilities of reactivation of fault D in both Case 1 and Case 2. However, the wide distributions of d in Figure 3.8(a) show the results from the FSP analysis contain large uncertainty due to all the variances given to the input parameters. Pdf's of d of fault E also have wide distributions, as shown in Figure 3.8(b). If fault E or D is near the operation area, then refining its geomechanical and stress parameters prior to treatment may be advisable. Likewise, a reduction in treatment volumes or skipping stages should be considered if fault E during

stimulation begins to display sustained microseismicity that aligns along the fault plane.

Comparison with recorded AIS during the operation

A hydraulic fracturing operation was conducted adjacent to faults D to H. The operation consisted of injection in four south-north horizontal wells, named Wells 1-4 from the west to east. The injection first started in Well 2. Then, Well 3 and Well 4 were hydraulic-fractured interchangeably. Well 1 was fractured last. A series of AIS was recorded with the maximum moment magnitude (M_w) of 3.2 (Eaton et al., 2018). To better study the FSP analysis, the recorded AIS is plotted in Figure 3.7(b) and (d) with the FSP analysis of Case 1 and Case 2. Here all the movements of the faults and fractures are assumed to be seismic.

Comparing the locations of AIS and the faults, part of the AIS lines up with fault D and another cluster of AIS was at faults G and H. No indication of any movement on fault E, which has a higher possibility of reactivation in the FSP analysis. Meanwhile, the M_w 3.2 earthquake happened at the location of fault D. It is reasonable to connect this earthquake with the reactivation of fault D.

3.4 Discussion

3.4.1 Principal stress and pore pressure

To measure the in situ stresses, most techniques are usually more suitable for shallow formations and strong rocks with low temperatures; the depths of unconventional formations are usually too deep and hot to obtain accurate measurements via these methods (Zoback, 2010). Therefore, other indirect calculations can be applied, such as the focal mechanism (Zoback, 2010; Zhang et al., 2019). At the same time, stress interpretation based on the critical stress state is not suggested. This approach assumes the most optimally orientated faults are at the edge of slip as the failure line is the tangent of the outer Mohr circle (Zoback, 2010; Roche and van der Baan, 2017). If S_{Hm} is calculated based on this assumption, the FSP results would be high as it already assumes

a critically stressed state. This could be beneficial from the perspective of risk assessment, yet it biases the judgments and decision-making processes as it potentially magnifies the FSP. Therefore, the methodology proposed by Roche and van der Baan (2017) to calculate the stress gradients in depth is applied. This methodology uses a strain-driven model and assumes the horizontal layers are not coupled. If other assumptions, such as stress-driven and coupled layers, are applied, the interpretation of the horizontal stress gradients could be different. Because the focus in this thesis is not to compare different stress interpretation methods, this method is adopted for demonstration. In addition, uncertainty is included when conducting the FSP analysis. The uncertainty could overcome the differences originated from using different assumptions and methods to estimate in situ stress. According to Equation 3.4, the pore pressure is also involved with the calculations of horizontal stress. Understanding the pore pressure gradient is as important.

For unconventional reservoirs, the rock is usually both the source and reservoir, which indicates it can be overpressured due to the continuous maturation of the kerogen (Higgins-Borchardt et al., 2016). Measurements have shown an overpressured state in the Duvernay formation at the study area (Shen et al., 2018). For other formations above and below the Duvernay, the pore pressure is rarely measured. Alternative approaches for interpreting the pore pressure gradients are proposed, such as calculating the pore pressure gradient using the empirical relation between the pore pressure and the seismic velocities (Eaton, 1975; Bowers et al., 1995; Sayers, 2006; Zhang, 2011). Here the idea illustrated by Higgins-Borchardt et al. (2016) is adopted, where the pore pressure is overpressured in the reservoir formation and transits to the hydrostatic state in other formations, as shown in Figure 3.9.

Because of limited pore pressure measurements, how the pore pressure transits from an overpressured state to a hydrostatic state is unknown. Therefore two possible cases to describe the pore pressure, Case 1 and Case 2, are proposed. In Case 1, the overpressured state only exists in the Duvernay. In Case 2, overpressured states exist in the source rock layer, the Duvernay, and the adjacent layers, the Lower Ireton and the Swan Hill. According to Shen et al. (2018), the pore pressure in the Duvernay is $16.5kPa/m$ in the study area. In

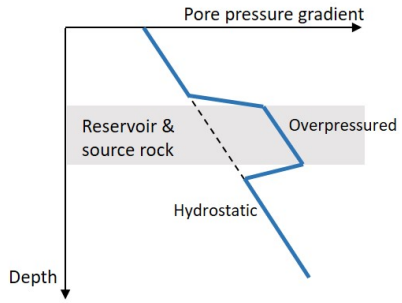

Figure 3.9: Pore pressure gradient change. Black dashed line indicates the pore pressure gradient. Figure not drawn to scale. Figure created based on Higgins-Borchardt et al. (2016).

Case 2, a pore pressure gradient of $15kPa/m$ is given to the other two adjacent layers. Comparing Figure 3.4(b) with Figure 3.5(b) we can see that the overpressured state generally decreases the distances between the Mohr circles and the failure line, making the stress state more critical for failure.

3.4.2 Comparison between the moment tensor inversion and the slip direction prediction

Slip directions of the faults are calculated using the same parameters in the FSP analysis. Therefore, the slip directions can be used to validate the input values for FSP analysis once more microseismic and seismic data are acquired. A contradiction between predicted slip directions and observed ones indicates most likely incomplete or incorrect information in the stress states and/or fault properties. If the microseismic and seismic data start to show alignment with an observed fault, and the focal mechanism of the seismicities corresponds with the predicted fault slip direction, this means:

1. The interpretation of the fault is correct.
2. The fault could be slipping.
3. The input values for the slip direction calculation are within the correct range.
4. The FSP analysis based on the input values is reliable.

Figure 3.10 shows the focal mechanisms of the seismic events in the area. The beach balls show that the M_w 3.2 event was strike-slip trending north-south. Our prediction of the slip direction of fault D also suggests the similar strike-slip pattern and direction. This indicates that this event is likely resulted from the reactivation of fault D. This could also validate that the stress regime in this area is a strike-slip regime.

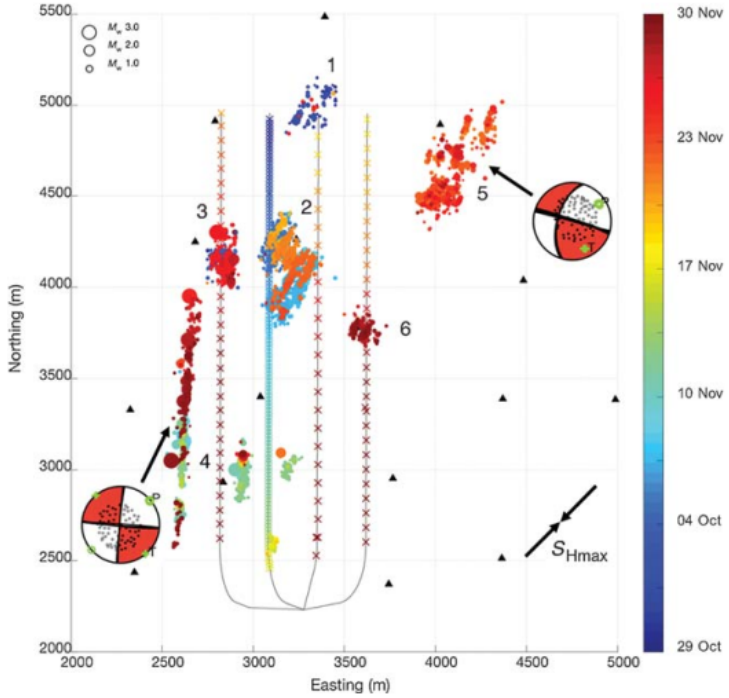

Figure 3.10: Focal mechanism analysis of the observed AIS during the treatment. The beach ball on the left side is the focal mechanism of the maximum AIS with M_w 3.2. Colored dots are recorded microseismic and seismic events during the operation. Figure from Eaton et al. (2018).

3.4.3 Comparison between the seismic observations and FSP results

The FSP analysis can be amended once passive-seismic data become available during the treatment. With additional information, the FSP analysis is updated. Comparisons of the moment tensor inversion, the seismic events and the FSP results demonstrate that there are some discrepancies as well as some

consistencies between the initial FSP analysis and the observations. As shown in Figure 3.7(b) and d, AIS aligned with fault D, while no AIS was observed at fault E. A cluster of AIS was observed at the the conjunction of faults G and H, both of which have low possibility of reactivation in the initial FSP analysis.

Various causes exist and some of them are listed below.

1. There is no fault E. Most faults are strike-slip faults in this area that are very hard to identify in seismic sections, as shown in Figure 3.2. With highly compressed cross sections strike-slip faults are interpreted by aligning topographic variations, but no slip or discontinuities in the cross section are visible.

2. The impact of the uncertainty is too large. As discussed above, the wide distributions of d show that the input parameters are poorly constrained. The large uncertainty could also lead to imprecise FSP analysis.

3. The movements at fault E could be aseismic slips that were undetectable. Aseismic movements are possible during the injection (Eyre et al., 2019). Because only seismic movements can be recorded, aseismic movements on faults are undetectable. If the movement on fault E is aseismic, no seismic events would be shown around fault E.

4. The local stresses could be different around large faults. Faults F, G, and H are connected and can be regarded as one large fault with three segments. The azimuth of S_{Hm} could alter at this large fault, based on the observations at other locations (Yale, 2003). Since a constant azimuth of S_{Hm} is applied at the initial FSP analysis, it is possible that this azimuth does not apply to the local stress azimuth around faults F, G, and H.

Though the FSP analysis does not match with the observations of AIS, this example still illustrates the application of the FSP analysis in depth. More importantly, the FSP analysis quantifies the possibility of fault reactivation. This quantification can help operators be aware of the potential risk of proceeding the operation and be prepared if seismic events with larger magnitudes do occur.

3.4.4 Update of FSP analysis

The knowledge of the study area is updated with the observed microseismic and seismic events during the operation. Therefore the FSP analysis is also updated. Several changes are made to the FSP analysis.

1. Fault E is eliminated since its existence is not confirmed by the seismicity.

2. The pore pressure gradient is updated by combining Case 1 and Case 2. The updated pore pressure state is called Case 3. In Case 3, the Lower Ireton is overpressued while the Swan Hill is hydrostatic. This change is based on the depths of observed seismic events. Both microseismic and seismic events clustered in the Duvernay and Ireton (Igonin et al., 2019).

The patterns of recorded microseismic and seismic data demonstrate that fluid pathways exist, for instance, due to the existence of a fracture network. Igonin et al. (2019) propose the existence of a highly developed fracture network in this area. The fracture network increases the permeability of the reservoir. So the pore pressure perturbation due to fluid injection was $2MPa$ rather than less than $0.2MPa$ as was initially calculated. The stress gradient profile and the corresponding Mohr diagrams of Case 3 are shown in Figure 3.11. The Mohr diagrams indicate that the stress states in the Lower Ireton and the Duvernay are closer to the failure line than the stress state in the Swan Hills. This means that both the Lower Ireton and the Duvernay are more critically stressed than the Swan Hills. Therefore more seismic events are observed in the Ireton and the Duvernay.

Figure 3.12(a) shows the updated FSP analysis with the stress profiles in Case 3. In the updated results of the FSP analysis, fault D has a higher probability of reactivation. Comparing the updated FSP analysis with the recorded AIS, shown in Figure 3.12(b), there is a better consistency between the updated FSP analysis and the observations.

3.5 Conclusion

This chapter demonstrates that the vertical stress variations could result in changes of FSP with depth. FSP provides the likelihood of fault reactivation

under the current understanding of relevant parameters. The slip direction is a way to validate the inputs of the FSP analysis. The pdf's of safety distance d capture the influence of uncertainty on the FSP results.

The analysis can be done prior to a hydraulic fracturing treatment to obtain a better understanding of the risk of AIS in one area. It can be easily updated once new information becomes available during the treatment, as demonstrated by the case study.

In a word, FSP is a fast and easy way to assess the likelihood of fault reactivation. Along with the size and the location of the fault, people can assess the risk of AIS by anticipating the possible magnitude and damage the fault reactivation can lead to. The results of FSP analysis can also be used during the economic assessment of the operation (Zhang and van der Baan, 2019a). Calculating the FSP is not complicated but the interpretation and application of the results are important and should be done with caution. If the impact of the uncertainty is too large, a sensitivity analysis would help to determine which parameters are first to be refined for an improved prediction, such as the tornado diagram in Figure 2.7. To refine the quantification of a parameter, additional measurements of that parameter is reasonable. Chapter 4 and Chapter 5 explain how to determine the optimal locations for additional measurements.

3.6 Acknowledgement

Ron Weir, David Eaton and Nadine Igonin are specially thanked for the processing and preparation of the data. In addition, Dale Walters from CGG and Mehrdad Soltanzadeh from Canadian Discovery are much appreciated for providing insights about geomechanics.

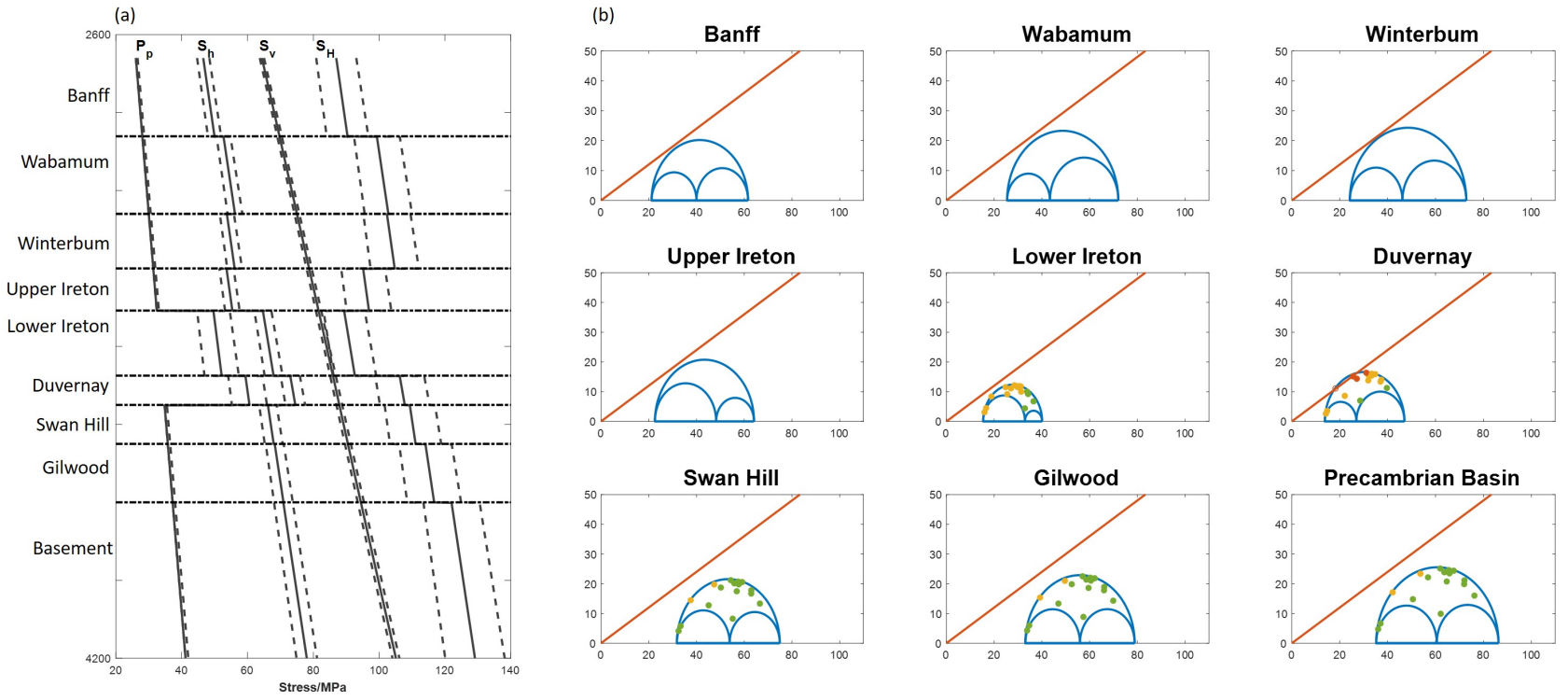

Figure 3.11: Stress gradients and Mohr diagrams of Case 3 where the overpressure exists in the Lower Ireton and the Duvernay. (a). Gradients of principal stresses and pore pressure. p_p, S_h, S_v, and S_H represent the pore pressure, minimum horizontal stress, vertical stress and maximum horizontal stress respectively. Solid lines are the stresses directly calculated based on the rock properties in Figure 3.1(b) and stress measurements at the Duvernay in Table 3.2 using the stress interpretation model by Roche and van der Baan (2017). The dashed lines close to the solid lines indicate the uncertainty given to each stress during the FSP analysis. Horizontal dashed lines are the formation boundaries. (b). Mohr diagrams of the formations using the stresses indicated by the solid lines in (a). Names of the formations are shown above the diagrams. The CFC is the red solid line. At formations with faults crossing, the stress state at each fault plane is calculated and shown as dots in the Mohr diagram. The color of the dot is based on the distance between the dot and the line of CFC.

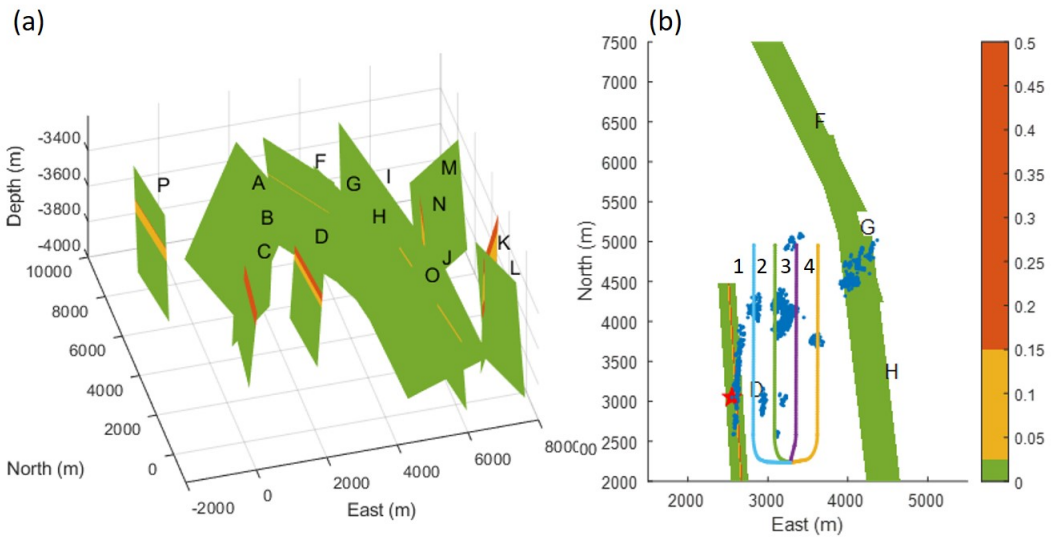

Figure 3.12: Updated FSP analysis and comparison with the observed AIS. (a). FSP of all faults in Case 3. Fault planes are colored based on the FSP in each formation. The color bar on the right shows how the FSP is colored. (b). Comparison between the FSP results in Case 1 and the AIS during the treatment. The figure is in a map view. Four horizontal wells are named 1-4. Blue dots are the observed AIS. Red star is the location of the maximum AIS with M_w 3.2.

Chapter 4

Kriging and sampling criteria

Summary

In this chapter, the theory of kriging is explained, followed by the introductions of two sampling criteria for determining the optimal locations for additional samples. One criterion is based on the error variance given by kriging. The additional sampling takes place at where the error variances are the largest. The second criterion is modified from the Warrick-Myers sampling criterion. This criterion aims to increase the robustness of the variogram model estimation.

4.1 Introduction

In situ stress measurements are considered as one of the essential types of information in the risk assessment of AIS. By understanding the stress state of a region, analysts can assess which areas and faults are under a critical stress state. Measurements of in situ stress states are limited to the locations of wells, making the quantification of regional in situ stress one of the main sources of uncertainty in the risk assessment. Improving the strength of the knowledge used in the risk assessment is beneficial. For areas with few stress measurements, interpolation becomes important because it shows how the stress changes within the area. In this thesis, kriging is adopted as the main interpolation approach of in situ stress. Kriging is a common interpolation method in geostatistics.

Kriging assumes the variable is first- and second-order stationarities, in which the mean and the variance of the variable are constant through the whole area.

Kriging estimates how the in situ stress changes within the area of interest. If there are more wells available for stress measurements, the interpolation is updated with more samples. Given the fact that the in situ stress measurements are both time-consuming and expensive, choosing the optimal wells for additional sampling becomes crucial. On the other hand, sampling locations are constrained by the locations of wells, which means that the wells might not be located in the most desirable areas for improving interpolation. Therefore, the objective is to determine the optimal sampling locations that can improve the performance of kriging the most within the spatial limitation of well locations. For convenience, the sampling process is divided into two phases, where the first-phase samples refer to the original samples and the second-phase samples refer to the additional samples. The second-phase sampling design is the focus of this thesis. Two second-phase sampling criteria are proposed, namely the modified Warrick-Myers sampling criterion and the error-variance sampling criterion. The detailed explanations of the criteria are in the following sections after the explanation of kriging.

4.2 Methodology

4.2.1 Variogram

The following explanations are based on Pyrcz and Deutsch (2014). For a random variable Z in an area $\mathbf{U}$ (Figure 4.1(a)), suppose $Z(\mathbf{u}_i)$ indicates the spatial variability of Z with the location $\mathbf{u}_i$, where $\mathbf{u} = (u_{xi}, u_{yi})$ and $\mathbf{u} \in \mathbf{U}$. Define the mean and the variance of Z are m and σ^2. Assume Z is a function of the location $\mathbf{u}$, the variogram is defined as the variance of Z at two different locations, $\mathbf{u}_i$ and $\mathbf{u}_j$,

$$2\gamma(h) = E\{[Z(\mathbf{u}_i) - Z(\mathbf{u}_j)]^2\}, \tag{4.1}$$

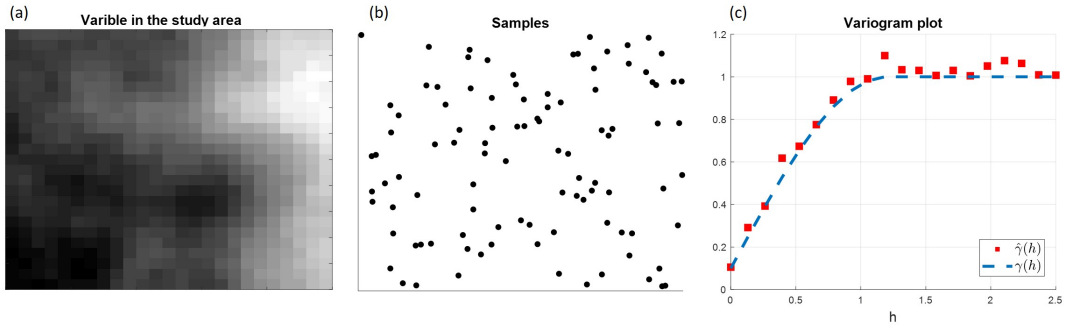

Figure 4.1: Example of calculating experimental variograms. (a). Map of the variable (Z) in the study area. (b). 100 samples of the variable. (c). Calculated experimental variograms $\hat{\gamma}(h)$ (red squares) and variogram model $\gamma(h)$ (dashed line) created based on $\hat{\gamma}(h)$.

where h denotes the distance vector between the two locations as $h = ||\mathbf{u}_i - \mathbf{u}_j||$. h is also known as the lag. The semi-variogram is $\gamma(h)$ and in this thesis, variogram refers to semi-variogram for convenience.

Within the area of interest with k samples (Figure 4.1(b)), denote the set of samples that have the distance of h_l as L. The variogram $\hat{\gamma}(h_l)$ is

$$\hat{\gamma}(h_l) = \frac{1}{2N_l} \sum [Z(\mathbf{u}_i) - Z(\mathbf{u}_j)]^2 (i, j \in L), \tag{4.2}$$

where N_l is the number of all the combinations of elements in set L. In the same area, we can calculate the variogram between any two samples and plot it in a figure with the lag distance as the x-axis and the variogram as the y-axis (Figure 4.1(c)). The calculated variograms are denoted as $\hat{\gamma}(h_e)$ and called the experimental variograms. The variogram represents the variance of samples with a certain distance, and is negatively related to the spatial correlation of the samples. In general, with the increase of the lag, the variogram becomes larger as the samples become less correlated as the distance between them increases spatially. The lag continues increasing to a value called the effective range. For any lag that is greater than the effective range, samples are not spatially correlated. The maximum of the variogram is called the sill, which equals the variance of the random variable Z, σ^2. In contrast, with the lag decreasing, the variogram becomes smaller as the samples become more spatially correlated. Ideally, the variogram reduces to zero when the lag is zero because the samples

at the same location should be identical. However, the variogram does not become zero at lag zero due to the measurement errors of the samples. The non-zero variogram when the lag is zero is called the nugget. The nugget represents the measurement errors.

Once all the experimental variograms $\hat{\gamma}(h_e)$ are calculated, a variogram model $\gamma(h)$ is created by fitting the experimental variograms with a function, as the blue dashed line shown in Figure 4.1(c). With the variogram model, the spatial correlation of all the locations in the area of interest, including sampled and unsampled ones, are estimated.

Another parameter to describe the spatial relations between samples is the covariance. It is defined as

$$Cov(Z(\mathbf{u}_i), Z(\mathbf{u}_j)) = E\{[Z(\mathbf{u}_i) - m][Z(\mathbf{u}_i) - m]\}(\mathbf{u}_i, \mathbf{u}_j \in \mathbf{U}), \tag{4.3}$$

where Cov is short for covariance.

From Equation 4.1 and Equation 4.3 we have

$$\gamma(h) = \sigma^2 - Cov(h), \tag{4.4}$$

where σ^2 is the variance of Z. h is the vector containing all possible distances between locations in $\mathbf{U}$. Please see Appendix B for proof.

To describe a variogram, three parameters are used, the sill σ^2, the range η and the nugget τ^2. Because sill also refers to the variance of the variable, the same notation σ^2 is used to represent both sill in a variogram model and the variance of the variable. Because the covariance and variogram are interchangeable, the parameters are also used to describe the covariance. Table 4.1 lists three common variogram and covariance models, the Matern 3/2, exponential and Gaussian models. Figure 4.2 show the corresponding plots of the variogram models on the left diagram and the corresponding plots of covariance models on the right diagram. Note in Figure 4.2, the variogram models do no reach the sill at the range, this is because the range given by the variogram model is different than the effective range where the samples are no longer correlated (Mälicke et al., 2018).

Table 4.1: Common variogram and covariance models. τ^2 is the nugget effect, σ^2 is the sill and η is the range.

Model	Variogram ($\gamma(h)$)	Covariance ($Cov(h)$)
Matern 3/2	$\tau^2+(\sigma^2-\tau^2)(1-(1+3h/\eta)e^{-3h/\eta})$	$(\sigma^2-\tau^2)(1+3h/\eta)e^{-3h/\eta})$
Expon-ential	$\tau^2+(\sigma^2-\tau^2)(1-e^{-3h/\eta})$	$(\sigma^2-\tau^2)e^{-3h/\eta}$
Gaussian	$\tau^2+(\sigma^2-\tau^2)(1-e^{-h^2/\eta^2})$	$(\sigma^2-\tau^2)e^{-h^2/\eta^2}$

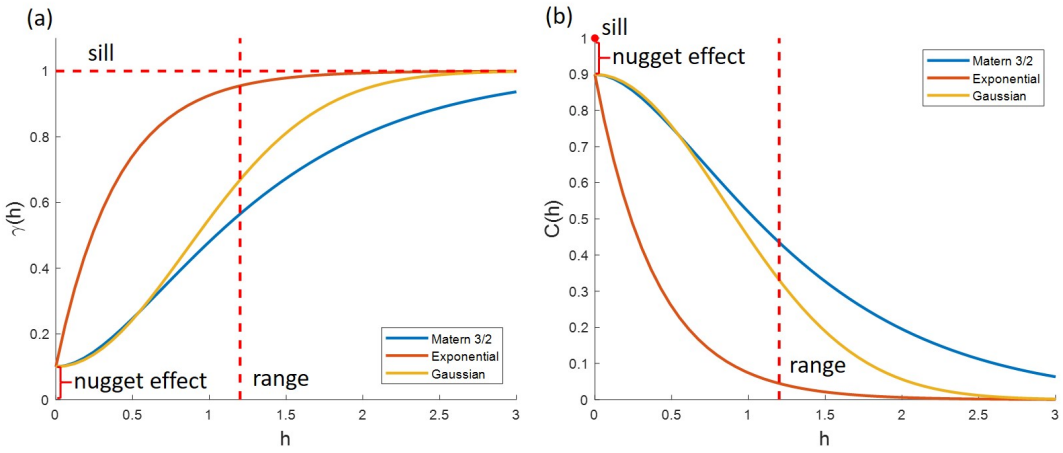

Figure 4.2: (a). Variogram models. (b). Covariance models. In all three models, the sill $\sigma^2 = 1$, the range $\eta = 1.2$, and the nugget effect $\tau^2 = 0.1$.

Declustering

Before kriging, it is important to define a grid in the study area. The samples are declustered based on the grid. Only one datum can represent one grid. If multiple samples are in the same grid, the value of that grid is the average of all samples in that grid as,

$$\bar{z} = \frac{1}{n}\sum_{i=1}^{n} z_i, \tag{4.5}$$

where z_i represents one sample in the grid, n is the total number of samples in the grid, and $\bar{z}$ is the average of all values in the grid. Declustering reduces the data redundancy, if two samples that are very close to each other are treated individually, this could affect the accuracy of the final results (Pyrcz

and Deutsch, 2014). If there are in total U grids, we have

$$U = k + u, \tag{4.6}$$

where k and u are the numbers of samples after declustering and unsampled locations.

4.2.2 Kriging

The first proposal of kriging was by Krige in the 1950s (Krige, 1951). Cressie (1990) examines the development of kriging. The advantage of kriging is that it considers the spatial variance in the samples. Thus it is useful to study the spatial distribution of the variable. The following explanation about kriging is adopted from Pyrcz and Deutsch (2014) and Davis (2002).

Following the notations in Equation 4.6, use $\mathbf{U}$ to denote all the locations in the area of interest. There are k locations that are sampled and u locations that are not sampled. For the unsampled locations, the values of those locations are estimated using kriging. Assume one of the unsampled locations is $\mathbf{u}_0$, the value at this location is $Z(\mathbf{u}_0)$. By the definition of simple kriging, $Z(\mathbf{u}_0)$ is calculated as

$$\hat{Z}(\mathbf{u}_0) = m + \sum_{i=1}^{k} \lambda_i [Z(\mathbf{u}_i) - m], \tag{4.7}$$

where m is the mean of the variable Z and λ_i is the weight of the value at the ith sampled location. Kriging is based on least square optimization. The idea is to minimize the squared error between the estimated result and the true value. To get the least estimation error, the weights in Equation 4.7 are calculated using the covariances between the sampled locations and the unsampled location $\mathbf{u}_0$. Define

$$\mathbf{\Lambda} = \begin{bmatrix} \lambda_1 \\ \lambda_2 \\ \vdots \\ \lambda_k \end{bmatrix}, \tag{4.8}$$

$$\mathbf{C}_s = \begin{bmatrix} Cov(\mathbf{u}_1, \mathbf{u}_1) & Cov(\mathbf{u}_1, \mathbf{u}_2) & \dots & Cov(\mathbf{u}_1, \mathbf{u}_k) \\ Cov(\mathbf{u}_2, \mathbf{u}_1) & Cov(\mathbf{u}_2, \mathbf{u}_2) & \dots & Cov(\mathbf{u}_2, \mathbf{u}_k) \\ \vdots & \vdots & \ddots & \vdots \\ Cov(\mathbf{u}_k, \mathbf{u}_1) & Cov(\mathbf{u}_k, \mathbf{u}_2) & \dots & Cov(\mathbf{u}_k, \mathbf{u}_k) \end{bmatrix}, \tag{4.9}$$

and

$$\mathbf{M} = \begin{bmatrix} Cov(\mathbf{u}_1, \mathbf{u}_0) \\ Cov(\mathbf{u}_2, \mathbf{u}_0) \\ \vdots \\ Cov(\mathbf{u}_k, \mathbf{u}_0) \end{bmatrix}. \tag{4.10}$$

Then we have

$$\mathbf{\Lambda} = \mathbf{C}_s^{-1}\mathbf{M}. \tag{4.11}$$

If

$$\mathbf{Y} = \begin{bmatrix} Z(\mathbf{u}_1) - m \\ Z(\mathbf{u}_2) - m \\ \vdots \\ Z(\mathbf{u}_k) - m \end{bmatrix}, \tag{4.12}$$

then the estimated value $\hat{Z}(\mathbf{u}_0)$ equals

$$\hat{Z}(\mathbf{u}_0) = m + \mathbf{Y}^T\mathbf{\Lambda} = m + \mathbf{Y}^T\mathbf{C}_s^{-1}\mathbf{M}. \tag{4.13}$$

The detailed explanation of simple kriging can be found in Davis (2002) and Pyrcz and Deutsch (2014).

4.3 Error-variance based sampling criterion

In this section, the sampling criterion based on the kriging error variance is explained. The idea is straightforward. The additional samples should be located at where the error variances are the greatest.

The error variance of the estimated value $\sigma_E^2(\mathbf{u}_0)$ is

$$\sigma_E^2(\mathbf{u}_0) = \sigma^2 + \sum_{i=1}^{k}\sum_{j=1}^{k}\lambda_i\lambda_j Cov(\mathbf{u}_i, \mathbf{u}_j) - \sum_{i=1}^{k}\lambda_i Cov(\mathbf{u}_i, \mathbf{u}_0). \tag{4.14}$$

The three parts in Equation 4.14 represent three types of variances that contribute to $\sigma_E^2(\mathbf{u}_0)$. According to Pyrcz and Deutsch (2014), the three parts are

1. $\sum_{i=1}^{k}\sum_{j=1}^{k}\lambda_i\lambda_j Cov(\mathbf{u}_i, \mathbf{u}_j)$. This is called the *redundancy*. It represents the spatial redundancy of the samples. The redundancy increases with the decrease in the distances among samples. If the samples are clustered in a small part of the study area, the error variance could become high as the redundancy in the samples is large.

2. $\sum_{i=1}^{k}\lambda_i Cov(\mathbf{u}_i, \mathbf{u}_0)$. This is called the *closeness*. This closeness is the distance between the samples and unsampled location $\mathbf{u}_0$. The error variance decreases as the samples become closer to $\mathbf{u}_0$.

3. σ^2. This is the variance of the variable in the study area.

With the second-phase samples, both the sample *redundancy* and the *closeness* change, and hence $\sigma_E^2(\mathbf{u}_0)$ changes.

The error-variance based sampling criterion determines the additional sampling locations based on $\sigma_E^2(\mathbf{u}_0)$ at each unsampled location. After declustering, there are in total U locations in the study area. The objective is to reduce $\sum_i^U \sigma_E^2(\mathbf{u}_i)$ as much as possible by the second-phase samples. $\sigma_E^2(\mathbf{u}_i)$ at the ith sampled location is zero. $\sigma_E^2(\mathbf{u}_i)$ at one of the unsampled locations is calculated using Equation 4.14. The change in the error variance, based on Delmelle (2012), is measured as

$$\Delta\sigma_E^2 = \frac{1}{U}(\sum_{i=1}^{U}\sigma_{E1}^2(\mathbf{u}_i) - \sum_{i=1}^{U}\sigma_{E2}^2(\mathbf{u}_i)), \tag{4.15}$$

where footnotes $_1$ and $_2$ represent the error variance before and after the additional samples.

To maximize $\Delta\sigma_E^2$, we need to minimize $\sum_{i=1}^{U} \sigma_{E2}^2(\mathbf{u}_i)$ with additional samples. Because the error variances at the sampled locations are zero, $\sum_{i=1}^{U} \sigma_{E2}^2(\mathbf{u}_i)$ reaches its minimum when the locations with the highest error variances are measured. Therefore, the error-variance based method is to sample at locations where the error variances are the largest.

4.4 Warrick-Myers sampling criterion

In this section, the modified Warrick-Myers sampling criterion that generates a robust variogram model for kriging is explained.

4.4.1 Concept

Proper estimations of the experimental variograms and a good variogram model are important (Armstrong, 1984). In general, a decent construction of the variogram model requires a sufficient number of experimental variograms calculated with existing samples (Davis and Borgman, 1979, 1982; Warrick and Myers, 1987). In other words, the sampling should be designed in a way that the experimental variograms are calculated from as many lags as possible. Figure 4.3 illustrates how the distribution of experimental variograms affects the construction of the variogram model. With samples covering the whole area, various lags can be used to build the variogram model, as shown in Figure 4.3(a) and (c). On the other hand, if samples are clustered in parts of the area, the variability of the lags is limited, as shown in Figure 4.3(b) and (d). In Figure 4.3(d), more uncertainty is created when fitting a variogram model to the experimental variograms. To reduce the uncertainty, a series of properly distributed experimental variograms are better than poorly scattered ones. Therefore, the sampling criterion is designed to improve the variability of lags.

Based on this idea, the Warrick-Myers sampling criterion is adopted. First, optimal numbers of experimental variograms within different lag intervals are assigned. Then the criterion calculates the differences between the number of the experimental variograms in each interval with the assigned optimal number (Warrick and Myers, 1987; Delmelle, 2009; Wang et al., 2012). The sampling

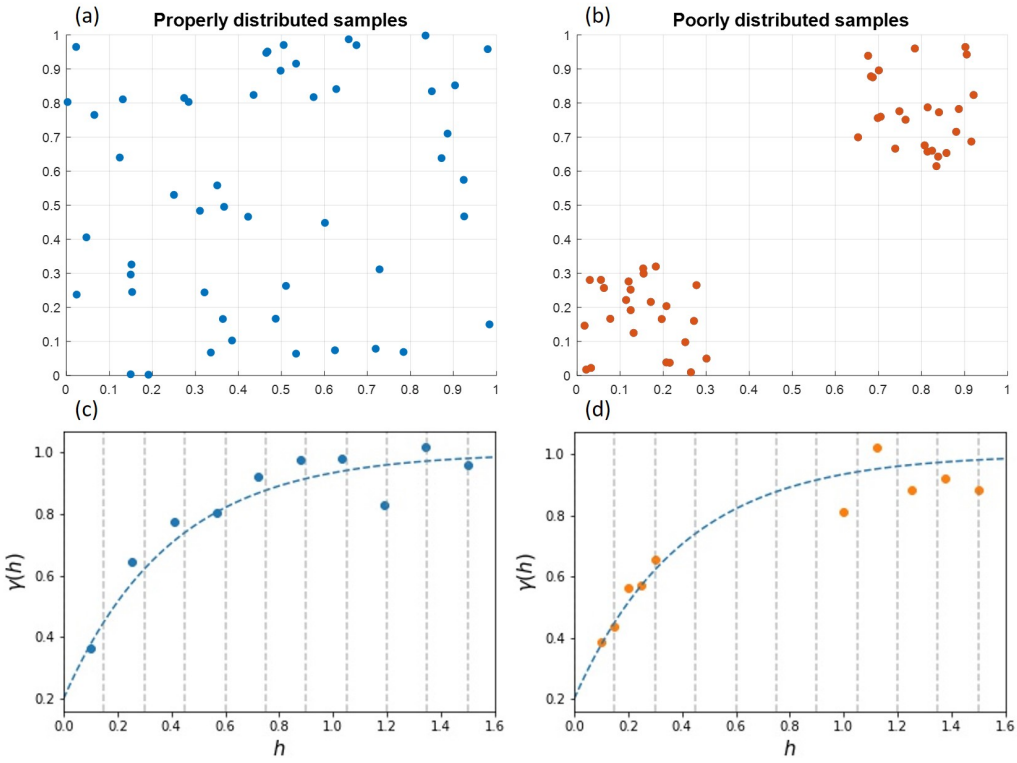

Figure 4.3: Comparison between the variograms from properly distributed samples and poorly distributed samples. There are 50 samples in both cases. (a). Samples cover the whole area; (b). Samples only cover parts of the area; (c). Experimental variograms from samples in (a); (d). Experimental variograms from samples in (b). The dashed line in (c) and (d) indicates one possible variogram model by fitting the experimental variograms.

design is evaluated based on the closeness between the assigned optimal number and the actual number of sample pairs. Because the original criterion focuses on the first-phase sampling, the original evaluation equation is modified to solve the second-phase sampling problem.

4.4.2 Methodology

The Warrick-Myers sampling criterion is explained in the following section with an example. Suppose there are $k = 20$ first-phase samples in a 1×1 square, as shown in Figure 4.4(a). There are in total $\binom{k}{2} = k(k-1)/2 = 190$ pairs of samples. The maximum lag is equally divided into 15 intervals. The experimental variograms are calculated using Equation 4.2. Then within one

lag interval $(h_{i-1}, h_i]$ $(i = 1, 2, ..., 15; h_0 = 0)$, the number of pairs of samples with the lag within that interval is counted. Denoted the number of pairs of samples in the ith interval as N_i^s, as shown in blue bars in Figure 4.4(b). Since the variogram model is based on the experimental variograms, there should be as many pairs of samples as possible in each lag interval. The optimal number of pairs of samples within the interval is assigned as N_i^o, as shown in green bars in Figure 4.4(b). It is obvious that

$$\sum_{i=1}^{15} N_i^s = \sum_{i=1}^{15} N_i^o = \binom{15}{2} = 190. \tag{4.16}$$

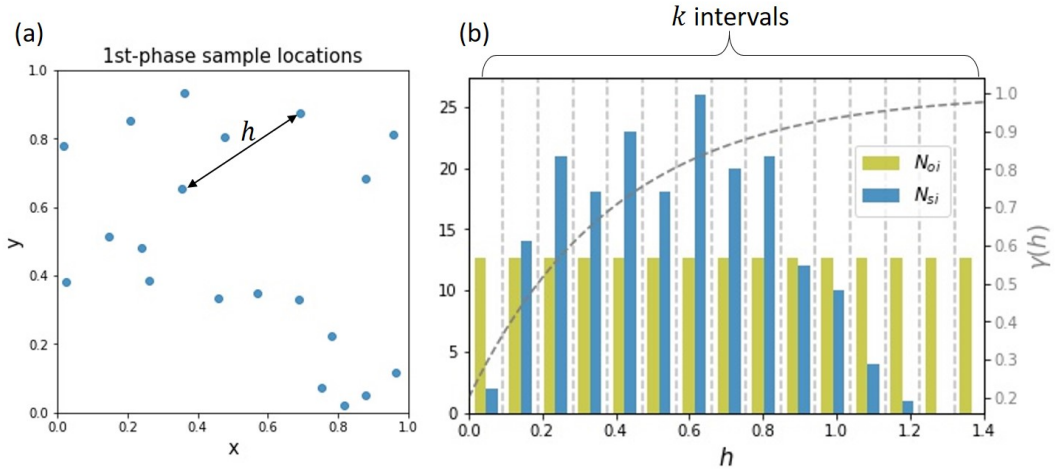

Figure 4.4: Demonstration of N_i^o and N_i^s. (a). 20 first-phase samples in a 1×1 square. Blue dots represent the samples. Samples connected with the black arrow is one pair of samples with lag distance of h. (b). Numbers of pairs of samples within intervals. The lag h is divided into 15 intervals. N_i^s and N_i^o are the actual and the optimal numbers of pairs of samples with lag distances in the ith interval respectively. The dashed gray curve is a possible variogram model. A detailed analysis of this figure is in the context.

From Figure 4.4(b) we can see that most of the experimental variograms of the first-phase samples have intermediate lag distances. N_i^s is greater at intermediate lag intervals comparing to N_i^s at small or large intervals. When fitting the experimental variograms with a variogram model, there is less uncertainty in the middle of the variogram model than that in the beginning or the end of

the variogram model. This is because more experiment variograms, indicated by N_i^s, lead to a more robust estimation of the variogram model. For instance, in Figure 4.4(b), the number of pairs in the first interval N_1^s (the first blue bar) is small, meaning that the estimations of the nugget and of how the variogram model changes at very small lags are poor. Therefore, the idea is to design the sampling locations that makes N_i^s as similar to N_i^o as possible. Based on this, Warrick and Myers (1987) propose a criterion called the *Sum of Squares(SS)*. The SS is defined as

$$SS = s_1 \sum_{i=1}^{15} w_i (N_i^s - N_i^o)^2 + s_2 \sum_{i=1}^{15} m_{1i} + s_3 \sum_{i=1}^{15} m_{2i}, \tag{4.17}$$

where w_i is the weight given to each internal. s_1, s_2 and s_3 are the assigned coefficients. m_{1i} and m_{2i} are two parameters that also characterize the samples but are not our focus. Hence $s_2 = s_3 = 0$. The detailed explanation of these two parameters can be found in the original work by Warrick and Myers (1987). Equation 4.17 focuses on how different first-phase sampling designs affect SS. Since the focus in this study is the second-phase sampling design, Equation 4.17 is modified. If $\mathbf{N}^o = [N_1^o, N_2^o, ..., N_{15}^o]$ and $\mathbf{N}^s = [N_1^s, N_2^s, ..., N_{15}^s]$, we can denote $f(\mathbf{N}^o)$ and $f(\mathbf{N}^s)$ as the discrete pdf's of $\mathbf{N}^o$ and $\mathbf{N}^s$. Based on Equation 4.17, we have

$$f(\mathbf{N}^o) = \frac{\mathbf{N}^o}{k(k-1)/2}, f(\mathbf{N}^s) = \frac{\mathbf{N}^s}{k(k-1)/2}. \tag{4.18}$$

Therefore, the modified criterion evaluates the similarity of $f(\mathbf{N}^o)$ and $f(\mathbf{N}^s)$, which is represented by the Bhattacharyya coefficient. The Bhattacharyya coefficient determines the overlap between two probability distributions (Bhattacharyya, 1943). Define the similarity as R, the modified version of Equation 4.17 is

$$\begin{aligned} R &= \sum_{i}^{k} \sqrt{f(\mathbf{N}^o) f(\mathbf{N}^s)} \\ &= \sum_{i}^{k} \sqrt{\frac{N_i^s N_i^o}{(N(N-1)/2)^2}}. \end{aligned} \tag{4.19}$$

When $f(\mathbf{N}^o) = f(\mathbf{N}^s)$, R reaches its maximum as 1. R represents the robust-

ness of the variogram model built based on the sampling design. With second-phase samples, R changes. Similar to the error-variance based criterion, there are $\binom{n_a}{n_c}$ combinations of additional sample locations with n_a available locations and n_c samples that can be added. Denote the combinations as $\mathbf{a}$, then R becomes a function of $\mathbf{a}$ as $R(\mathbf{a})$. The best alternative a_b satisfies

$$R(a_b) = max(R(\mathbf{a})). \tag{4.20}$$

4.4.3 Demonstration

For example, suppose 3 out of 7 locations can be picked for the second-phase sampling, the 20 first-phase samples (blue dots) and the available locations (pink dots) are shown in Figure 4.5(a). There are in total $\binom{7}{3} = 35$ combinations of locations that can be selected for additional sampling. The combination with the highest R is shown as orange dots in Figure 4.5(b). The longest lag distance is $\sqrt{1^2 + 1^2} = \sqrt{2}$, the lag is divided into 15 intervals, as indicated by the vertical dashed lines in Figure 4.5(c). Assume the optimal distribution of $\mathbf{N_o}$ is uniform, indicating all the 15 lag intervals are equally important, so the pdf of $\mathbf{N}^o$ should be $f(\mathbf{N}^o) = 1/15$, as shown in the green dashed line in Figure 4.5. The corresponding pdf's of $\mathbf{N}^s$ with and without second-phase samples are shown in Figure 4.5(c). From Figure 4.5(c) we can see that by adding three more samples, $f(\mathbf{N}^s)$ becomes more similar to the assigned uniform distribution of $\mathbf{N}^o$, indicating the estimation of the variogram model becomes more robust.

4.5 Conclusion

Interpolation of the in situ stress is vital because it helps to understand how stress changes in the area of interest. The accuracy of the estimation of the in situ stress affects the validity of the risk assessment of AIS. Kriging is applied to interpolate the in situ stress. In this chapter, two second-phase sampling criteria are introduced. They are the modified Warrick-Myers sampling criterion and the error-variance based sampling criterion.

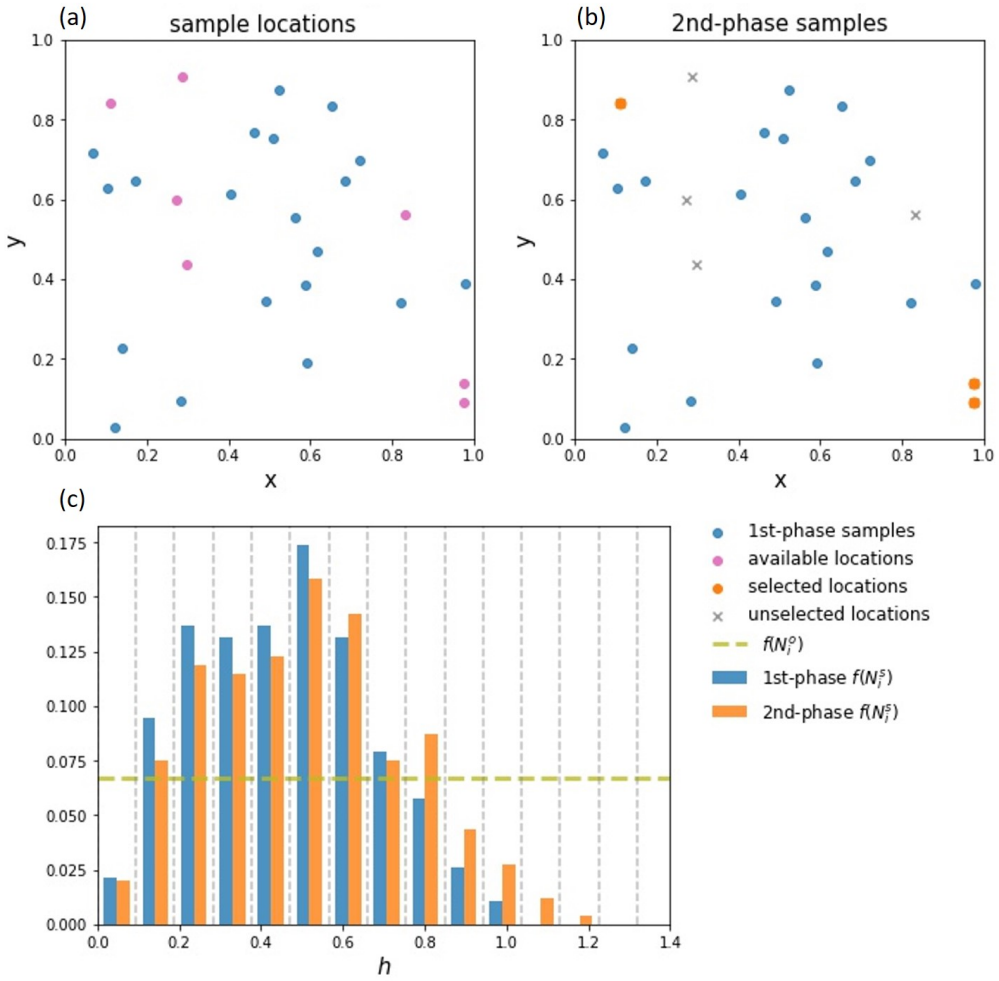

Figure 4.5: (a). 20 first-phase (blue dots) and 7 available sample locations for additional sampling (pink dots). (b). Second-phase samples presented by dots. Additional samples are selected based on the modified Warrick-Myers sampling criterion (orange dots). Unselected locations are shown in cross. (c). Pdf's of $\mathbf{N}^s$ from the first-phase samples in (a) and the first- and second-phase samples in (b). The horizontal dashed line is the assigned $f(\mathbf{N}^o)$. Vertical dashed lines indicate the 15 intervals.

Kriging is based on the spatial relations between the samples, which are represented by a variogram model. Therefore, it is crucial to build a robust variogram model that describes the spatial relations correctly. The Warrick-Myers sampling criterion is aimed at improving the robustness of the variogram model by having ideal pairs of samples in each lag interval. This criterion is modified to apply to the second-phase sampling situation. By adding the second-phase

samples based on this criterion, the robustness of the variogram model is increased. Therefore, the kriging results based on the improved variogram model are improved as well.

The second sampling criterion is the error-variance based criterion. According to the definition of kriging, the error variances of the kriging results are also calculated. The error variances at the sampled locations equal zero. The error-variance based sampling criterion is to add second-phase samples at the locations where the error variances are the greatest. So the sum of all the error variances in the kriging results reaches its minimum by adding the second-phase samples. Hence the kriging results are improved.

Before kriging, samples are declustered to reduce the data redundancy and improve the kriging results. Another step often done before the kriging is called the normal score transformation. It transforms the distribution of the samples into a normal distribution with a mean of zero and variance of one. Since the variance of the samples is also the sill of the variogram, after normal score transformation, the sill of the variogram model is known as one. The detailed explanation of the normal score transformation is in Appendix C.

The trend in the in situ stress should be removed before applying kriging because the trend violates the first- and second-order stationarities that kriging assumes. Another approach to include the trend in the interpolation is to use a spatial regression model with kriging. This method is briefly discussed in Appendix D.

Chapter 5

Determination of the optimal additional sampling locations

Summary

In this chapter, the two sampling criteria, the Warrick-Myers sampling criteria and the error-variance sampling criterion, are compared. As mentioned in Chapter 1, the premise is that the locations available for second-phase samples are pre-determined and only part of these locations can be chosen. Under this premise, synthetic data sets are created to test the effectiveness of the two criteria. The examples show that the second-phase samples given by the error-variance based sampling criterion yield a higher misfit reduction on average. The sensitivity tests also show that the error-variance based sampling criterion is more robust when the data variability, spatial correlation of the variable, the measurement error or the first-phase sampling size changes.

5.1 Introduction

In Chapter 4, two criteria for second-phase sampling are introduced, namely the modified Warrick-Myers sampling criterion and the error-variance based sampling criterion. In this chapter, which criterion is better to determine the optimal second-phase sampling locations is studied. For convenience, the

Warrick-Myers sampling criterion is referred as *WM-sampling* or *WM*, and the error-variance based sampling criterion is referred as *EV-based* or *EV* in the following context.

5.2 Method

To evaluate the effectiveness of the two criteria, the misfit is adopted. It is defined as the sum of the difference between the interpolated result and the real data, that is,

$$\delta_m = \sum_{i}^{U} |\hat{Z}(\mathbf{u}_i) - Z(\mathbf{u}_i)|^2, \tag{5.1}$$

where δ_m denotes the misfit, U is the number of locations after declustering, $\hat{Z}(\mathbf{u}_i)$ and $Z(\mathbf{u}_i)$ are the estimated and true values at the ith location. In general, with more samples, the misfit should be reduced (Sullivan, 2015). In another word, the interpolation results will be closer to the real data as the sample size increases.

5.3 Results

5.3.1 Example 1

To demonstrate how the two criteria are compared, a random data set within a 1×1 square is created. The workflow of this example is shown in Figure 5.1. The real data set $Z(\mathbf{U})$ is created based on a given variogram model. The variogram model of choice is the Matern 3/2 variogram model. Denote $\boldsymbol{\theta}$ as the variogram parameter vector, and $\boldsymbol{\theta} = (\sigma^2, \eta, \tau^2)$. The values of the three parameters are listed in Table 5.1. Note here the true data set should not contain the measurement error. Hence the nugget effect is zero. The real data set is shown in Figure 5.2(a). Then 25 samples are randomly picked from $Z(\mathbf{U})$ as the first-phase samples. The 25 samples with no measurement error are shown in Figure 5.2(b). Based on the first-phase samples, simple kriging is applied. The variogram model parameters are estimated using the maximum

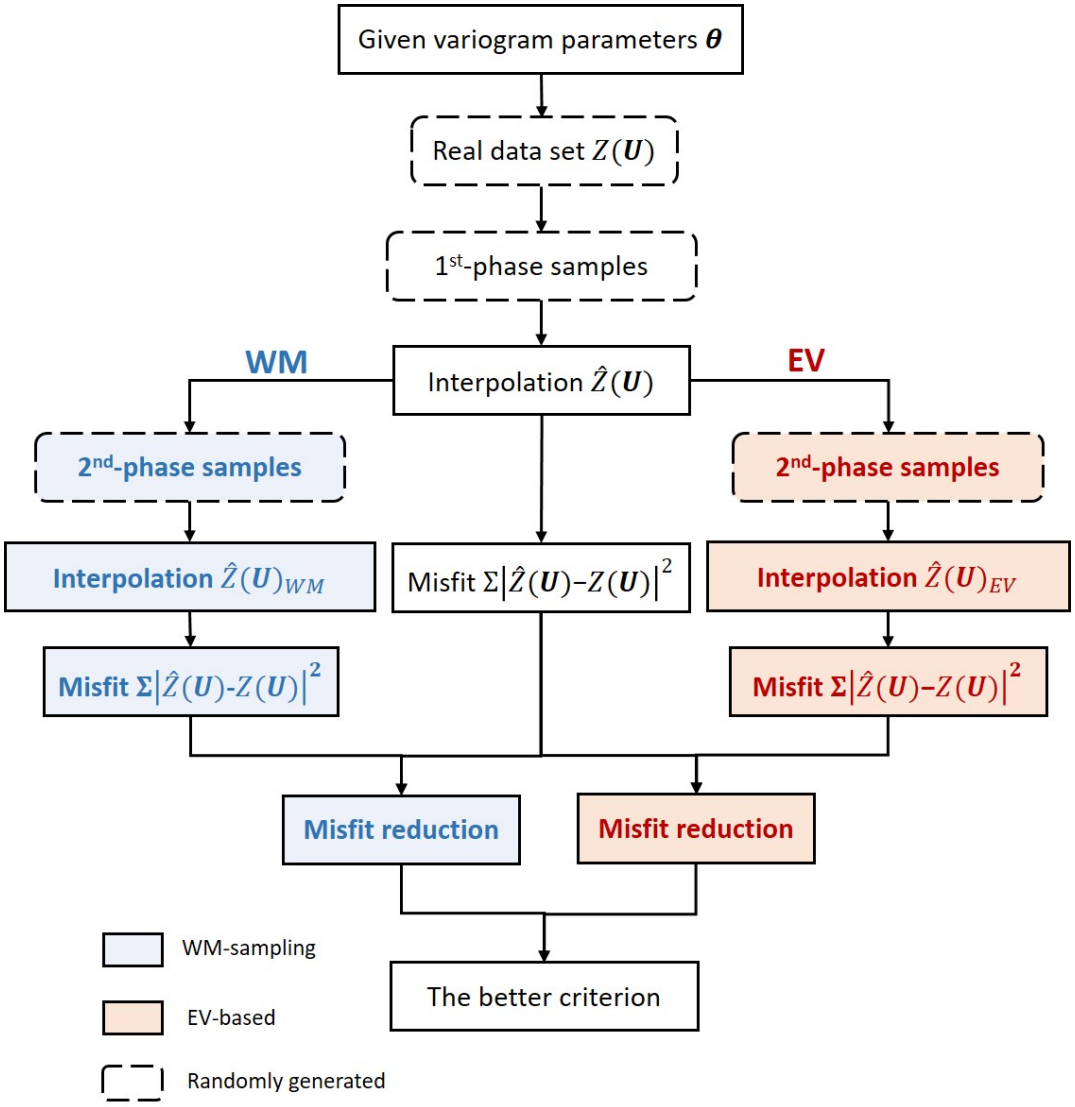

Figure 5.1: Workflow of Example 1. $\boldsymbol{\theta}$ is vector with variogram model parameters ($\boldsymbol{\theta} = (\sigma^2, \eta, \tau^2)$). Steps with dashed boxes are indicating the data are randomly generated based on the data from the above step. Data within the solid boxes are directly calculated. *WM* and *EV* are short for Warrick-Myers sampling and error-variance based sampling criteria. More detailed explanation of the workflow is in the context.

likelihood. The kriging result $\hat{Z}(\mathbf{U})$ and the error variance $\hat{\boldsymbol{\sigma}}_E^2$ from kriging are shown in Figure 5.3. Using Equation 5.1, the misfit is 13.80.

Table 5.1: Parameters used to create the true data set.

σ	η	τ^2
0.5	0.33	0

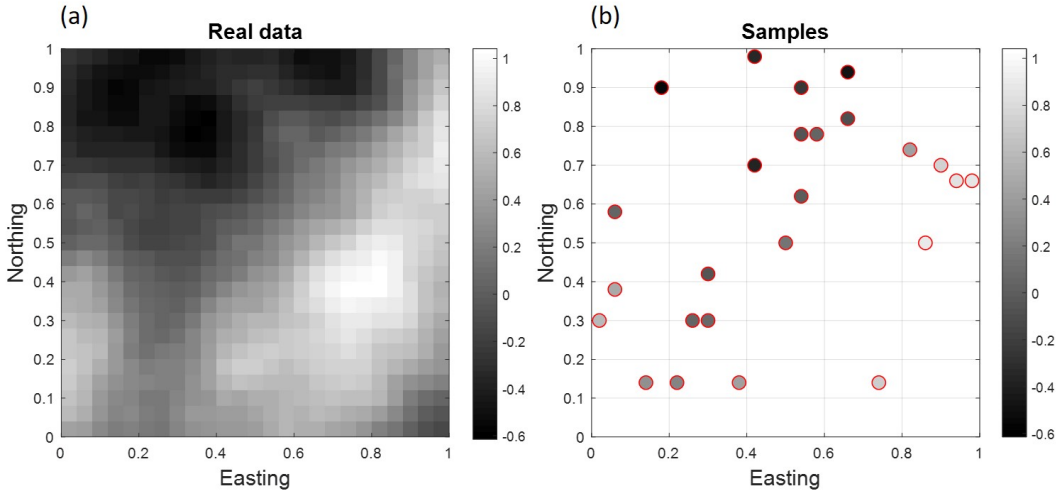

Figure 5.2: (a). Data created based on the parameters given in Table 5.1. (b). 25 samples randomly picked from the data set in (a).

Table 5.2: Misfit reductions using *WM-sampling* and *EV-based* criteria for second-phase sampling design. Misfit is calculated using Equation 5.1. The kriging results are based on the original 25 samples with the 3 additional samples given by *WM-sampling* and *EV-based* criteria in Figure 5.4(b) and (c).

Criteria	Misfit reduction
WM	3.83
EV	1.10

Then 7 sample locations are randomly generated as the available second-phase sampling locations, as shown in Figure 5.4(a). Assume 3 out of the 7 samples can be chosen for measurement. Using the *WM-sampling* and the *EV-based* criteria that are explained in section 4.3 and section 4.4, the 3 additional sampling locations are shown in Figure 5.4(b) and (c) respectively. Here we can see the optimal additional sampling locations given by the two criteria differ.

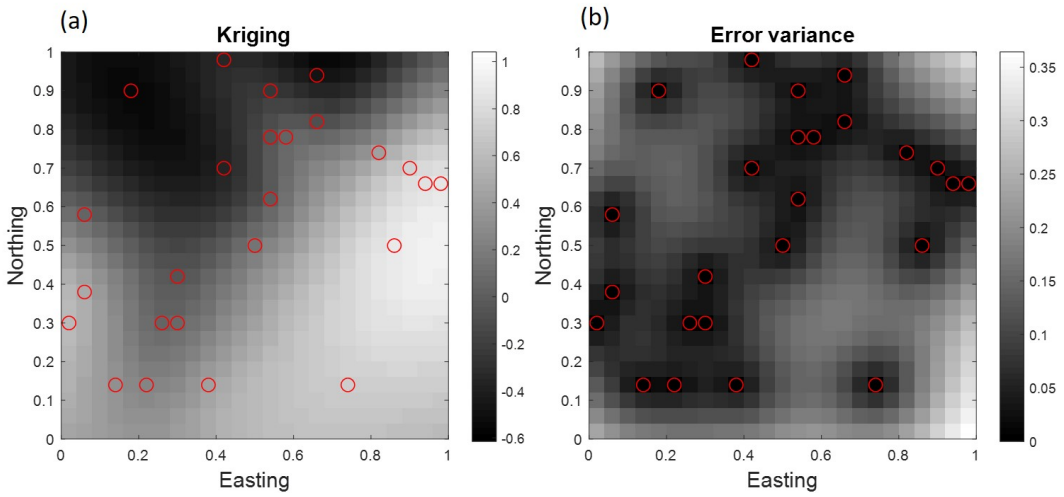

Figure 5.3: (a). Interpolation result using simple kriging with samples in Figure 5.2(b). (b). Error variance of the interpolation result. The error variance reaches zero at the sampled locations. Red circles in both figures are the sample locations.

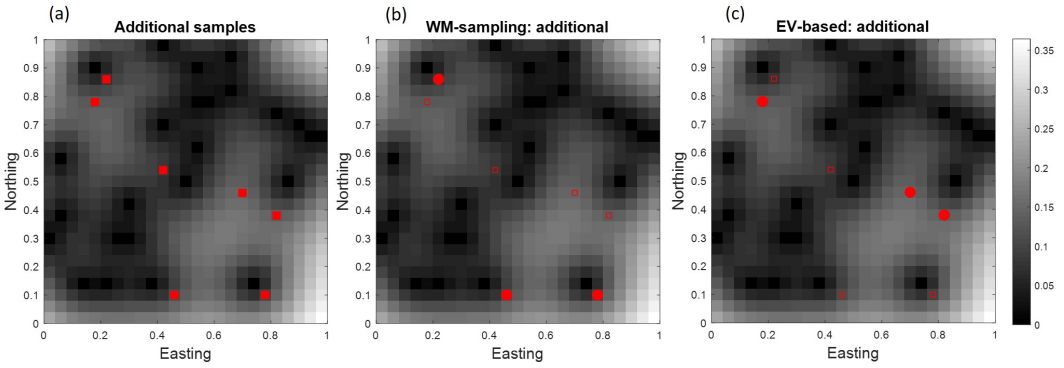

Figure 5.4: (a). 7 additional sampling locations represent by red squares. Samples are randomly picked. (b). 3 optimal sampling locations given by the *WM-sampling* criterion. **WM-sampling** is short for Warrick-Myers sampling. (c). 3 optimal sampling locations given by the *EV-based* criterion. **EV-based** is short for error-variance based sampling criterion. In (b) and (c), hollow squares are the additional sampling locations that are not picked by the criterion, and red dots represent the picked locations.

Figure 5.5(a) shows how the pdf's of $\mathbf{N}^s$ change with the additional samples from the two criteria comparing with that the first-phase samples. The maximum lag is $\sqrt{2}$. The lag is divided into 20 intervals. Here the optimal pdf of the number of pairs ,$f(\mathbf{N}^o)$, is a uniform distribution. With the additional samples, $f(\mathbf{N}^s)$ becomes more similar to a uniform distribution. Figure 5.5(b)

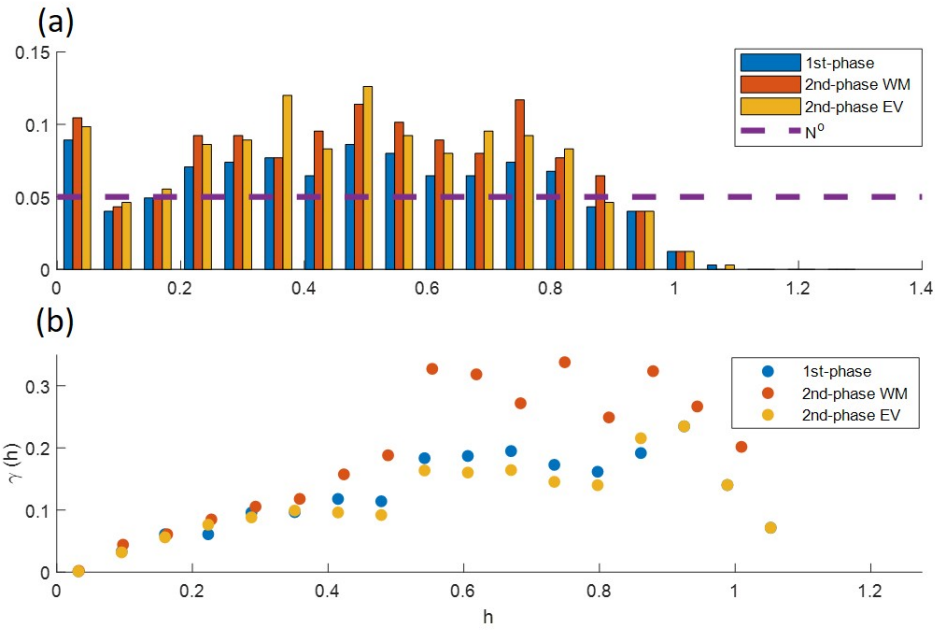

Figure 5.5: (a). Pdf's of the number of pairs of samples ($f(\mathbf{N}^s)$, please see Chapter 4 for detailed explanations). The horizontal line is the pdf of the optimal number of pairs of samples ($f(\mathbf{N}^o)$). (b). Experimental variograms. *1st-phase* indicates samples from the first-phase sampling. *2nd-phase* indicates the experimental variograms calculated after second-phase sampling. *WM* and *EV* mean the criterion used for picking the second-phase samples.

shows the experimental variograms with the first-phase samples and the second-phase samples given by two criteria. Note the experimental variograms with the smallest lag are not zero but very close to zero. This is consistent with the premise that the nugget is zero in Table 5.1. By fitting the experimental variograms with a Matern 3/2 variogram model, the sill, range and the nugget are known. Comparing the estimated variogram model parameters with the true values in Table 5.1, we can see that the experimental variograms calculated from the samples given by *WM-sampling* have a sill that is closer to the real sill. This indicates that the estimated variogram model based on them would describe the true data set the best.

With the 3 additional samples given by both criteria, simple kriging is reconducted and the interpolation results, $\hat{Z}(\mathbf{U})_{WM}$ and $\hat{Z}(\mathbf{U})_{EV}$, as well as the error variances are shown in Figure 5.6. Misfits between the updated kriging results and the real data are calculated again using Equation 5.1. With more

samples, the misfits becomes smaller. The misfit reductions using the second-phase samples given by the two criteria are listed in Table 5.2. In this example, *WM-sampling* results in a greater misfit reduction than *EV-based* does. Therefore, the *WM-sampling* is the better criterion for second-phasing sampling in this example.

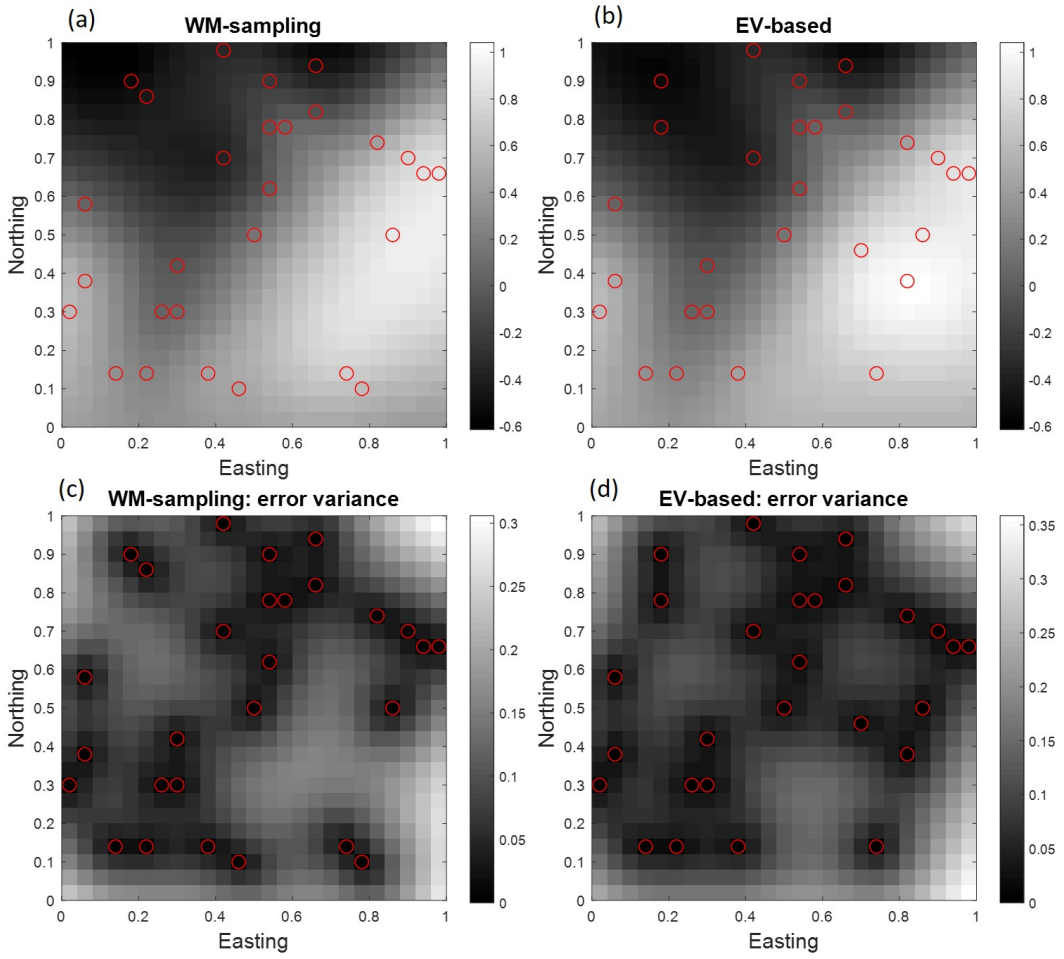

Figure 5.6: Interpolation results and error variances calculated with the first-phase and the 3 additional samples given by the two criteria. Sample locations are shown in red circles. (a) and (c). Samples are the same samples shown in Figure 5.4(b). The second-phase samples are given based on the *WM-sampling*. (b) and (d). Samples are the same samples shown in Figure 5.4(c). The second-phase samples are given based on the *EV-based*.

5.3.2 Example 2

To assure that the conclusion in *Example 1* is not affected by the randomness of the true data set and the sample locations, the same process is repeated multiple times. Since both the real data set and the sampling locations are randomly generated, the simulations are repeated by only randomly generating one of them while fixing the other. The average misfit reductions from the simulations are listed in Table 5.3. From Table 5.3 we can see that in average, EV results in a greater misfit reduction than WM does. Therefore, *EV-based* sampling criterion is a better criterion for determining the optimal additional sampling locations.

Table 5.3: The averaged misfit reduction from simulations. Numbers in the parenthesis are standard deviations. Criterion in bold means the better criterion.

Randomly generated	Criterion	Misfit reduction
Sampling locations	WM	8.59(2.79)
	EV	12.3(2.71)
Real data set	WM	5.39(1.60)
	EV	8.33(2.55)

5.4 Sensitivity tests

Next a series of sensitivity tests are conducted to determine which criterion is more robust. The parameters included in the sensitivity tests are the first-phase sampling size, the sill, the range and the nugget. When changing the sampling size, the real data set ,$Z(\mathbf{U})$ is fixed and the same as shown in Figure 5.2(a). When changing one of the kriging parameters, the sampling locations are fixed, and $Z(\mathbf{U})$ is randomly generated based on the given parameters of the variogram model during each simulation. Except for the variogram parameter that is varied during the sensitivity tests, the remaining parameters stay unchanged as shown in Table 5.1. For the second-phase sampling, it remains as picking 3 out of 7 locations. And the 7 locations are fixed in all sensitivity tests. Both the first-phase and additional sampling locations are the same as shown in Figure 5.2(b) and Figure 5.4(a).

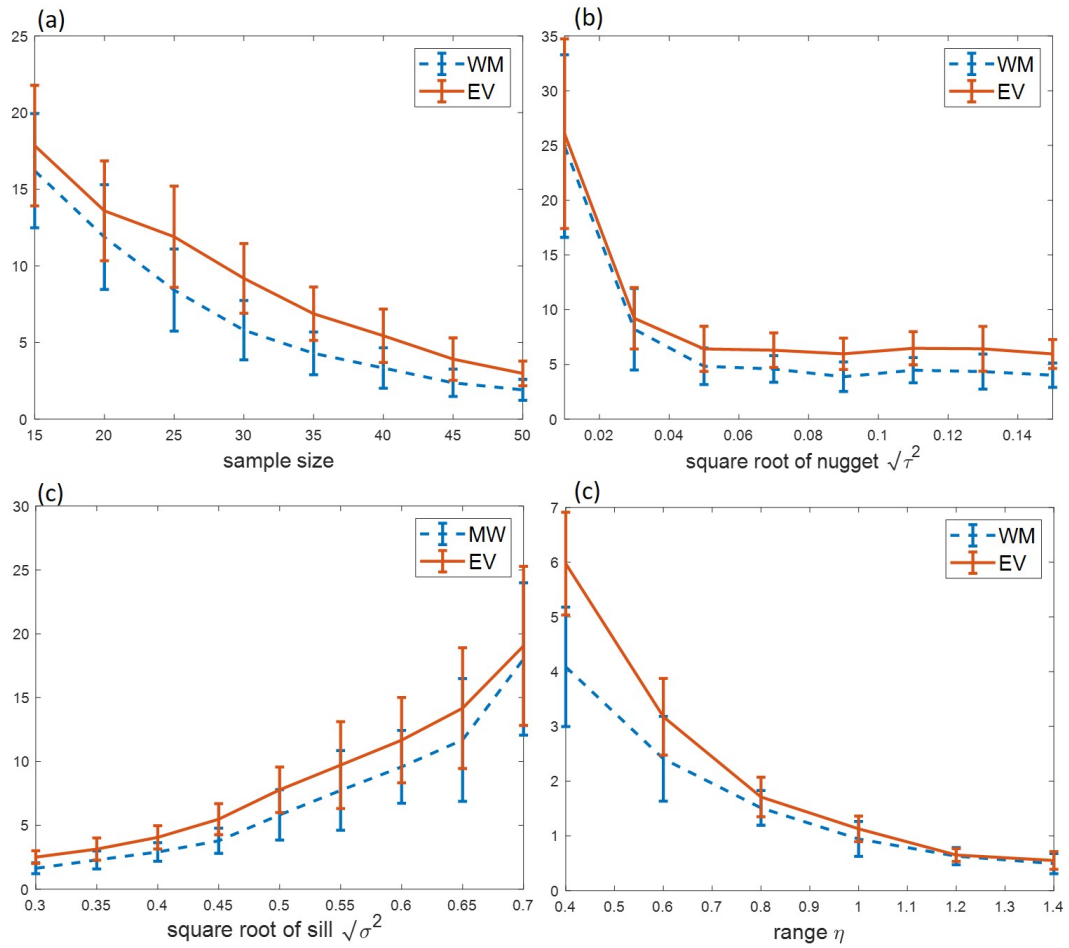

Figure 5.7: Sensitivity tests of the misfit reduction. The y-axis in each plot is the misfit reduction. The error bars are based on the standard deviations of the misfit reductions from the simulations. (a). Sensitivity test of the sample size. (b). Sensitivity test of the nugget τ^2. Here the $x-$axis is the square root of the nugget. (c). Sensitivity test of the sill σ^2. Here the x-axis is the square root of the sill. (d). Sensitivity test of the range η.

From Figure 5.7 we can see that the misfit reduction is sensitive to all the parameters. Nevertheless, in all sensitivity test, EV always has a higher misfit reduction than WM does, indicating EV is the more robust criterion.

When increasing the first-phase sample size from 15 to 50, the means and the variances of the misfit decrease because the performance of the first-phase kriging improves as there are more samples to begin with (Figure 5.7(a)).

The measurement error (the nugget) affects the accuracy of the kriging results. As the nugget τ^2 increases, the misfit reduction decreases because the

error with the additional samples also add uncertainty in $\hat{Z}(\mathbf{U})$. The variances of the misfit reductions decrease significantly at the beginning of Figure 5.7(b). This indicates that when the measurement error is small, the greater source of uncertainty in the misfit reduction comes from the variance of the true data set $Z(\mathbf{U})$. As τ^2 increases, the impact of the randomness in $Z(\mathbf{U})$ on the variances of the misfit reduction reduces. In addition, with larger measurement errors ($\tau > 0.06$), the misfit reductions and their variances do not change significantly. This could indicate that with the increase in the measurement error, the misfit reduction is mainly affected by the measurement error.

The sill represents the variability of the $Z(\mathbf{U})$ itself. As the variance in $Z(\mathbf{U})$ increases, the misfit reductions increases, as shown in Figure 5.7(c). Because with more variability of $Z(\mathbf{U})$, the additional samples become more influential for improving the performance of kriging. The variances of the misfit reduction also increase due to the increase of the variability.

The range indicates the maximum distance between samples that have a spatial correlation. The increase in the range means that more samples in the area are related. The additional samples become less influential on the misfit reduction as the first-phase samples are sufficient for the estimation of the variogram model and the spatial relations of samples in the whole area. The same reason is applicable to the reduction of the variances in the misfit reduction. Figure 5.7(d) also shows that EV is more effective than WM when the range η is small.

5.5 Discussion

By comparing the averaged misfit reductions in different simulations, the criterion that provides the better second-phase sampling locations is *EV-based* sampling criterion. Though in *Example 1*, the second-phase samples given by *WM-sampling* has a higher misfit reduction, the averaged results in *Example 2* show that *EV-based* is the better criterion for determining the second-phase sampling locations.

The misfit between the interpolation results and the real data set is influenced by the first-phase sample size and the spatial relation between the

samples, as shown in the sensitivity tests. The misfit reduction decreases with the increase in the first-phase samples. The size of the first-phase samples determines the value of the second-phase samples. If there is a large size of first-phase samples, adding several second-phase sample might not affect the interpolation results significantly. Hence the misfit reduction reduces as the size of the first-phase samples increases. The misfit increases with the increase of the sill of the real data set and the measurement error, and decreases with the increase of the range of the real data set.

The sill and the measurement error represent two sources of the uncertainty, the *parametric variability* and the *experimental uncertainty*. Increasing either of them would results in the increase in the uncertainty in the interpolation results. The range indicates the spatial correlation of the samples. A larger range means the samples are more correlated within a certain radius, hence decreasing the misfit.

The sensitivity tests show that on average, using the *EV-based* criterion has a higher misfit reduction when changing the variogram parameters. This proves that the *EV-based* criterion is more robust. Therefore, *EV-based* criterion is a better and more robust criterion than *WM-sampling* criterion.

Because the two sampling criteria aim at reducing different sources of uncertainty during interpolation, it is worth discussing the sources of uncertainty that affect the interpolation. Uncertainty can be divided into six groups, namely *parameter uncertainty, parametric variability, model inadequacy, algorithmic uncertainty, measurement uncertainty,* and *interpolation uncertainty* (Kennedy and O'Hagan, 2001). For interpolating spatial samples, such as the stress measurements, with kriging, the six sources of uncertainty can be interpreted as follows.

1. *Parameter uncertainty* comes from the estimated variogram model parameters.

2. *Parametric variability* comes from the variability of the variable. For stress measurements, this is the spatial variance of the stress.

3. *Model inadequacy* refers to the limitation of variogram modeling. Kriging is based on the given variogram model. However, it is difficult to prove

that the variogram model is able to correctly describe the spatial correlation of the samples. The choice of the variogram model also contributes to this type of uncertainty. There are multiple variogram models, such as the Gaussian model. Table 4.1 lists three common variogram models. More variogram models can be found in Pyrcz and Deutsch (2014). If the model is chosen incorrectly, the interpolation results would be incorrect.

4. *Algorithmic uncertainty* comes from the limitation of kriging. Kriging assumes the samples obey the first- and second-order stationarities. At the same time, this assumption could be faulty and create uncertainty. If there is a trend in the data, the assumption does not hold true any more. In this case, the trend should be removed before performing kriging. However, identifying and removing the trend correctly are difficult.

5. *Experimental uncertainty* means the measurement error.

6. *Interpolation uncertainty* is the error variance given by kriging. Since there are limited samples, interpolation and extrapolation are conducted during kriging, which brings uncertainty.

Here we can see that the *WM-sampling* criterion focuses on reducing the *parameter uncertainty* while *EV-based* criterion tackles the *interpolation uncertainty*. The six sources are listed, yet which sources contribute more on the ultimate uncertainty that leads to the misfit has not been studied in this thesis. Nevertheless, because the *EV-based* criterion is more robust, it is possible that for kriging, the interpolation uncertainty has a greater impact. Another possible explanation is that while the *EV-based* criterion focuses on reducing the *interpolation uncertainty*, it also reduces other sources of uncertainty, including the *parameter uncertainty* and *parametric variability*.

On the other hand, since the comparisons are made with multiple simulations and the conclusions are made based on the averaged simulated results. It is possible that there are times when the *WM-sampling* criterion outperforms the *EV-based* criterion.

5.6 Conclusion

In this chapter, the effectiveness and the robustness of both the *WM-sampling* and the *EV-based* criteria are tested. From the simulation results we can see that both criteria are able to achieve a misfit reduction with second-phase sampling while the *EV-based* is more effective. The results of the sensitivity tests indicate that the *EV-based* criterion is more robust when the data variability changes. The possible reasons could be that the *EV-based* criterion reduces more sources of uncertainty than *WM-sampling* criterion does, and the *interpolation uncertainty* represented by the kriging error variances has a larger impact on the misfit.

Another way of describing the *EV-based* sampling criterion is to sample at the least-sampled locations, which is intuitively the choice to make when designing second-phase sampling locations. Nevertheless, through the examinations in this chapter, this simple criterion is proven to be the more effective criterion. It is possible that by locating second-phase samples at the sparsely sampled locations, most sources of uncertainty are reduced.

At the same time, only two sampling criteria are analyzed here, which means that both criteria could fail to give the optimal additional sampling locations. For future work, sampling criteria that focus on other sources of uncertainty can be included. On the other hand, for in situ stress, it is possible that there is a trend in the stress. The effect of the trend is excluded in this study. The trend and the spatial variability can both be included in the interpolation. Additional sampling criterion could be proposed to focus on interpreting the trend in the data.

In a word, if only *EV-based* and *WM-sampling* criteria are considered for second-phase sampling locations, *EV-based* criterion should give the optimal second-phase sampling locations.

Chapter 6

Decision analysis in the risk assessment of AIS

Summary

In this chapter, the risk assessment of AIS with the three-level evaluation system is demonstrated using the same data set analyzed in Chapter 3. Risk consists of the possibility and the impact. In the example, the possibility and impact of the AIS are decomposed into 8 and 4 independent factors respectively. The three-level evaluation system is a qualitative way to analyze the potential risk because quantitative approaches are too complex or contain too much uncertainty. Based on the evaluations, the risk can be anticipated and used in decision tree analyses regarding several possible decisions of an operation, including *should the operation proceed, should mitigation be conducted* and *should mild mitigation or rigorous mitigation be chosen.* The example is aimed to demonstrate that decision analysis techniques can lead to a practical risk assessment and give decision makers a better understanding of how the benefit and cost of each decision affect the potential risk and the revenue.

6.1 Introduction

This chapter discusses the approaches to conduct the risk assessment of AIS in detail. Analyzing the risk of AIS is similar to analyzing the risk of natural earthquakes. Therefore, the risk of AIS is interpreted as the possibility of AIS causing unfavorable impacts. Unfavorable impacts refer to the temporary or permanent suspension of operations through to infrastructure damage. The suspension of operations leads to the loss of the revenue and the infrastructure damage leads to repairs and unforeseen expenses. In addition to the monetary loss, there could also be negative social impacts and other uncontrollable consequences.

The ultimate goal of the risk assessment of AIS is to help managers make effective decisions that maximize the production while avoiding triggering AIS. Approaches such as the FSP analysis and the PSHA quantify the risk of AIS. However, the uncertainties in these quantitative approaches are difficult to measure. Therefore, the three-level evaluation system, a quantitative analysis of the risk, is adopted. First, the risk is decomposed into multiple factors. Each factor is an independent variable that affects the risk of AIS. Then each factor is evaluated with a three-level system. The overall risk of AIS is a combined influence from all the evaluated factors. Decision tree analysis is also applied to connect the possibility of AIS with the impact of AIS, which is interpreted as monetary values. Decision tree analysis is especially helpful when dealing with cost-benefit problems.

In this chapter, risk factors related to the risk of AIS are listed and evaluated with the three-level system. The decision tree analysis is explained. The same operation studied in Chapter 3 is analyzed for demonstration here. The example shows that the proposed techniques consider both the possibility and impact of AIS while simplifying the process by adopting qualitative analyses.

6.2 Theory

6.2.1 Estimation of risk with risk factors

Analyzing the risk of AIS means understanding the possibility of AIS and the potential impact of the events simultaneously. Both the possibility and the impact can be decomposed into multiple independent factors. The independent factors are analyzed separately. The possibility of AIS can either be analyzed quantitatively, such as the FSP analysis and the PSHA analysis, or qualitatively with the analysts' experience and expertise using a level-based system. The levels should at least be two, as *low* and *high*. A more common system is to have three levels as *low, medium* and *high* (Newendorp and Schuyler, 2000), similar to a traffic light system. The quantification of the possibility, such as the FSP analysis, can also be categorized into the three levels (e.g. Walsh and Zoback, 2016). Scores are used to represent the risk levels. 0, 1, 2 and 3 are assigned to *none, low, medium* and *high*. Then the possibility is the ratio of the given scores and the maximum score, as

$$P = \frac{\sum_i^{N_r} s_i}{3N_r}, s_i = 0, 1, 2, 3, \tag{6.1}$$

where P is the possibility, s_i is the score of each risk factor, and N_r is the total number of risk factors that are evaluated. In cases where some risk factors cannot be evaluated due to the lack of data, these risk factors are not included in the calculation of the possibility of the risk. Therefore, by assessing the level of each factor, the possibility of AIS is known.

6.2.2 Decision tree and expected value

The decision tree analysis is a common technique in decision analysis (Clemen, 1996; Bratvold et al., 2007). In a decision tree, square nodes mean decisions and circle nodes mean uncertain events (Figure 6.1). Branches after a square or a circle lead to alternatives of a specific decision or possible outcomes. At the end of the decision tree, corresponding consequences are listed after each outcome. All consequences are assigned with values. The probability of each outcome

and the extra costs when choosing certain alternatives are also included in the decision tree.

In a decision tree, the alternative with the highest expected value is the best alternative. The expected monetary value (EMV) is defined as

$$EMV = \sum_{i}^{o} p_i \times V_i \tag{6.2}$$

where o is the total number of all outcomes, p_i is the probability of the ith outcome and V_i is the value of the outcome. EMV can be interpreted as the average value of one alternative after many repetitions of choosing that alternative. In a decision tree, the alternative with a higher EMV is considered as the better choice to make.

Figure 6.1 is a simple decision tree that shows one decision with two alternatives and two outcomes. *Outcome 1* costs $200K\$$ while *Outcome 2* brings $1000K\$$ profit. Numbers in parentheses are the probability of each outcome by choosing the alternative. While choosing *Alternative 2* has a higher possibility of *Outcome 2*, it also costs an extra $20K\$$. To determine which alternative is better, the EMV of each alternative is calculated as follows

$$\begin{aligned} EMV_1 =& (0.24) \times (-200K\$) + (0.76) \times (1000K\$) = 712K\$, \\ EMV_2 =& (0.20) \times (-200K\$) + (0.80) \times (1000K\$) = 760K\$, \end{aligned}$$

where footnotes $_1$ and $_2$ denote *Alternative 1* and *Alternative 2*. Also, any extra costs of alternatives are subtracted from the EMV. This reduces the EMV_2 to $740K\$$. Then at the decision node, the branch with the highest EMV is the alternative to be chosen, which is the number in red at the square in Figure 6.1. The decision tree shows that *Alternative 2* has an EMV of $740K\$$ and *Alternative 1* has an EMV of $720K\$$. Therefore, *Alternative 2* has the highest EMV, meaning it is the better alternative to choose.

With the three-level evaluation of each risk factor, the probabilities of the outcomes in a decision tree can be represented by the possibility of the risk and the consequence of each outcome is anticipated by the evaluation of the

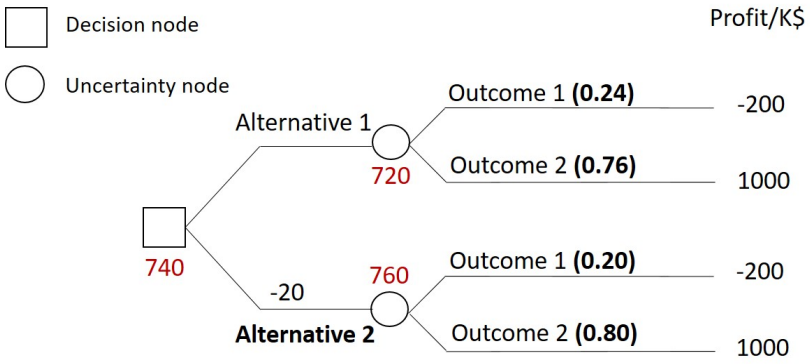

Figure 6.1: A decision tree analysis. Numbers in parentheses are the probabilities of the outcomes. Numbers in red are the EMVs. Word in bold is the alternative with the highest EMV. The notations are the same in the following decision trees.

impact of the risk.

6.3 Risk factors of AIS

The possibility of AIS is controlled by factors listed below, which are mainly based on the industrial shared practice (Canadian Association of Petroleum Producers (CAPP), 2019) and Walters et al. (2015).

1. *Prior seismicity (natural and induced)*: Previous seismic activities are an indicator of the stress state and possible existence of faults and fracture networks. In addition, seismic records also point out which areas are non-seismogenic but prone to AIS under the influence of industry activities. For instance, increase seismic events in the central Oklahoma after 2009 are linked with the increased wastewater disposal activities (Keranen et al., 2014). In this case, the *Prior seismicity (natural and induced)* in the central Oklahoma should be evaluated as *high*.

2. *Proximity to specific geological structures*: There is a relation between the locations of AIS and other large-scale geological structures, such as the crystalline basement and the reef margins (Zhang et al., 2013; Bao and Eaton, 2016; Schultz et al., 2017).

3. *Fracture network*: A fracture network reduces the permeability in the formation. The fracture network acts as conduits between the injection wells and the fault, increasing the pore pressure at the fault (Shapiro et al., 2002, 2003; Igonin et al., 2019).

4. *Fault size*: The magnitude of an earthquake depends on the rupture area and stress drop on the fault during the slip (Stein and Wysession, 2009). In general, the rupture area is correlated with the fault size, and the rupture area affects the magnitude of the earthquake (Stein and Wysession, 2009; Zoback and Gorelick, 2012).

5. *Fault slip potential (FSP)*: The FSP analysis is discussed in detail in Chapter 3. This analysis is a combination of the stress state, the pore pressure state and the fault, as well as their uncertainties.

6. *Adjacent operations*: It has been observed that adjacent operations might increase the risk of AIS because the perturbation of the in situ stress and the pore pressure from other operations can be cumulative.

7. *Concurrent observed seismicity - clustering*: Monitoring the induced seismicity during the operation is important. The observed seismicity points out the direction of the fracturing propagation. The hydraulic fractures should propagate along the direction of the maximum principal stress (Zoback, 2010; Eaton, 2018). Discrepancies between the observed propagation direction and the direction of the maximum principal stress denote the existence of other geological structures. For instance, the lineation of the observed seismicity could indicate possible reactivation of a fault (see the example in Chapter 3).

8. *Concurrent observed seismicity - magnitude*: The increase in the magnitude of the observed seismicity during the operation is a precursor of AIS. The mitigation method implemented by most of regulators around the world, the traffic light system, uses the magnitude of sesimicity as thresholds (Shipman et al., 2018; Kao, 2017). Studies have observed a continuous increase in the magnitudes of observed seismicity before the

magnitude reaches the predetermined thresholds (Atkinson et al., 2016; Lee et al., 2019).

All factors can be updated as more information is obtained. Note here no factors related to the operation, such as injection volume and rate, are listed. Because those factors do not directly affect the possibility of AIS but influence the risk factors listed above. For instance, high injection rate and volume increase the pore pressure at the pre-existing fault, and the FSP increases, hence the possibility of AIS increases. Therefore, the injection parameters are indirectly included in the analysis.

The impact of AIS is perceived as the expected losses caused by AIS (Tyagunov et al., 2004). Since AIS is a type of earthquake, the impact of AIS is analyzed in the same way as natural earthquakes. Four factors are recognized (Walters et al., 2015):

1. *Population*: The population near the area of interest is a crucial factor associated with the impact. If the area is close to a populated area, the impact of AIS becomes high as more people are exposed.

2. *Critical facilities*: AIS, like natural earthquakes, could cause damage to critical facilities. The analysts should be aware of any critical facility, such as major dams and nuclear power plants, that are adjacent to the area of interest.

3. *Structures*: It is important to be aware of how structures and infrastructures near the proposed operation would be influenced by the AIS. The possible damage to the equipment on site and wellbore integrity should also be considered.

4. *Environment*: Analysts should search for any conservation sites and protected areas near the operation. Earthquakes can trigger landslides and fire (Silva et al., 2017), which could lead to severe environmental damages.

Analysts can conduct evaluations of the factors to calculate the possibility of AIS and quantify the expected loss of the AIS. Interdisciplinary cooperation is encouraged to increase the accuracy of the evaluations with all available

knowledge. At the same time, due to the lack of knowledge, some factors might not be evaluated prior to the operation. If there is no recorded previous seismicity, or observed fracture networks, no evaluations should be assigned to these factors. The same idea works for *concurrent observed seismicity - clustering* and *concurrent observed seismicity - magnitude*. Because there is no operation yet, there may not be any observed seismicity. All factors can be re-evaluated once more information becomes available.

6.4 Example

The following is an example of the risk assessment of an operation. The same operation is studied for FSP analysis in Chapter 3. Here the risk assessment is done both before and during the operation. Results from the risk assessments are used in decision tree analyses to demonstrate how the the anticipated risk affects the decision-making process. There are four risk assessments and three decision tree analyses. The risk assessments are

1. The assessment of the initial risk of AIS prior to the operation.
2. The risk assessment assuming the worst-case scenario where the possibility of AIS is 100%.
3. The risk assessment during the operation with observed seismic events.
4. The risk assessment with proposed mitigation methods.

Along with the risk assessments, decision tree analyses are done considering the following decisions:

1. Based on the risk assessment prior to the operation, should the operation proceed?
2. During the operation, with the risk increasing, should the operation be mitigated?
3. If there are two available mitigation methods, and the more effective mitigation method costs more money, which one should be chosen?

The less effective mitigation is referred to as mild mitigation and the more effective mitigation as rigorous mitigation. Before doing the risk assessment, three assumptions are made:

1. Injecting fluids into formations increases the risk of AIS.
2. Any form of mitigation would reduce the risk of AIS.
3. The decision makers are risk-neutral.

6.4.1 Prior to the operation

The workflow of the risk assessment prior to the operation is

1. Calculate the possibility and the impact of AIS by evaluating the risk factors.
2. Apply the decision tree analysis to decide if the operation should proceed.

The operation took place in the west of Fox Creek, Alberta in 2016, as shown in Figure 6.2. The risk of AIS is assessed based on the evaluations of the risk factors. Each factor is analyzed with the available knowledge of the area prior to the operation. Published studies in the Fox Creek area are considered as the available information prior to the operation. Earthquakes with local magnitude (M_l) greater than 2 have occurred in the Fox Creek area before the operation. Some of them were induced by industrial activities (Schultz et al., 2015). Hence the *Prior seismicity (natural and induced)* is evaluated as *medium*. The operation aims at the tight shale reservoir in the Duvernay formation, which is approximately $500m$ above the Precambrian basement, which is a critical component affecting the occurrence of AIS. Therefore the factor *Proximity to geological structures* is evaluated as *medium* as well. The seismic cross section shows multiple strike-slip faults in the area, as well as the fault sizes (Figure 3.3). Because there are no public seismic data, the existence of a fracture network is unknown. Hence this factor cannot be evaluated before the operations. The FSP analysis is done in Chapter 3. The results indicate that the FSP's of multiple faults in this area are *low* (see Figure 3.7(a) and (c)). During the proposed operation time range, there were no other operations

within a $5km$ radius (Eaton et al., 2018). So factor *Adjacent operations* is evaluated as *none*. Table 6.1 lists the analyses and evaluations of all risk factors contributing to the possibility of AIS. Factors that cannot be evaluated due to lack of data are labeled as *Unknown*. The risk factors related to the concurrent observed seismicity during the operation are not evaluated and labeled as *N/A*. Factors that are labeled as *unknown* and *N/A* are excluded in the calculation of possibility of AIS in Equation 6.1. After the evaluations, the possibility of AIS is calculated using Equation 6.1. The possibility of AIS prior to the operation is 53%, as shown in Figure 6.4(a). An additional risk evaluation is done assuming the worst-scenario. The possibility of AIS in the worst-case scenario is set to 100%.

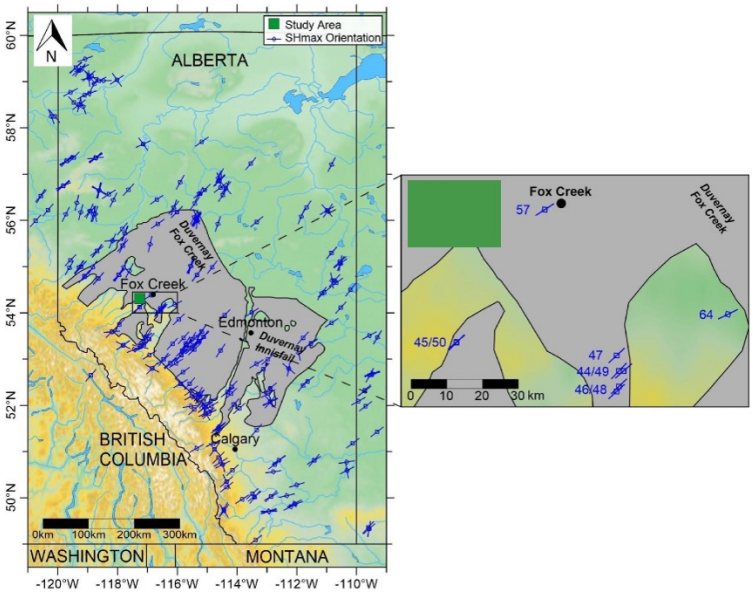

Figure 6.2: Map view of the location of the operation site (green rectangles in both maps). Figure modified from Zhang et al. (2019).

The impact of the risk is also determined by the evaluations of relevant factors. The closest town near the operation is Fox Creek with a population of about 2,000 people. There are no buildings exceeding $10m$ and all the buildings could withstand light ground shaking. And there are no major facilities or conservation sites around the operation site. The detailed analyses are shown in Table 6.2. Based on the evaluations, the impact of the AIS of this operation is considered as low to moderate and casualties are not anticipated as part of

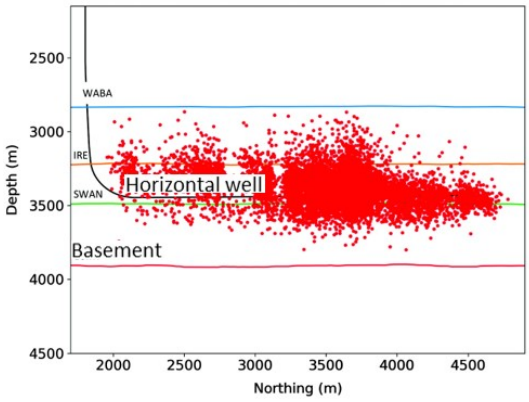

Figure 6.3: Depth of the operations. Black line indicated the horizontal well. The depth of the basement is indicated by the red line with *BSMT*. Figure modified from Poulin et al. (2019).

the impact of the AIS. Therefore, the expected loss of AIS is smaller than the expected revenue of the operation.

With the risk assessment done prior to the operation, the decision, *should the operation proceed*, is analysed using the decision tree, as shown in Figure 6.4(b). In this decision tree analysis, two outcomes are identified, *AIS* and *no AIS*. The monetary values of the two outcomes are given based on the impact evaluation of the risk. When there is no operation, the profits are 0 in both outcomes. Based on the analysis of the risk factors related to the impact, the monetary loss of an operation with *AIS* is assigned as $-200K\$$ and there is no monetary loss with the outcome *no AIS*. Meanwhile, the alternative *operation* comes with the revenue of $1000k\$$. These are just illustrative values based on the anticipated impact of AIS and the production of the wells. From Figure 6.4(b), we can see that the alternative *operation* has a higher *EMV*, hence the operation should proceed.

6.4.2 During operation

The workflow of the risk assessment during the operation is

1. Re-assess the possibility and impact of AIS with the observed seismic data.

2. Apply the decision tree analysis to determine if voluntary mitigation is

Table 6.1: Evaluations of risk factors related to possibility of AIS prior to the operation.

Variable	Analysis	Evaluation
Prior seismicity (natural and induced)	A correlation between the observed seismic events ($> M_l$ 0) and previous hydraulic operations have been found in the Fox Creek area (Schultz et al., 2015). Several induced seismic events were above M_l 2.	Medium
Proximity to geological structures	The operation site is about $7km$ to the reefs (based on the map shown in Figure 6.2) and about $500m$ above the basement (Figure 6.3).	Medium
Fracture network	Due to the lack of data, the presence of fracture networks are unknown.	Unknown
Fault size	The seismic data show there are several strike-slip faults in the area (Fault D, E, F, G and H in Figure 3.7(a)). Faults are between $2km$ to $6km$ long.	High
Fault slip potential	The fault slip potential analysis shows the faults have low slip potentials (Figure 3.7).	Low
Adjacent operations	There are no other operations operating at the same time within a $5km$ radius (Eaton et al., 2018).	None
Concurrent observed seismicity - clustering	No operation yet.	N/A
Concurrent observed seismicity - magnitude	No operation yet.	N/A

needed.

3. Re-assess the possibilities of AIS assuming applying different mitigation methods.

4. Apply the decision tree analyses to determine which mitigation method to implement.

During the operation, with more information acquired, evaluations of the risk factors should be updated. The operation started on October 29, 2016. Suppose the risk assessment is conducted on November 09, 2016. Observed

Table 6.2: Evaluations of risk factors related to the impact of AIS. The evaluations are applicable to the risk assessments prior to the operation and during the operation.

Variable	Analysis	Evaluation
Population	1720 (Statistics Canada, 2017).	Low
Critical facilities	None within $5km$ radius. The closest dam is the Iosegun Lake Stabilization Dam, $15km$ north of Fox Creek, with consequence classification as low (Alberta Government, 2020).	None
Structures	Based on the National Building Code seismic hazard calculator (Natural Resources Canada, 2019), the probability of exceeding $0.079g$ Peak Ground Acceleration in Fox Creek is less than 2%. The $0.079g$ Peak Ground Acceleration corresponds to the light ground shaking according to the Mercalli intensity scale. Given the fact that AIS has exceeded M_l 4 near Fox Creek area (Schultz et al., 2017), it is reasonable to infer that buildings in Fox Creek could experience shaking when AIS with large magnitudes (e.g. $> M_l$ 4) happens. Also, since the maximum building height in Fox Creek is $10m$ (Town of Fox Creek, 2016), damages to the structures are possible due to AIS with large magnitudes. Moreover, AIS can cause damage to the equipment on site and wellbore integrity, which is expensive to repair.	Medium.
Environment	The operation is not within 10km radius of near any conservation sites, protected area nor national parks. The closest conservation site is $62km$ northwest of Fox Creek (Alberta Conservation Association, 2016).	None

seismic events from the beginning of the operation to the time the risk assessment is conducted are used. The observed seismic data are from Eaton et al. (2018), shown in Figure 6.5.

From Figure 6.5(a) we can see that the observed seismic events do not propagate along the direction of the maximum principal stress, which is the maximum horizontal stress (S_{Hm}) in this area (Bell and Grasby, 2012). The difference between the propagation direction of the seismic events and S_{Hm}

indicate the possibility of the presence of fracture networks. The FSP analysis is updated because the fracture network connects the fault with the injection wells and the pore pressure at the fault increases more than first anticipated. The calculation of the updated FSP is explained in Chapter 3. The detailed analysis of the presence of the fracture network can be found in Igonin et al. (2019). The faults close to the injection wells have high FSP's with the new understanding of the fracture network. Therefore, the risk factor *fault slip potential* change from *low* to *high*. In addition, the seismic events in the red oval appear to lineate along a fault, which is fault D in Figure 3.3. The distribution of the observed seismic events cause the change of the risk factor *concurrent observed seismicity - clustering* from *unknown* to *high*. With the operation proceeding, more fluids are injected in to the Duvernay formation. In Figure 6.5(b) we can see that as the amount of fluids in the Duvernay formation increases, the magnitudes of the seismic events are increasing, especially towards the end of the figure. Meanwhile all concurrent seismic events are below moment magnitude (M_w) 1.5. The risk factor *concurrent observed seismicity - magnitude* is evaluated as *medium*. The updated evaluations are listed in Table 6.3.

The possibility of the AIS is re-calculated, as shown in Figure 6.6(a). Facing the increased possibility of AIS, the decision tree analysis is conducted about the question of *mitigation or not*. The impact remains unchanged during the operation because the additional information does not affect the description of the impact. The evaluations are shown in Table 6.2. Therefore, in the decision tree analysis, two outcomes, *AIS* and *no AIS*, still result in $200k$\$ loss and no loss respectively. The decision tree analysis is shown in Figure 6.6(b). Suppose the alternative *mitigation* means using the mild mitigation, which has an extra cost of $-20k$\$. With the mild mitigation method, the risk level of *fault slip potential* changes from *high* to *low* and the risk level of *concurrent observed seismicity - clustering* changes from *high* to *medium*. The possibility of AIS with the mild mitigation is shown in Figure 6.6(a). From Figure 6.6(b) we can see choosing to do the mitigation still has a higher EMV than not doing the mild mitigation.

Mitigation can be mild or rigorous depending on the anticipated risk. Decision tree analysis can also be applied when choosing among different mitigation

Table 6.3: Evaluations of risk factors related to possibility of AIS during the operation with the observed seismic data.

Variable	Analysis	Evaluation
Prior seismicity (natural and induced)	Same as the evaluation prior to the operation in Table 6.1.	High
Proximity to geological structures	Same as the evaluation prior to the operation in Table 6.1.	Medium
Fracture network	The observed seismic events indicate the possible existance of a fracture network (Igonin et al., 2019).	High
Fault size	Same as the evaluation prior to the operation in Table 6.1.	High
Fault slip potential	The fault slip potential analysis is updated by removing fault E and including a pre-existane fracture network. The updated FSP results are shown in Figure 3.12(a).	High
Adjacent operations	Same as the evaluation prior to the operation in Table 6.1.	None
Concurrent observed seismicity - clustering	Lineation at the west side of the most-left well means the possible reactivation of a fault as shown in Figure 6.5(a).	High
Concurrent observed seismicity - magnitude	Magnitudes of the observed seismicity show an increasing pattern but all the seismic events are below M_w 1.5 as shown in Figure 6.5(b).	Medium

methods. Here, two alternatives, *mild mitigation* and *rigorous mitigation*, are analyzed using the decision tree. If applying the rigorous mitigation method, the risk levels of *fault slip potential, concurrent observed seismicity - clustering* and *concurrent observed seismicity - magnitude* all change from *high* to *low*. The possibility of AIS with the rigorous mitigation are calculated and shown in Figure 6.6(a). In Figure 6.6(c), the EMV of the operation with the rigorous mitigation is higher. Therefore, it is logic to do the mitigation and choose the rigorous method if possible.

6.5 Discussion

In the example, the possibility and the impact of AIS are decomposed into multiple factors. Each factor is evaluated based on the three levels, being *low, medium* and *high*. If the factor does not exist, it is labeled as *none*. If the factor is not known or applicable to be evaluated, it is labeled as *unknown* or *N/A*. The evaluations are then used in the decision tree analyses. The possibility of AIS is the lowest prior to the operation, and increases with the operation. With mitigation, the possibility decreases. The possibilities of AIS under different circumstances are listed in Table 6.4. The assessment of the impact of AIS is low to moderate, indicating the expected loss of AIS from this operation is low.

Table 6.4: Probabilities of the AIS under different scenarios.

Scenario	Probability of AIS
Prior to the operation	53%
Worst-case	100%
During the operation	75%
With mild mitigation	63%
With rigorous mitigation	54%

The risk assessment prior to the operation provides insights on what the initial risk is in the area of interest given the current knowledge. Risk of AIS should be assessed prior to the operation without considering the influence of the operation, as well as assuming the worst-case scenario. The initial risk affects the plan of the operation. Calculating the worst-case scenario is important because it is a conservative and simple approach to anticipate the risk (Silva et al., 2017). The decision tree analysis of *should the operation proceed* shows that the better alternative is to do the operation. Even assuming the worst-case scenario, the EMV of doing the operation still outweighs the EMV of not doing the operation. This is because the impact of AIS during the operation is anticipated as the low to moderate.

With the ongoing operation, risk is increased and should be re-evaluated with more available information. The updated risk assessment is used in the decision tree analyses of the decisions, *mitigation or not* and *which mitigation to choose*. Here, either the mild mitigation or the rigorous mitigation is assumed

to be effective in reducing the possibility of AIS. In this operation, implementing voluntary mitigation reduces the possibility of AIS and the EMV of the operation is increased despite the extra cost of the mitigation. Furthermore, the rigorous mitigation gives a greater EMV even with a higher cost. Decision tree analyses are very helpful when resolving cost-benefit situations.

It is worth mentioning that EMVs in the example are not the exact monetary values of the operation by choosing those alternatives. They are the weighted average values. In other words, if the operation is conducted for many times, which could never be true, the averaged monetary values of choosing different alternatives are EMVs.

Comparing to the FSP analysis, this approach includes both the possibility and impact of the risk. Instead of assessing the risk as a whole, analyzing individual risk factors and combining the evaluations together afterwards simplify the process of a risk assessment. However, it is crucial to define independent factors, because the risk can only be calculated using Equation 6.1 if the variables are independent. Under this assumption, correct evaluations of factors are supposed to give us a relatively precise assessment of the risk.

Another advantage of this approach is that the analysis process is easy and requires little computational effort. Unlike PSHA, decomposing the risk of AIS and assessing multiple risk factors qualitatively do not require complex quantification of the uncertainty or sophisticated equations to predict the ground motions. The risk can be easily re-assessed once more information is obtained during the operation. Re-assessing the risk shows how the operation alters the risk. Utilizing the decision tree analysis helps understand how the risk and different mitigation methods affect the consequences of the operation.

At the same time, this approach is subjective to a certain degree. Evaluating risk factors depends on the analysts' personal judgements and expertise. Therefore, though the decision analysis is a subject related to economy and engineering, geological and geophysical experts should also be the analysts or at least work closely with the analysts conducting the risk assessment of AIS.

In addition to subjectivity, this approach ignores the time factor. Taking the third decision tree analysis, *mild or rigorous mitigation*, for example, though the rigorous mitigation should be the better choice to make as it results in a

higher EMV. Sometimes, the decision makers might be reluctant to do so. There are several reasons. First, in this decision tree, only the monetary values representing the expected revenue and loss are included. In a real operation, the time spent on the operation also affects the revenue. This is accounted for by including a negative amount for postponed revenues. If the rigorous mitigation is more effective but delays the operation, the extra time spent on the operation is not included in this analysis. On the contrary, the mild mitigation might not be as effective, but it is fast and costs less. In this case, the postponed revenues need to be included for a more accurate decision tree analysis.

The outcomes in the decision tree analyses in the example are described based on the anticipated impact of AIS. Here the non-monetary factors, such as public opinions are not included. Including these factors is difficult yet achievable (Clemen, 1996).

Moreover, the decision tree analyses assume the decision makers are risk-neutral. In fact, decision makers can be either *risk-averse, risk-neutral* or *risk-seeker*. Different choices are made with different attitudes towards the risk. How the decision makers anticipate the risk should be discussed with the analysts at the very beginning of the risk assessment of AIS (Bratvold et al., 2007; Newendorp and Schuyler, 2000; Clemen, 1996).

In addition, data analysis is helpful when determining the individual risk factors. Pawley et al. (2018) combine machine learning algorithm with PSHA and identify different factors related to the induced seismic events in the Duvernay play and their importance respectively. With sufficient data, data analysis can also be applied to understand which mitigation methods are more effective under specific geological environments.

6.6 Conclusion

This chapter demonstrates the workflow of a complete risk assessment of AIS with a case study. The risk consists of the possibility and the impact of AIS. These two aspects are analyzed separately. The anticipated risk is utilized in the decision-making process of the operation through the several decision tree analyses.

Because the possibility of AIS is affected by various factors, these factors are considered as the risk factors and evaluated independently. Instead of using quantitative evaluations like the FSP analysis and the PSHA, a qualitative method called the three-level evaluation system is applied here. Each factor is assessed and labeled *low, medium* and *high*. If the factor does not exist, the factor is evaluated as *none*. If the information for evaluating certain factors is missing, the factor is considered as *unknown* and is excluded in the calculation of the possibility. Here two factors, *concurrent observed seismicity - clustering* and *concurrent observed seismicity - magnitude*, are not applicable when assessing the risk prior to the operation. Hence they are labeled as *N/A*. Using this qualitative evaluation system requires less computation and can be updated easily once more information is available. It is a practical risk assessment approach.

By implementing the decision tree analysis, both the possibility and the impact of AIS are included in the decision-making process. This is necessary because the objective of the risk assessment is to make better decisions with the understanding of the risk. Instead of interpreting the risk assessment intuitively, the decision tree analysis specifically illustrates how the anticipated risk affects the expected values of the operation by making certain decisions. More costly decisions may statistically lead to better results (revenues) if they reduce the possibilities of negative outcomes. In this case, the negative outcome is the occurrence of AIS.

It is important to emphasize that in this case only monetary values are considered. Decision makers should routinely take additional influences into consideration such as the cost of the operation delay, political and/or societal impact of their decisions. Yet the values of these factors are more difficult to assess statistically.

6.7 Acknowledgement

The work in this chapter is inspired by the author's personal conversations with Tim Tyrrell from XTO Energy and Sobhi Alhashwa from Ovintiv. The author would like to thank the kind help from Tim and Sobhi, and all the people who

were willing to share their companies' risk assessments of AIS. This chapter would not be possible without them.

Figure 6.4: (a). Risk evaluations prior to the operation. Factors labeled as *Unknown* and *N/A* are excluded in the calculation of the possibility of AIS. The evaluations in the *prior to the operation* scenario are the same as in Table 6.1. In the *worst-case* scenario, all risk factors that can be evaluated prior to the operation are considered as *high* and the possibility of AIS is 100%. (b). The decision tree analysis of *should the operation proceed*? The possibilities of the outcomes are based on the possibilities in (a). The monetary value of each outcome is based on the assessment of the impact of the AIS (Table 6.2). Detailed analyses are in the main context.

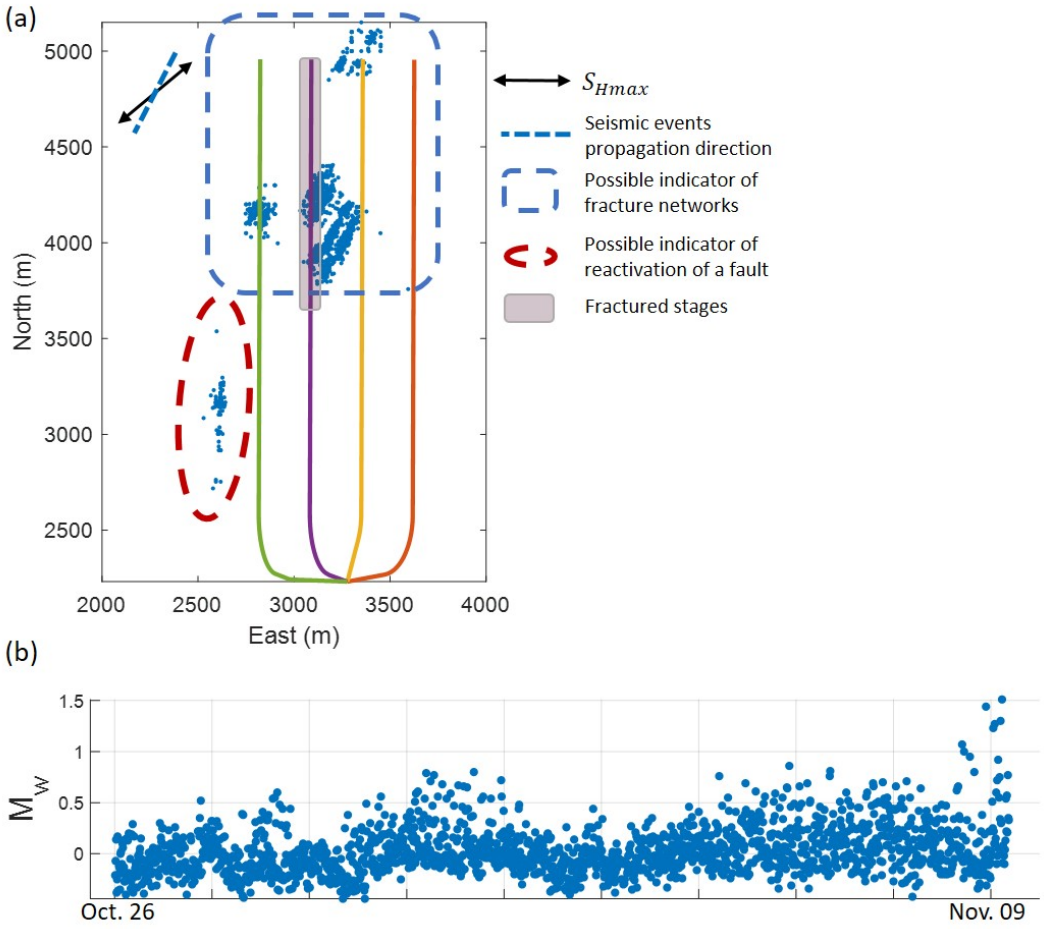

Figure 6.5: Observed seismic events (blue dots) at the operation site from October 26, 2016 to November 09, 2016. Data from Eaton et al. (2018). (a). Map view of the observed seismic events and the locations of the four horizontal wells. The dashed blue line represents the propagation direction of the seismic events in the blue dashed box. The maximum horizontal stress is the maximum principal stress in the area, which is 45° to the north (Bell and Grasby, 2012). The seismic events in the dashed red oval indicates the possible reactivation of a fault. The shaded area indicates the stages that have been fractured. (b). Magnitudes of the observed seismic events shown in (a).

Figure 6.6: (a). Evaluation of each risk factor during the operation. Evaluations in the *during the operation* scenario are the same as in Table 6.3. In the *with mild mitigation* scenario, risk factor, *concurrent observed seismicity - clustering* is changed from *high* to *medium*. In the *with rigorous mitigation* scenario, both *concurrent observed seismicity - clustering* and *concurrent observed seismicity - magnitude* are evaluated as *low*. (b). The decision tree analysis of *should the operation be mitigated*. The possibilities of AIS under the *during the operation* and the *with mild mitigation* scenarios are used. (c). The decision tree analysis of *should mild or rigorous mitigation be implemented*. The possibilities of AIS under the *with rigorous mitigation* and the *with mild mitigation* scenarios are used. In (b) and (c), the monetary values are based on the evaluation of the impact of AIS in Table 6.2.

Chapter 7

Conclusions and suggested future research

Risk assessment of AIS is vital as long as the industrial activities have the potential of causing AIS. Through this thesis, multiple aspects of the risk assessment are analyzed extensively.

In **Chapter 2** and **Chapter 3**, the fault slip potential (FSP) analysis is studied. The FSP analysis calculates the likelihood of fault reactivation with the available knowledge. The 3D FSP analysis proposed in this thesis is based on the consideration of the depth variations of in situ stress and pore pressure. These two chapters shows how the current knowledge of relative parameters affects the accuracy of FSP and the importance of using additional information to update the FSP analysis whenever we can.

The contributions of **Chapter 2** and **Chapter 3** are

1. Proving the Monte Carlo simulations are capable of replacing analytical solutions in the FSP analysis;
2. Including the horizontal stress variances in depth in the FSP analysis;
3. Introducing the safety distance to understand the influence of the uncertainty on the FSP results;
4. Including the slip direction analysis to validate the input parameters of the FSP analysis; and

5. Updating the FSP analysis with additional information to create a better FSP analysis.

This project demonstrates that

1. Both the horizontal in situ stresses and pore pressures can vary from layer to layer. They are not well described by a constant depth gradient.

2. The FSP analysis calculates the likelihood of fault reactivation based on the current knowledge. Including the stress variations in depth in the FSP analysis shows at which depth the fault is more likely to fail.

3. Besides the 3D FSP analysis, the analyses of the slip directions and the safety distance are alternative approaches to utilize the available knowledge. Comparing the slip directions with the focal mechanism analyses verifies the inputs of the FSP analysis. The histograms of the safety distance represent the uncertainty in the results of the FSP analysis.

4. Comparing the 3D FSP analysis with the analysis of the recorded seismic events, the current knowledge of the stress regime and other geomechanical parameters is tested and updated if necessary. The discrepancies between these two analyses indicate the limited or incorrect knowledge of the FSP parameters.

5. Because of the simplicity and minimum computational requirements of the 3D FSP analysis, the same analysis can be updated once more information available. This is an effective and proactive approach of utilizing the observed seismic data besides using them as an indicator of the AIS. The updated knowledge and 3D FSP analyses can be implemented in future risk assessments in the same area.

At the same time, the 3D FSP analysis has several limitations that can be addressed in future studies.

1. The FSP analysis only studies the possibility of fault reactivation. Because there is not a clear correlation between the possibility of reactivation and the resulting magnitude. Thus a high FSP does not necessarily

mean a high risk of AIS. How the FSP is linked to the impact needs to be further investigated.

2. Only the spatial locations of the observed seismic events are compared with the 3D FSP results. Neither the depth nor the magnitude of each event is included in the FSP analysis in **Chapter 3**. These two parameters are suggested to be included in future studies. The depths of seismic events can justify the proposed vertical pore pressure gradient variations and the estimation of the in situ stress. The magnitudes of seismic events can further indicate the pattern of induced seismic events and their relations with the reactivation of a possible fault.

The next objective of the thesis is to provide the optimal additional stress sampling locations, which is discussed in **Chapter 4** and **Chapter 5**. First in **Chapter 4**, the main interpolation method studied in this thesis, kriging, is explained. Then two sampling criteria aimed to improve the kriging results are listed, namely the modified *Warrick-Myers(WM) sampling* criterion and the *error-variance(EV) based* sampling criterion.

The contributions of **Chapter 4** and **Chapter 5** are

1. Proposing two different sampling criteria that are suitable for second-phase sampling; and

2. Demonstrating that when sampling at the locations with the highest error variances, the additional samples are most valuable as they bring the largest misfit reduction in the prediction.

The comparisons these two criteria show that

1. There are six different sources of uncertainty in the interpolated results using kriging. *WM-sampling* criterion focuses on reducing the uncertainty generated during the creation of the variogram model. The *EV-based* criterion is based on the error variance given by kriging. This error variance is considered as the interpolation uncertainty.

2. Additional samples improve the interpolation results and reduce the misfit. When the second-phase samples given by the two criteria respectively

differ, the misfit reduction is higher on average by adding the second-phase samples given by the *EV-based* criterion. This means that when designing the second-phase sampling locations, adding samples based on their kriging error variances would result in the greatest reduction on the misfit.

3. *EV-based* criterion is more robust when the spatial relations of the samples (the sill, the range and the nugget) or the sample size changes.

Again, there are many opportunities for future studies.

1. In this study, two criteria targeting two sources of uncertainty are discussed. More criteria focusing on the other four sources of uncertainty could be included and studied as well.

2. For using kriging to interpolate the in situ stress, it is reasonable to take the spatial trend of the stress into consideration, especially when interpolating the regional in situ stress. Kriging specifies the exclusion of any spatial trend in the samples. Therefore, it is suggested to combine a spatial regression model with the kriging when doing the interpolation of the regional stress.

3. Here only the stress measurements are considered. Incorporating other types of data, such as seismic data and well data, and conducting co-kriging are also recommended. These types of data are also able to illustrate the change of the in situ stress within one area.

The last part of the thesis proposes to adopt techniques from the decision analysis to the risk assessment of AIS. The main techniques mentioned here are the three-level risk evaluation system and the decision tree analysis. Including these techniques improves the understanding of the actual risk and assists the decision making process.

The contributions of **Chapter 6** are

1. Identifying the limitations of using quantitative approaches, such as the FSP analysis and PSHA, to measure the risk of AIS;

2. Listing multiple independent factors related to the risk of AIS;

3. Proposing to use a three-level evaluation system to assess different risk factors qualitatively;

4. Implementing the decision tree analysis to solve the cost-benefit problems during an operation;

5. Conducting a complete risk assessment of a hydraulic fracturing operation in Fox Creek using the techniques mentioned above; and

6. Updating the risk assessment during the operation with observed seismicity and using the updated version to better assist with the decision-making process.

Chapter 6 illustrates that

1. The three-level risk evaluation is a qualitative assessment of the risk. This system requires the understanding of all types of risk factors of the AIS and considers both the possibility and the impact of the risk of AIS.

2. Two outcomes are considered here, namely *no AIS* and *causing AIS*. The influence of the anticipated risk of AIS on the expected monetary values of different outcomes is shown with the decision tree. The decision tree analysis also shows how different decisions affect the risk and the expected values.

For future studies, it is suggested that

1. The outcomes are only divided as *no AIS* and *AIS*. Other descriptions of the outcomes can be included. For example, the outcomes can be grouped by the magnitude of AIS.

2. The risk assessment of AIS should be conducted routinely. Considering the risk during the planning stage and updating the risk with more information show how the anticipated risk affects the decision-making process. Understanding this impact can increase the effectiveness and efficiency of the operation and reduce the risk of AIS.

In conclusion, this thesis studies three parts of the risk assessment of AIS and proposes several improvements. During the course of this whole project, one great obstacle is the lack of geological and geophysical understanding of the detailed process of triggering AIS with injection. The mechanism is well-developed but there are still some questions remaining unanswered, such as

1. Why are some areas more prone to AIS than other areas?
2. How does the injection process trigger AIS exactly?
3. Is it possible to detect forewarning of AIS with real-time monitoring?

Early observations of AIS due to injection was in the 1960s (Healy et al., 1968), yet AIS is still a risk with limited understanding and assessments. With constant research and interdisciplinary cooperation, the risk of AIS will be better assessed.

Bibliography

Alaniz-Álvarez, S. A., G. Tolson, and Á. F. Nieto-Samaniego, 2000, Assessing fault reactivation with the reactiva program: Journal of Geoscience Education, **48**, 651–657.

Alberta Conservation Association, 2016, Alberta Conservation Guide.

Alberta Government, 2020, Alberta Dam Safety Map, http://damsafetymap.alberta.ca/ (accessed January 25, 2020).

Armstrong, M., 1984, Improving the estimation and modelling of the variogram, *in* Geostatistics for natural resources characterization: Springer, 1–19.

Atkinson, G. M., D. W. Eaton, H. Ghofrani, D. Walker, B. Cheadle, R. Schultz, R. Shcherbakov, K. Tiampo, J. Gu, R. M. Harrington, et al., 2016, Hydraulic fracturing and seismicity in the Western Canada Sedimentary Basin: Seismological Research Letters, **87**, 631–647.

Aven, T., 2015, Risk analysis: Wiley Blackwell.

Baker, J. W., 2013, An introduction to probabilistic seismic hazard analysis: White paper, version, **2.0**, 79.

Ballantine, J. P., and A. R. Jerbert, 1952, Distance from a line, or plane, to a point: The American Mathematical Monthly, **59**, 242–243.

Bao, X., and D. W. Eaton, 2016, Fault activation by hydraulic fracturing in Western Canada: Science, **354**, 1406–1409.

Barthwal, H., M. Van der Baan, et al., 2017, Stress perturbations and microseismicity induced by hydraulic fracturing: Presented at the 51st US Rock Mechanics/Geomechanics Symposium, American Rock Mechanics Association.

Bell, J., and S. Grasby, 2012, The stress regime of the Western Canadian Sedimentary Basin: Geofluids, **12**, 150–165.

Bell, J., P. Price, and P. McLellan, 1990, In-situ stress in the Western Canada Sedimentary Basin: Bulletin of Canadian Petroleum Geology, **38**, 157–157.

Bhattacharyya, A., 1943, On a measure of divergence between two statistical populations defined by their probability distributions: Bull. Calcutta Math. Soc., **35**, 99–109.

Bommer, J. J., S. Oates, J. M. Cepeda, C. Lindholm, J. Bird, R. Torres, G. Marroquín, and J. Rivas, 2006, Control of hazard due to seismicity induced by a hot fractured rock geothermal project: Engineering Geology, **83**, 287–306.

Bott, M. H. P., 1959, The mechanics of oblique slip faulting: Geological Magazine, **96**, 109–117.

Bowers, G. L., et al., 1995, Pore pressure estimation from velocity data: Accounting for overpressure mechanisms besides undercompaction: SPE Drilling & Completion, **10**, 89–95.

Bratvold, R., and S. Begg, 2010, Making good decisions: Society of Petroleum Engineers.

Bratvold, R., J. Bickel, and H. Lohne, 2007, Value of information in the oil andgas industry: Past, present and future: Paper SPE 110378 presented at the SPE Annual Conference and Exhibition, Anaheim, California, USA, 11–14.

Canadian Association of Petroleum Producers (CAPP), 2019, Hydraulic fracturing industry shared practices: Anomalous induced seismicity due to hydraulic fracturing.

Clemen, R. T., 1996, Making hard decisions: an introduction to decision analysis, 2nd ed.: Brooks/Cole.

Cressie, N., 1990, The origins of kriging: Mathematical geology, **22**, 239–252.

Cui, A., R. Brezovski, K. Glover, et al., 2013, Controls of anisotropic in-situ stress and permeability in optimization of wells and hydraulic fractures for unconventional reservoirs: examples from the Western Canada Sedimentary Basin: Presented at the 47th US Rock Mechanics/Geomechanics Symposium, American Rock Mechanics Association.

Davis, B. M., and L. E. Borgman, 1979, Some exact sampling distributions for variogram estimators: Journal of the International Association for Mathe-

matical Geology, **11**, 643–653.

———, 1982, A note on the asymptotic distribution of the sample variogram: Journal of the International Association for Mathematical Geology, **14**, 189–193.

Davis, J. C., 2002, Statistics and data analysis in geology, 3 ed.: John Wiley & Sons, Inc.

Delmelle, E., 2009, Spatial sampling: The SAGE handbook of spatial analysis, **183**, 206.

Delmelle, E. M., 2012, Spatial sampling: Handbook of Regional Science, 1385.

Do, C. B., 2008, Stanford University CS229 : Machine Learning, Lecture notes: The multivariate Gaussian distribution.

Dunn, L., G. Schmidt, K. Hammermaster, M. Brown, R. Bernard, E. Wen, R. Befus, and S. Gardiner, 2012, The Duvernay Formation (Devonian): sedimentology and reservoir characterization of a shale gas/liquids play in Alberta, Canada: Presented at the Canadian Society of Petroleum Geologists - Annual Convention, Canadian Society of Petroleum Geologists.

Eaton, B. A., 1975, The equation for geopressure prediction from well logs: Presented at the Fall meeting of the Society of Petroleum Engineers of AIME, Society of Petroleum Engineers.

Eaton, D. W., 2011, 2-D finite-difference modelling of pore-pressure diffusion in heterogeneous anisotropic porolelastic media: Implications for induced microseismicity: Presented at the Recovery – 2011 CSPG CSEG CWLS Convention, Canadian Society of Exploration Geophysicists.

———, 2018, Passive seismic monitoring of induced seismicity: Fundamental principles and application to energy technologies: Cambridge University Press.

Eaton, D. W., N. Igonin, A. Poulin, R. Weir, H. Zhang, S. Pellegrino, and G. Rodriguez, 2018, Induced seismicity characterization during hydraulic-fracture monitoring with a shallow-wellbore geophone array and broadband sensors: Seismological Research Letters, **89**, 1641–1651.

Economides, M. J., and K. G. Nolte, 2000, Reservoir stimulation: John Wiley & Sons Chichester, NY.

Eidsvik, J., T. Mukerji, and D. Bhattacharjya, 2015, Value of information

in the Earth sciences: Integrating spatial modeling and decision analysis: Cambridge University Press.

Eissa, E., and A. Kazi, 1988, Relation between static and dynamic young's moduli of rocks: International Journal of Rock Mechanics and Mining & Geomechanics Abstracts, **25**.

Ellsworth, W. L., 2013, Injection-induced earthquakes: Science, **341**, 1225942.

Eyre, T. S., D. W. Eaton, D. I. Garagash, M. Zecevic, M. Venieri, R. Weir, and D. C. Lawton, 2019, The role of aseismic slip in hydraulic fracturing–induced seismicity: Science advances, **5**, eaav7172.

Gaucher, E., M. Schoenball, O. Heidbach, A. Zang, P. A. Fokker, J.-D. van Wees, and T. Kohl, 2015, Induced seismicity in geothermal reservoirs: A review of forecasting approaches: Renewable and Sustainable Energy Reviews, **52**, 1473–1490.

Gischig, V. S., and S. Wiemer, 2013, A stochastic model for induced seismicity based on non-linear pressure diffusion and irreversible permeability enhancement: Geophysical Journal International, **194**, 1229–1249.

Gutenberg, B., and C. F. Richter, 1956, Magnitude and energy of earthquakes: Science, **83**, 183–185.

Healy, J., W. Rubey, D. Griggs, and C. Raleigh, 1968, The Denver earthquakes: Science, **161**, 1301–1310.

Heidbach, O., M. Rajabi, K. Reiter, M. Ziegler, W. team, et al., 2016, World stress map database release 2016: GFZ Data Services, **10**.

Hennings, P. H., J.-E. Lund Snee, J. L. Osmond, H. R. DeShon, R. Dommisse, E. Horne, C. Lemons, and M. D. Zoback, 2019, Injection-induced seismicity and fault-slip potential in the Fort Worth Basin, Texas: Bulletin of the Seismological Society of America, **109**, 1615–1634.

Higgins-Borchardt, S., J. Sitchler, and T. Bratton, 2016, Geomechanics for unconventional reservoirs, *in* Unconventional Oil and Gas Resources Handbook: Elsevier, 199–213.

Hillis, R., and S. Reynolds, 2000, The Australian stress map: Journal of the Geological Society, **157**, 915–921.

Hsieh, P. A., and J. D. Bredehoeft, 1981, A reservoir analysis of the Denver earthquakes: A case of induced seismicity: Journal of Geophysical Research:

Solid Earth, **86**, 903–920.

Igonin, N., J. P. Verdon, J.-M. Kendall, and D. W. Eaton, 2019, The importance of pre-existing fracture networks for fault reactivation during hydraulic fracturing: Earth and Space Science Open Archive.

Jaeger, J., et al., 1969, Behavior of closely jointed rock: Presented at the The 11th US Symposium on Rock Mechanics (USRMS), American Rock Mechanics Association.

Jaeger, J. C., N. G. Cook, and R. Zimmerman, 2009, Fundamentals of rock mechanics: John Wiley & Sons.

Jia, S. Q., D. W. Eaton, and R. C. Wong, 2018, Stress inversion of shear-tensile focal mechanisms with application to hydraulic fracture monitoring: Geophysical Journal International, **215**, 546–563.

Kao, H., 2017, *in* Induced Seismicity Workshop [Powerpoint slides]: Office of the Regulator of Oil and Gas Operations.

Kennedy, M. C., and A. O'Hagan, 2001, Bayesian calibration of computer models: Journal of the Royal Statistical Society: Series B (Statistical Methodology), **63**, 425–464.

Keranen, K. M., H. M. Savage, G. A. Abers, and E. S. Cochran, 2013, Potentially induced earthquakes in Oklahoma, USA: Links between wastewater injection and the 2011 Mw 5.7 earthquake sequence: Geology, **41**, 699–702.

Keranen, K. M., M. Weingarten, G. A. Abers, B. A. Bekins, and S. Ge, 2014, Sharp increase in central Oklahoma seismicity since 2008 induced by massive wastewater injection: Science, **345**, 448–451.

Krige, D. G., 1951, A statistical approach to some mine valuation and allied problems on the Witwatersrand: PhD thesis, University of the Witwatersrand.

Langenbruch, C., and S. A. Shapiro, 2010, Decay rate of fluid-induced seismicity after termination of reservoir stimulations post injection seismicity: Geophysics, **75**, MA53–MA62.

Langenbruch, C., M. Weingarten, and M. D. Zoback, 2018, Physics-based forecasting of man-made earthquake hazards in Oklahoma and Kansas: Nature communications, **9**, 1–10.

Lee, K.-K., W. L. Ellsworth, D. Giardini, J. Townend, S. Ge, T. Shimamoto,

I.-W. Yeo, T.-S. Kang, J. Rhie, D.-H. Sheen, et al., 2019, Managing injection-induced seismic risks: Science, **364**, 730–732.

Lisle, R. J., and D. C. Srivastava, 2004, Test of the frictional reactivation theory for faults and validity of fault-slip analysis: Geology, **32**, 569–572.

Ma, X., and M. D. Zoback, 2017, Laboratory experiments simulating poroelastic stress changes associated with depletion and injection in low-porosity sedimentary rocks: Journal of Geophysical Research: Solid Earth, **122**, 2478–2503.

Mälicke, M., S. K. Hassler, M. Weiler, T. Blume, and E. Zehe, 2018, Exploring hydrological similarity during soil moisture recession periods using time dependent variograms: Hydrology and Earth System Sciences Discussions, 1–25.

McGarr, A., 2014, Maximum magnitude earthquakes induced by fluid injection: Journal of Geophysical Research: solid earth, **119**, 1008–1019.

McKenzie, D. P., 1969, The relation between fault plane solutions for earthquakes and the directions of the principal stresses: Bulletin of the Seismological Society of America, **59**, 591–601.

Michael, A. J., 1984, Determination of stress from slip data: faults and folds: Journal of Geophysical Research: Solid Earth, **89**, 11517–11526.

Mohr, O., 1914, Abhandlungen aus dem gebiete der technischen mechanik [Treatise on Topics in Engineering Mechanics], 2 ed.: Ernst und Sohn,Berlin.

Morris, A., D. A. Ferrill, and D. B. Henderson, 1996, Slip-tendency analysis and fault reactivation: Geology, **24**, 275–278.

Mullen, M. J., R. Roundtree, G. A. Turk, et al., 2007, A composite determination of mechanical rock properties for stimulation design (what to do when you don't have a sonic log): Presented at the Rocky Mountain Oil & Gas Technology Symposium, Society of Petroleum Engineers.

Myung, I. J., 2003, Tutorial on maximum likelihood estimation: Journal of mathematical Psychology, **47**, 90–100.

Najibi, A., and M. Asef, 2013, A back analysis approach for estimation static stiffness of rock material at depth: Presented at the International EAGE Workshop on Geomechanics and Energy.

Natural Resources Canada, 2019, National building code of Canada

- Seismic hazard values, https://earthquakescanada.nrcan.gc.ca/hazard-alea/interpolat/calc-en.php (accessed January 25, 2020).

Neves, M. C., L. T. Paiva, and J. Luis, 2009, Software for slip-tendency analysis in 3D: A plug-in for Coulomb: Computers & Geosciences, **35**, 2345–2352.

Newendorp, P., and J. Schuyler, 2000, Decision analysis for petroleum exploration, 2 ed.: Planning Press.

Papoulis, A., and S. U. Pillai, 2002, Probability, random variables, and stochastic processes: Tata McGraw-Hill Education.

Pawley, S., R. Schultz, T. Playter, H. Corlett, T. Shipman, S. Lyster, and T. Hauck, 2018, The geological susceptibility of induced earthquakes in the Duvernay play: Geophysical Research Letters, **45**, 1786–1793.

Pollard, D., S. Saltzer, and A. M. Rubin, 1993, Stress inversion methods: are they based on faulty assumptions?: Journal of Structural Geology, **15**, 1045–1054.

Poulin, A., R. Weir, D. Eaton, N. Igonin, Y. Chen, L. Lines, and D. Lawton, 2019, Focal-time analysis: A new method for stratigraphic depth control of microseismicity and induced seismic events: Geophysics, **84**, 1–45.

Prats, M., et al., 1981, Effect of burial history on the subsurface horizontal stresses of formations having different material properties: Society of Petroleum Engineers Journal, **21**, 658–662.

Preston, A., G. Garner, K. Beavis, O. Sadiq, and S. Stricker, 2016, Duvernay reserves and resources report: a comprehensive analysis of Alberta's foremost liquids-rich shale resource: Alberta Energy Regulator, Calgary.

Pyrcz, M. J., and C. V. Deutsch, 2014, Geostatistical reservoir modeling: Oxford university press.

Raleigh, C., J. Healy, and J. Bredehoeft, 1976, An experiment in earthquake control at Rangely, Colorado: Science, **191**, 1230–1237.

Ripley, B. D., 1981, Spatial statistics: Wiley.

Roche, V., and M. van der Baan, 2017, Modeling of the in situ state of stress in elastic layered rock subject to stress and strain-driven tectonic forces: Solid Earth, **8**, 479–498.

Rodriguez-Pradilla, G., 2018, Reservoir characterization of a shale-gas play in the Duvernay formation using seismic, microseismic, and well log data:

Recorder.

Savage, W., H. Swolfs, and B. Amadei, 1992, On the state of stress in the near-surface of the Earth's crust: Pure and Applied Geophysics, **138**, 207–228.

Sayers, C. M., 2006, An introduction to velocity-based pore-pressure estimation: The Leading Edge, **25**, 1496–1500.

Schultz, R., V. Stern, M. Novakovic, G. Atkinson, and Y. J. Gu, 2015, Hydraulic fracturing and the Crooked Lake Sequences: Insights gleaned from regional seismic networks: Geophysical Research Letters, **42**, 2750–2758.

Schultz, R., R. Wang, Y. J. Gu, K. Haug, and G. Atkinson, 2017, A seismological overview of the induced earthquakes in the Duvernay play near Fox Creek, Alberta: Journal of Geophysical Research: Solid Earth, **122**, 492–505.

Shapiro, S., 2018, Seismogenic index of underground fluid injections and productions: Journal of Geophysical Research: Solid Earth, **123**, 7983–7997.

Shapiro, S., R. Patzig, E. Rothert, and J. Rindschwentner, 2003, Triggering of seismicity by pore-pressure perturbations: Permeability-related signatures of the phenomenon, *in* Thermo-Hydro-Mechanical Coupling in Fractured Rock: Springer, 1051–1066.

Shapiro, S. A., and C. Dinske, 2009, Fluid-induced seismicity: Pressure diffusion and hydraulic fracturing: Geophysical Prospecting, **57**, 301–310.

Shapiro, S. A., C. Dinske, C. Langenbruch, and F. Wenzel, 2010, Seismogenic index and magnitude probability of earthquakes induced during reservoir fluid stimulations: The Leading Edge, **29**, 304–309.

Shapiro, S. A., E. Rothert, V. Rath, and J. Rindschwentner, 2002, Characterization of fluid transport properties of reservoirs using induced microseismicity: Geophysics, **67**, 212–220.

Shen, L., D. Schmitt, and K. Haug, 2018, Measurements of the states of in situ stress for the Duvernay formation near Fox Creek, west-central Alberta: Alberta Energy Regulator/Alberta Geological Survey, AER/AGS Report, **97**, 29.

Shipman, T., R. MacDonald, and T. Byrnes, 2018, Experiences and learnings from induced seismicity regulation in Alberta: Interpretation, **6**, SE15–SE21.

Sibson, R. H., 1974, Frictional constraints on thrust, wrench and normal faults: Nature, **249**, 542–544.

———, 1985, A note on fault reactivation: Journal of Structural Geology, **7**, 751–754.

———, 1990, Rupture nucleation on unfavorably oriented faults: Bulletin of the Seismological Society of America, **80**, 1580–1604.

Silin, D., V. Korneev, and G. Goloshubin, 2003, Pressure diffusion waves in porous media, *in* SEG Technical Program Expanded Abstracts 2003: Society of Exploration Geophysicists, 2323–2326.

Silva, V., C. Yepes-Estrada, and G. Weatherill, 2017, Hazard specific risk assessment - 1. Earthquake hazard and risk assessment.

Snee, J.-E. L., and M. D. Zoback, 2016, State of stress in Texas: Implications for induced seismicity: Geophysical Research Letters, **43**, 10–208.

Soltanzadeh, M., A. Fox, and N. Rahim, 2015, Application of an integrated approach for the characterization of mechanical rock properties in the Duvernay formation: Submission 348S0123) Geoconvention, 4–8.

Sone, H., and M. D. Zoback, 2013, Mechanical properties of shale-gas reservoir rocks—part 2: Ductile creep, brittle strength, and their relation to the elastic modulus: Geophysics, **78**, D393–D402.

Song, I., S. Elphick, I. Main, B. Ngwenya, N. Odling, and N. Smyth, 2004, One-dimensional fluid diffusion induced by constant-rate flow injection: Theoretical analysis and application to the determination of fluid permeability and specific storage of a cored rock sample: Journal of Geophysical Research: Solid Earth, **109**.

Statistics Canada, 2017, Fox Creek [Population centre], Alberta [Province] (table). Census Profile, 2016 Census. Statistics Canada. Catalogue no. 98-316-X2016001. Ottawa. https://www12.statcan.gc.ca/census-recensement/2016/dp-pd/prof/index.cfm?Lang=E (accessed January 24, 2020).

Stein, S., and M. Wysession, 2009, An introduction to seismology, earthquakes, and Earth structure: John Wiley & Sons.

Sullivan, M., 2015, Fundamentals of statistics: Pearson.

Switzer, S., W. Holland, D. Christie, G. Graf, A. Hedinger, R. McAuley, R. Wierzbicki, J. Packard, G. Mossop, and I. Shetsen, 1994, Devonian Woodbend-Winterburn strata of the Western Canada Sedimentary Basin:

Geological Atlas of the Western Canada Sedimentary Basin: Canadian Society of Petroleum Geologists and Alberta Research Council, 165–202.

Tibshirani, R. J., and B. Efron, 1993, An introduction to the bootstrap: Monographs on statistics and applied probability, **57**, 1–436.

Town of Fox Creek, 2016, Land Use Bylaw 2016 Update, Town of Fox Creek Comprehensive Community Plan, https://foxcreek.ca/wp-content/uploads/2017/04/Fox-Creek-Land-Use-Bylaw-DRAFT-20160817.pdf (accessed January 25, 2020).

Twiss, R. J., and E. M. Moores, 1992, Structural geology: Macmillan.

Tyagunov, S., L. Stempniewski, G. Grünthal, R. Wahlström, and J. Zschau, 2004, Vulnerability and risk assessment for earthquake prone cities: Proc. of the 13th World Conference on Earthquake Engineering (13 WCEE), Vancouver, BC, Canada, 1–6.

Van der Baan, M., and F. J. Calixto, 2017, Human-induced seismicity and large-scale hydrocarbon production in the usa and c anada: Geochemistry, Geophysics, Geosystems, **18**, 2467–2485.

Van Eck, T., F. Goutbeek, H. Haak, and B. Dost, 2006, Seismic hazard due to small-magnitude, shallow-source, induced earthquakes in the Netherlands: Engineering Geology, **87**, 105–121.

Vavryčuk, V., 2014, Iterative joint inversion for stress and fault orientations from focal mechanisms: Geophysical Journal International, **199**, 69–77.

Walsh, F. R., and M. D. Zoback, 2016, Probabilistic assessment of potential fault slip related to injection-induced earthquakes: Application to north-central Oklahoma, USA: Geology, **44**, 991–994.

Walters, R. J., M. D. Zoback, J. W. Baker, and G. C. Beroza, 2015, Characterizing and responding to seismic risk associated with earthquakes potentially triggered by fluid disposal and hydraulic fracturing: Seismological Research Letters, **86**, 1110–1118.

Wang, J.-F., A. Stein, B.-B. Gao, and Y. Ge, 2012, A review of spatial sampling: Spatial Statistics, **2**, 1–14.

Warrick, A., and D. Myers, 1987, Optimization of sampling locations for variogram calculations: Water Resources Research, **23**, 496–500.

Weingarten, M., S. Ge, J. W. Godt, B. A. Bekins, and J. L. Rubinstein, 2015,

High-rate injection is associated with the increase in US mid-continent seismicity: Science, **348**, 1336–1340.

Weir, R. M., D. W. Eaton, L. R. Lines, D. C. Lawton, and E. Ekpo, 2018, Inversion and interpretation of seismic-derived rock properties in the Duvernay play: Interpretation, **6**, SE1–SE14.

Woo, J.-U., M. Kim, D.-H. Sheen, T.-S. Kang, J. Rhie, F. Grigoli, W. Ellsworth, and D. Giardini, 2019, An in-depth seismological analysis revealing a causal link between the 2017 MW 5.5 Pohang earthquake and EGS project: Journal of Geophysical Research: Solid Earth.

Worum, G., J.-D. van Wees, G. Bada, R. T. van Balen, S. Cloetingh, and H. Pagnier, 2004, Slip tendency analysis as a tool to constrain fault reactivation: A numerical approach applied to three-dimensional fault models in the Roer Valley rift system (Southeast Netherlands): Journal of Geophysical Research: Solid Earth, **109**.

Wu, X., Y. Jiang, Z. Guan, and B. Gong, 2019, Influence of confining pressure-dependent Young's modulus on the convergence of underground excavation: Tunnelling and Underground Space Technology, **83**, 135–144.

Yale, D. P., 2003, Fault and stress magnitude controls on variations in the orientation of in situ stress: Geological Society, London, Special Publications, **209**, 55–64.

Yilmaz, Ö., 2001, Seismic data analysis: Processing, inversion, and interpretation of seismic data: Society of exploration geophysicists.

Yin, Z.-M., and G. Ranalli, 1992, Critical stress difference, fault orientation and slip direction in anisotropic rocks under non-Andersonian stress systems: Journal of Structural Geology, **14**, 237–244.

Zhang, H., D. W. Eaton, G. Rodriguez, and S. Q. Jia, 2019, Source-mechanism analysis and stress inversion for hydraulic-fracturing-induced event sequences near Fox Creek, Alberta: Bulletin of the Seismological Society of America, **109**, 636–651.

Zhang, J., 2011, Pore pressure prediction from well logs: Methods, modifications, and new approaches: Earth-Science Reviews, **108**, 50–63.

Zhang, J., and M. van der Baan, 2019a, Analyzing the decision-making process of hydraulic fracturing operations: Presented at the GeoConvetion, Canadia

Society of Exploration Geophysicists.

———, 2019b, Depth-dependent fault slip potential: SEG Technical Program Expanded Abstracts 2019, 3016–3020.

Zhang, Y., M. Person, J. Rupp, K. Ellett, M. A. Celia, C. W. Gable, B. Bowen, J. Evans, K. Bandilla, P. Mozley, et al., 2013, Hydrogeologic controls on induced seismicity in crystalline basement rocks due to fluid injection into basal reservoirs: Groundwater, **51**, 525–538.

Zoback, M. D., 2010, Reservoir geomechanics: Cambridge University Press.

Zoback, M. D., and S. M. Gorelick, 2012, Earthquake triggering and large-scale geologic storage of carbon dioxide: Proceedings of the National Academy of Sciences, **109**, 10164–10168.

Zoback, M. D., and A. H. Kohli, 2019, Unconventional reservoir geomechanics shale gas, tight oil and induced seismicity: Cambridge University Press.

Zoback, M. L., 1992, First-and second-order patterns of stress in the lithosphere: The world stress map project: Journal of Geophysical Research: Solid Earth, **97**, 11703–11728.

Appendices

Appendix A

Pore pressure change due to injection

Pore pressure diffusion describes the behavior of injected fluids in a porous media. The diffusive behavior of fluids is one of the typical mechanisms of injection-induced microseismicity. The following explanations are adopted from Shapiro et al. (2003) and Eaton (2011).

In a homogeneous, isotropic and poroelastic porous medium, at the direction of the x-axis, the pore pressure behaves as

$$\frac{\partial p(t,x)}{\partial t} = D_x \frac{\partial^2 p(t,x)}{\partial x^2}, \tag{A.1}$$

where D_x is the hydraulic diffusivity in the x-axis, t is the time of diffusion, x is the distance from the observation point, and p is the pore pressure perturbation, a function of time t and distance x.

The diffusivity D_x is defined as

$$D_x = \frac{\alpha K_x}{\zeta}, \tag{A.2}$$

where K_x is the permeability along the x-axis, ζ is the pore-fluid dynamic viscosity and α is the poroelastic modulus. α is defined as

$$\alpha = \frac{TP_d}{H}, \tag{A.3}$$

Table A.1: Values of diffusion parameters in a typical shale gas reservoir.

Parameter	Value	Parameter	Value
ϕ	10%	K_x	$50mD$
ζ	$0.00019Pa \cdot s$	G_d	$22.5GPa$
K_d	$49GPa$	K_g	$75GPa$
K_f	$2.2GPa$		

where

$$T = (\frac{\phi}{K_f} + \frac{\xi - \phi}{K_g})^{-1};$$
$$\xi = 1 - \frac{K_d}{K_g}; H = P_d + \xi^2 T;$$
$$P_d = K_d + \frac{4G_d}{3}.$$

Here $K_{f,d,g}$ are the bulk moduli of the fluid, dry frame and the grain material. Because the medium is assumed as homogeneous and isotropic, the moduli are the same in all directions. G_d is the shear modulus of the dry frame and ϕ is the porosity.

For a typical shale gas reservoir, the pore pressure perturbation from injection is calculated using the values listed in Table A.1

Assume the maximum height of the hydraulic fracture is $100m$ and the width $200m$, and the injection rate and pressure are $10m^3/min$ and $5MPa$ respective. If the injection continues for $60min$, then the pore pressure change at the injection point in $30min$ after the end of the injection is $3MPa$. However, because of the low permeability, the pore pressure perturbation reduces to zero at approximate $20m$ away form the injection point, as shown in Figure A.1a. After the injection, because of diffusion, the pore pressure at the center of the fracture decreases and fluids propagate outwards. Figure A.1b shows the pore pressure perturbation around the hydraulic fracture with injection duration of $5h$ and computation duration of $5d$. The maximum pore pressure perturbation reduces to $0.4MPa$ at the center of the fracture. Figure A.1 illustrate that with a longer injection time and computation duration, the area affected by the injection fluids increases with the decrease of maximum perturbation in pore pressure. If a fault is more than $100m$ away from the hydraulic fracture,

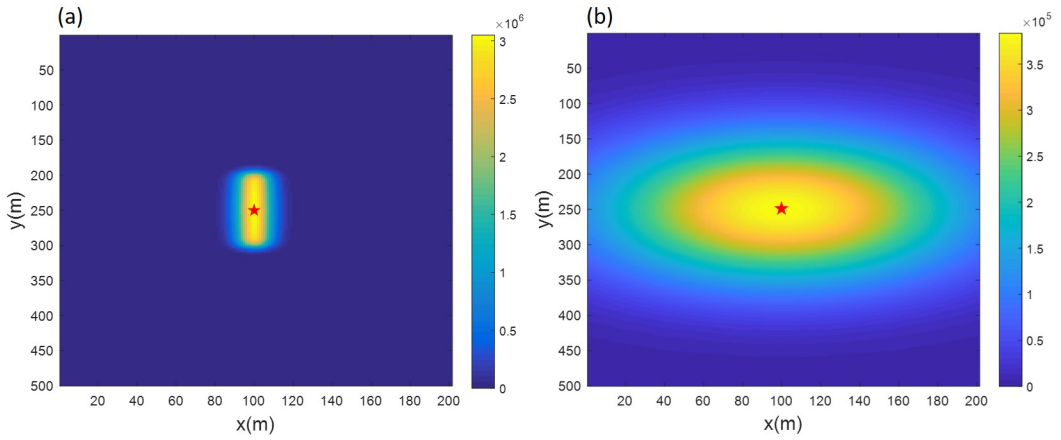

Figure A.1: Pore pressure perturbation at a $100m \times 200m$ hydraulic fracture. Red star indicate the center of the hydraulic fracture. Color bars show the pore pressure in Pa. (a). Injection time is $60min$ and total computation duration $90min$. (b) Injection time is $5h$ and total computation duration of $5d$.

based on the simple model, the pore pressure perturbation at the fault would be smaller than $0.2MPa$.

Appendix B

Relation between variogram and covariance

The variogram between two samples at location $\mathbf{u}_i$ and location $\mathbf{u}_j$ are

$$\begin{aligned} 2\gamma(Z(\mathbf{u}_j), Z(\mathbf{u}_i) &= E\{[Z(\mathbf{u}_j) - Z(\mathbf{u}_i)]^2\} \\ &= E\{Z(\mathbf{u}_j)^2 + Z(\mathbf{u}_i)^2 - 2Z(\mathbf{u}_j)Z(\mathbf{u})_i\} \\ &= E\{Z(\mathbf{u}_j)^2) + E\{Z(\mathbf{u}_i)^2) - 2E\{Z(\mathbf{u}_j)Z(\mathbf{u}_i)\}. \end{aligned} \tag{B.1}$$

For a random variable Z with m as the mean and σ as the variance, we have

$$\begin{aligned} \sigma^2 &= E\{(Z-m)^2\} \\ &= E\{Z^2 + m^2 - 2Zm\} \\ &= E\{Z^2\} + E\{m^2\} - 2E\{Zm\} \\ &= E\{Z^2\} - m^2. \end{aligned} \tag{B.2}$$

For the covariance of the random variables Z with lag h, based on the first- and second-order stationarities we have

$$\begin{aligned} Cov(Z(\mathbf{u}_j), Z(\mathbf{u}_i)) &= E\{(Z(\mathbf{u}_j) - m)(Z(\mathbf{u}_i) - m)\} \\ &= E\{Z(\mathbf{u}_j)Z(\mathbf{u}_i) - mZ(\mathbf{u}_j) - mZ(\mathbf{u}_i) + m^2\} \\ &= E\{Z(\mathbf{u}_j)Z(\mathbf{u}_i)\} \\ &- mE\{Z(\mathbf{u})_j\} - mE\{Z(\mathbf{u}_i)\} + E\{m^2\} \\ &= E\{Z(\mathbf{u}_j)Z(\mathbf{u}_i)\} - m^2 - m^2 + m^2, \\ &= E\{Z(\mathbf{u}_j)Z(\mathbf{u}_i)\} - m^2. \end{aligned} \tag{B.3}$$

Combine Equation B.2, Equation B.3, and Equation B.1 we have,

$$\begin{aligned} 2\gamma(Z(\mathbf{u}_j), Z(\mathbf{u}_i)) &= \sigma^2 + m^2 + \sigma^2 + m^2 - 2Cov(Z(\mathbf{u}_j), Z(\mathbf{u}_i)) - 2m^2 \\ &= 2\sigma^2 - 2Cov(Z(\mathbf{u}_j), Z(\mathbf{u}_i)). \end{aligned} \tag{B.4}$$

If the distance between $\mathbf{u}_j$ and $\mathbf{u}_i$ is h, we can replace $Cov(Z(\mathbf{u}_j), Z(\mathbf{u}_i))$ and $\gamma(Z(\mathbf{u}_j), Z(\mathbf{u}_i))$ with $Cov(h)$ and $\gamma(h)$. Therefore,

$$\gamma(h) = \sigma^2 - Cov(h). \tag{B.5}$$

Appendix C

Normal score transformation

Before kriging, the data set is transformed from the original distribution to a normal distribution with a mean of zero and variance of 1, which is called the normal score transformation. The methodology of the normal score transformation is adopted from Pyrcz and Deutsch (2014).

Denote the data as Z. Z should firstly be standardized by calculating the standard residual Z_r, which is defined as

$$Z_r = \frac{Z - m}{\sigma}, \tag{C.1}$$

where m and σ are the mean and variance of Z.

The basic idea of the normal score transformation is that the p-quantile, or the percentile, stays unchanged before and after the transformation. We have

$$z_r = F_{z_r}^{-1}(F_Z(z)), \tag{C.2}$$

where F represents the cdf of the variable. The steps of normal score transformation are as follows,

1. Create the cdf $F_Z(z)$ of the variable Z;
2. For the value of ith datum z_i, find the corresponding probability $F_Z(z_i)$;
3. Find the corresponding value z_{ri} with the same P_i;

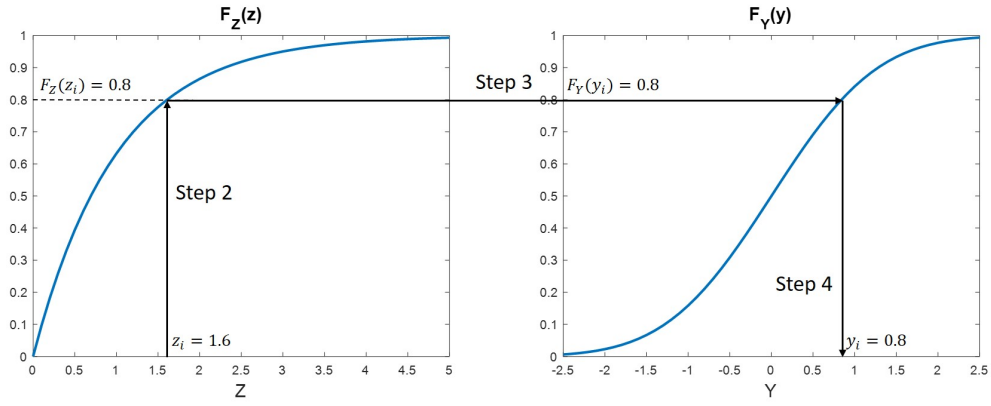

Figure C.1: Demonstration of normal score transformation. $F_Z(z)$ is the cdf in the original domain and $F_Y(y)$ is the cdf in the normal distribution domain. The figure is read from the bottom of the left figure to the right figure, following the arrows. Before and after the normalscore transformation, the percentiles of the data remain unchanged. This figure corresponds to the explanation of Step 2-4 of the normalscore transformation in the context.

4. Assign the value z_{ri} as the new value for the ith datum;

5. repeat steps $2-4$ until all the data are assigned with corresponding values.

Steps 2-4 are also shown in Figure C.1. To transfer the data back to the original distribution after analysis, which is called the backscore transformation, the methodology remains the same. Only the arrows in Figure C.1 point to the opposite direction.

Appendix D

Spatial regression model

If there is a spatial trend, the local mean could vary site by site in the area, and neither first- nor second-order stationarity holds true. In this case, a spatial regression model is used for interpolation. The following explanations are adopted from Eidsvik et al. (2015).

To capture the spatial trend in the variable, the variable is divided into the trend and the residual. The trend can be described with a function of the spatial location $\mathbf{u}$. For a particular location $\mathbf{u}_i$, $\mathbf{u}_i = (u_{xi}, u_{yi})$. Without the trend, the residual satisfies the first- and second-order stationarity. The residual can be calculated using simple kriging. Denote the spatial variable with a trend as $Z_t(\mathbf{u})$, we have

$$Z_t(\mathbf{u}) = t(\mathbf{u}) + w(\mathbf{u}), \tag{D.1}$$

where $t(\mathbf{u})$ denotes the trend and $w(\mathbf{u})$ the residual. The residual is assigned with a normal distribution function as

$$w(\mathbf{u}) = N(0, \mathbf{C}). \tag{D.2}$$

where $\mathbf{C}$ is the covariance matrix of $\mathbf{u}$, which can be obtained with a proper covariance model. $\mathbf{C}$ is described by range η, sill σ^2, and nugget τ^2. The covariance parameters are denoted as $\boldsymbol{\theta} = (\sigma^2, \eta, \tau^2)$.

Since $w(\mathbf{u})$ has a Gaussian distribution, $Z_t(\mathbf{u})$ also has a Gaussian distri-

bution model (Do, 2008). Therefore,

$$p(Z_t(\mathbf{u})) = N(t(\mathbf{u}), \mathbf{C}). \tag{D.3}$$

To estimate the trend $t(\mathbf{u})$ and the covariance parameter vector $\boldsymbol{\theta}$ that fit the data the best, the maximum likelihood estimation is applied.

The trend $t(\mathbf{u})$ can be written as the regression parameters times combinations of the locations. For example, a simple linear trend of $\mathbf{u}$ can be written as

$$t(\mathbf{u}) = \mathbf{G}\boldsymbol{\beta} = [1 \ u_x \ u_y] \begin{bmatrix} \beta_0 \\ \beta_1 \\ \beta_2 \end{bmatrix}. \tag{D.4}$$

For more complex trends, $\mathbf{G}$ and $\boldsymbol{\beta}$ can be changed accordingly. Denote $\boldsymbol{\alpha} = (t(\mathbf{u}), \mathbf{C})$, which are the mean and the variance of $Z_t\mathbf{u}$). To find the optimal parameters that describe $Z_t\mathbf{u}$), the maximum likelihood estimation is applied.

The idea of maximum likelihood estimation is to find $\hat{\boldsymbol{\alpha}}(Z_t\mathbf{u}))$ that maximizes $L_{Z_t\mathbf{u})}(\boldsymbol{\alpha})$ as

$$\begin{aligned} \hat{\boldsymbol{\alpha}}(Z_t\mathbf{u})) &= max\{p(Z_t(\mathbf{u})), \boldsymbol{\alpha}) : \boldsymbol{\alpha} \in \hat{\boldsymbol{\alpha}}\} \\ &= max\{L_{Z_t(\mathbf{u})}(\boldsymbol{\alpha}) : \boldsymbol{\alpha} \in \hat{\boldsymbol{\alpha}}\}. \end{aligned} \tag{D.5}$$

$\hat{\boldsymbol{\alpha}}$ is the set containing all possible values of $\boldsymbol{\alpha}$. One pitfall of maximum likelihood estimation is that the estimated results do not necessarily give the global maximum. This is called the local maxima problem (Myung, 2003).

Since the residual can be calculated with simple kriging, the covariance matrix $\mathbf{C}$ is determined by a variogram model with three parameters, the sill (σ^2), the range (η) and the nugget (τ^2). Here we use $\boldsymbol{\theta}$ to denote the three parameters as $\boldsymbol{\theta} = (\sigma^2, \eta, \tau^2)$. $\boldsymbol{\theta}$ determines $\mathbf{C}$.

With $\mathbf{G}$ predetermined, the values of $\boldsymbol{\beta}$ and $\boldsymbol{\theta}$ are estimated. The log-likelihood function is

$$L(\boldsymbol{\theta}, \boldsymbol{\beta}) = -\frac{m}{2}log(2\pi) - \frac{1}{2}log(|\mathbf{C}|) - \frac{1}{2}Z_t(\mathbf{u})^T\mathbf{C}^{-1}Z_t(\mathbf{u}), \tag{D.6}$$

where m is the number of different locations. The estimated parameters $\hat{\boldsymbol{\theta}}$ should give the arguments of maxima of $l(\boldsymbol{\theta})$ as,

$$\hat{\boldsymbol{\theta}} = argmax\{L(\boldsymbol{\theta})\}. \tag{D.7}$$

Therefore, the partial differential equations should equal zero as

$$\frac{\partial L(\boldsymbol{\theta})}{\partial \boldsymbol{\theta}} = 0. \tag{D.8}$$

With a fixed $\boldsymbol{\theta}$, the derivative of $L(\boldsymbol{\theta})$ with respect to $\boldsymbol{\beta}$ is

$$\frac{dL(\boldsymbol{\theta})}{d\boldsymbol{\beta}} = \mathbf{G^T C^{-1}} Z_t(\mathbf{u}) - \mathbf{G^T C^{-1} G}\boldsymbol{\beta} = 0. \tag{D.9}$$

The solution of $\boldsymbol{\theta}$ to Equation D.8 can be solved numerically. Denote θ_i as the ith component of $\boldsymbol{\theta}$. Using Equation D.8, the derivative of l with respect of θ_i is

$$\begin{aligned} \frac{dL(\boldsymbol{\theta})}{d\theta_i} &= -\frac{1}{2}\frac{dlog|\mathbf{C}|}{d\theta_i} - \frac{1}{2}\frac{dZ_t(\mathbf{u})^T\mathbf{C}^{-1}Z_t(\mathbf{u})}{d\theta_i} \\ &= -\frac{1}{2}trace(\mathbf{C^{-1}}\frac{d\mathbf{C}}{d\theta_i}) + \frac{1}{2}Z_t(\mathbf{u})^{\mathbf{T}}\mathbf{C^{-1}}\frac{d\mathbf{C}}{d\theta_i}\mathbf{C^{-1}}Z_t(\mathbf{u}) \end{aligned} \tag{D.10}$$

To solve Equation D.10, the Fisher scoring algorithm is used. The derivative of l with respect of $\boldsymbol{\theta}$, $dL(\boldsymbol{\theta})/d\boldsymbol{\theta}$, is the score. For $m+1$th iteration, we have

$$\theta_i^{m+1} = \theta_i^m + E\left\{\frac{d^2 l}{d\theta_i^m d\theta_i^m}\right\}\theta_i^m, \tag{D.11}$$

where $E\{*\}$ stands for the expected Hessian, which is

$$E\left\{\frac{d^2 L(\boldsymbol{\theta})}{d\theta_i^m d\theta_i^m}\right\} = -\frac{1}{2}trace\left(\mathbf{C^{-1}}\frac{d\mathbf{C}}{d\theta_i^m}\mathbf{C^{-1}}\frac{d\mathbf{C}}{d\theta_i^m}\right). \tag{D.12}$$

The initial values of $\boldsymbol{\theta}^0$ should be given. And the algorithm is iterated until the score becomes less to a given value or the number of iterations reaches the given number.

Based on the maximum likelihood estimation and fisher scoring algorithm, $\hat{\boldsymbol{\theta}}$ that satisfy Equation D.7 can be estimated. The detailed steps are shown in Figure D.1.

Related scripts run in MATLAB®, which can be found in the supplement of Eidsvik et al. (2015).

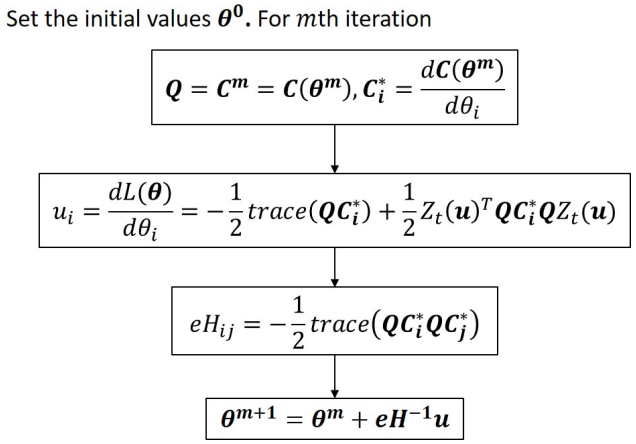

Figure D.1: Estimating $\hat{\boldsymbol{\theta}}$ using maximum likelihood estimation with Fisher scoring.